

**Development of Polymer Blend Solar Cells  
Composed of Conjugated Donor  
and Acceptor Polymers**

**Daisuke MORI**

**2015**



## Contents

### Chapter 1

#### General Introduction

1.1.	Background and Motivation .....	1
1.1.1.	Conjugated Polymers and Their Blends .....	1
1.1.2.	Polymer-Based Solar Cells .....	3
A.	Working Mechanism of Polymer-Based Solar Cells .....	3
B.	Determining Factors for Photovoltaic Performances .....	6
C.	Polymeric Donor Materials for Polymer-Based Solar Cells .....	7
D.	Acceptor Materials for Polymer-Based Solar Cells .....	9
1.1.3.	Polymer/Polymer Blend Solar Cells .....	10
A.	Advantages of Polymer/Polymer Blend Solar Cells .....	10
B.	Development of Polymeric Acceptor Materials .....	11
C.	Morphology of Polymer/Polymer Blend Solar Cells .....	13
1.2.	Outline of This Thesis .....	15
1.3.	References .....	18

## Part I

### Chapter 2

#### *Efficient Polymer/Polymer Blend Solar Cells Developed by Thermal Purification of Nanoscale-Phase-Separated Morphology*

2.1.	Introduction .....	29
2.2.	Results and Discussion .....	30

2.3.	Conclusions .....	37
2.4.	Experimental.....	37
2.5.	Appendix.....	39
2.6.	References and Note .....	43

### **Chapter 3**

#### ***Charge Generation and Recombination Dynamics in Efficient Polymer/Polymer Blend Solar Cells with Nanoscale-Phase-Separated Morphology***

3.1.	Introduction.....	45
3.2.	Results .....	48
3.2.1.	Influence of Thermal Annealing on External Quantum Efficiency .....	48
3.2.2.	Temperature Dependence of Photoluminescence Quenching Efficiency .....	49
3.2.3.	Temperature Dependence of Charge-Carrier Mobility .....	50
3.2.4.	Transient Absorption Spectra .....	51
3.2.5.	Charge Generation and Recombination Dynamics .....	54
3.3.	Discussion.....	61
3.3.1.	Development of Nanoscale Phase Separation by Thermal Annealing.....	61
3.3.2.	Influence of Morphology on Free Carrier Generation Efficiency.....	63
3.3.3.	Relevance to Device Performance .....	64
3.4.	Conclusions .....	65
3.5.	Experimental.....	66
3.6.	Appendix.....	70
3.7.	References and Note .....	75

## *Chapter 4*

### *Influence of Molecular Weight of Acceptor Polymer on the Performance of Polymer/Polymer Blend Solar Cells*

4.1.	Introduction.....	79
4.2.	Results and Discussion .....	81
4.3.	Conclusions.....	88
4.4.	Experimental .....	88
4.5.	Appendix.....	91
4.6.	References.....	93

## *Part II*

## *Chapter 5*

### *Improvement in Light-Harvesting Efficiency by Using Low-Bandgap Donor and Acceptor Polymers*

5.1.	Introduction.....	97
5.2.	Results and Discussion .....	100
5.3.	Conclusions.....	106
5.4.	Experimental .....	107
5.5.	Appendix.....	110
5.6.	References and Note .....	116

*Chapter 6*

*Efficient Charge-Carrier Generation and Collection in Low-Bandgap*

*Donor/Acceptor Polymer Blend Solar Cells with High Charge-Carrier Mobilities*

6.1.	Introduction.....	119
6.2.	Results and Discussion .....	122
6.3.	Conclusions .....	129
6.4.	Experimental.....	130
6.5.	Appendix.....	135
6.6.	References and Note .....	140
	<i>Summary</i> .....	145
	<i>List of Publications</i> .....	149
	<i>Acknowledgment</i> .....	153

# Chapter 1

## General Introduction

### 1.1. Background and Motivation

#### 1.1.1. Conjugated Polymers and Their Blends

Polymer materials play an important role in modern life because of their excellent chemical, physical, and mechanical properties, which allow them to be used in a large number of industrial products. In 1977, Shirakawa *et al.* reported the conductive conjugated polymer, iodine-doped polyacetylene.<sup>1,2</sup> This accomplishment opened the way for a wider application of polymer materials beyond their conventional usage.<sup>3</sup> A conjugated polymer consists of a  $\pi$ -conjugated backbone, composed of linked unsaturated units, resulting in extended  $\pi$ -orbitals along the polymer chain. They therefore possess semiconducting properties, such as charge transporting, light-emitting, and light-absorbing properties, which are comparable or superior to those of conventional inorganic semiconductors. Since their development, conjugated polymers have been applied in various organic electronic devices such as transistors,<sup>4-6</sup> light-emitting devices,<sup>7-11</sup> lasers,<sup>12-14</sup> solar cells,<sup>3,11,14-20</sup> photodiodes,<sup>21</sup> memory devices,<sup>22,23</sup> and thermoelectric transducers.<sup>24</sup> In particular, conjugated polymers have contributed significantly to the progress of organic thin-film transistors (OTFTs), organic light-emitting diodes (OLEDs), and organic photovoltaics (OPVs), as they are key components in all these devices (Figure 1-1).

Polymer blend technologies such as polymer alloys and polymer composites have long been established, especially in industry, for improving the chemical, physical, and mechanical performances of polymer materials. The blending of two or more polymers creates new and invaluable properties and functions, which are not only derived from each

constituent polymer but are also based on the synergistic properties of polymer blends, and as such, depend on the phase-separated structure of these blends.<sup>11,25,26</sup> Recently, considerable attention has been paid to the thin films of conjugated polymer blends in order to apply them to organic electronics. In the case of thin film polymer blends, phase-separation processes are more complicated than bulk polymer blends.<sup>27,28</sup> In addition, thin film polymers are generally prepared by spin coating from polymer blend solutions, and thus the resulting phase separation is constrained to a thermodynamic non-equilibrium state due to the rapid evaporation of solvents. The phase-separated structure critically depends on the processing solvents employed, solvent evaporation rate, and interactions between solvents and solute polymers.<sup>29,30</sup> In order to maximize the optical and electrical functions of thin film polymer blends, it is particularly important to control phase-separated morphology by a careful tuning of these conditions.

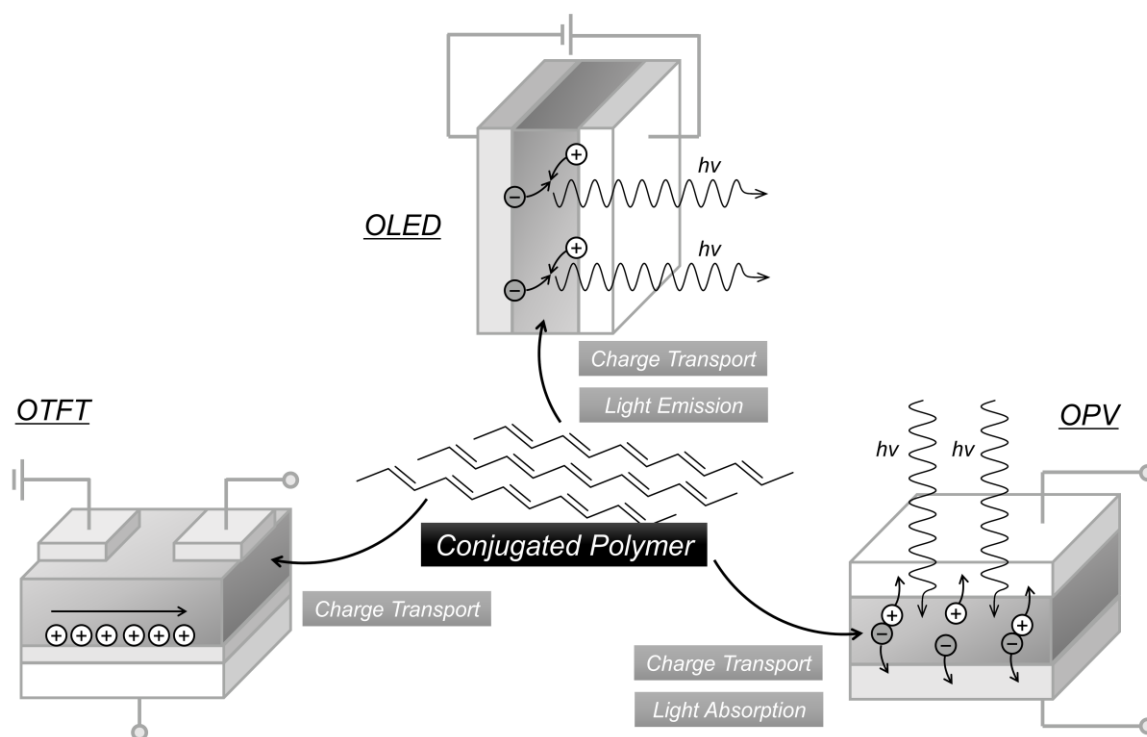


**Figure 1-1.** Application fields of conjugated polymers in organic electronics.

### 1.1.2. Polymer-Based Solar Cells

Polymer-based solar cells have gained increasing attention as a next generation solar cell because of their potential in the fabrication of light-weight, flexible, and large-area devices *via* low-cost production methods.<sup>30–32</sup> Tremendous efforts focusing on their processing, materials, and devices have been devoted to this field in recent years in order to improve the device performance.<sup>3,11,14–20</sup>

#### A. Working Mechanism of Polymer-Based Solar Cells

Organic solar cells work by the combination of an electron-donating (donor) organic semiconductor and an electron-accepting (acceptor) organic semiconductor. In most cases, conjugated polymers are used as donor materials, while fullerene derivatives have been employed as acceptor materials. Figure 1-2 shows a schematic illustration of the working mechanism of organic solar cells. Photovoltaic conversion processes in organic solar cells can be divided into five sequential processes: (i) absorption of an incident photon leading to the formation of a singlet exciton; (ii) diffusion of the exciton to the donor–acceptor interface; (iii) charge transfer at the interface driven by either the LUMO–LUMO energy or the HOMO–HOMO offsets between the donor and acceptor; (iv) dissociation of the charge pair into free charges; and (v) transport of the free charges to the anode and cathode through the networks of donor (hole transport) and acceptor (electron transport) materials, respectively. The incident photon energy can thus be converted into electricity, and a direct current is supplied to an external circuit.<sup>33</sup> It should be noted that in the case of organic semiconductors, the diffusion length of singlet excitons is limited to only approximately 10 nm.<sup>34–37</sup> Therefore, excitons generated at a distance of beyond 10 nm from donor–acceptor interfaces cannot contribute to the generation of the photocurrent. In 1979, Tang *et al.* introduced the donor–acceptor bilayer structure (planar heterojunction, Figure 1-3a) to

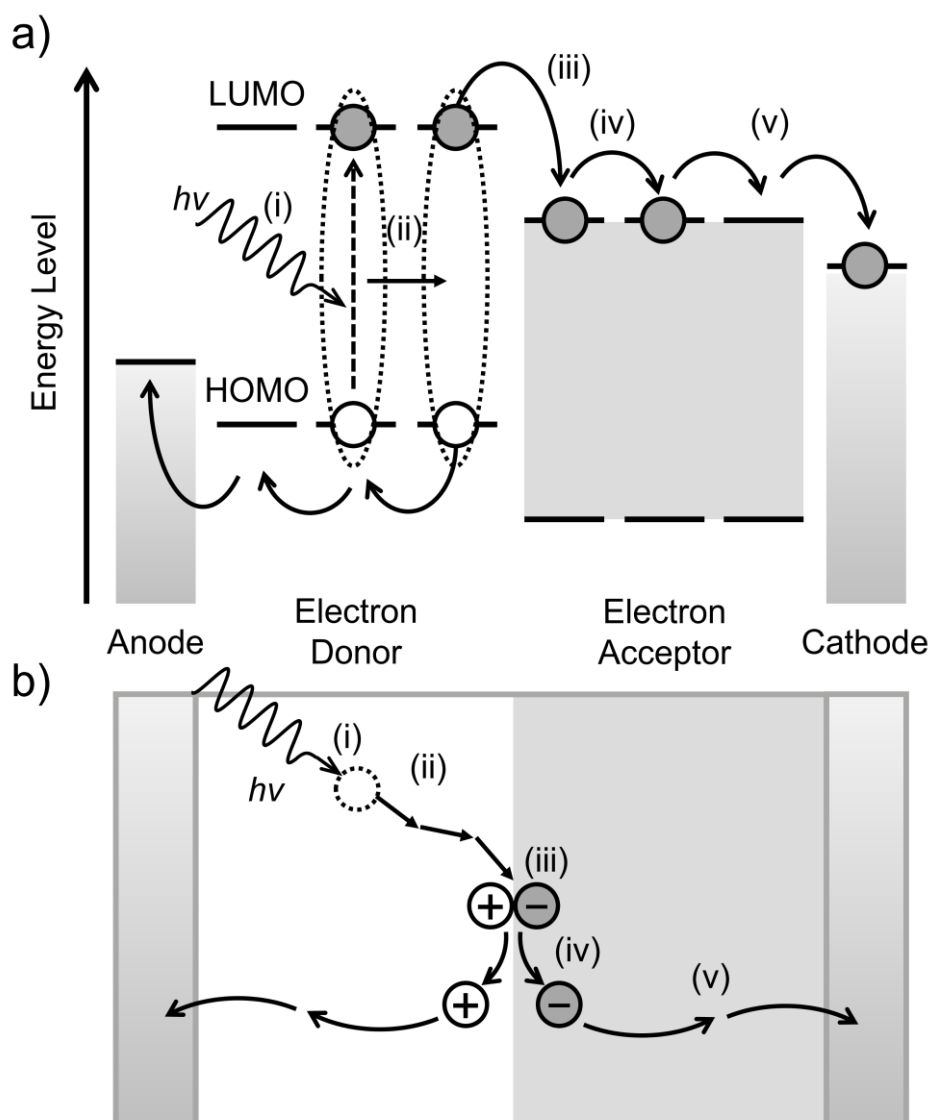


**Figure 1-2.** Schematic illustration of fundamental photovoltaic conversion processes in an organic solar cell from (a) energetic and (b) spatial points of view: (i) exciton generation; (ii) exciton diffusion; (iii) charge transfer; (iv) charge dissociation; and (v) charge transport. These illustrations show the generation of a photocurrent from donor materials. Gray and white circles represent electrons and holes, respectively. Dotted circles indicate excitons.

organic solar cells, and achieved a PCE of approximately 1%.<sup>38</sup> The planar heterojunction structure faces a critical limitation for the generation of a photocurrent due to the small surface area of the interface. This problem can be addressed by introducing a bulk heterojunction (BHJ) structure, which is composed of a mixture of donor and acceptor

materials. This concept was first demonstrated by Hiramoto *et al.* through the co-evaporation of small-molecule donors and acceptors.<sup>39</sup> As shown in Figure 1-3b, BHJ structures can increase the interface area, resulting in a much larger photocurrent than that of planar heterojunction devices. The first efficient BHJ devices were developed independently in 1995 by the groups of Heeger and Friend.<sup>40,41</sup> The BHJ structure is the most successful device architecture for high-efficiency organic solar cells. Although the BHJ concept is a powerful solution for addressing the issue of poor charge generation, the overall photovoltaic performances depend on the phase-separated structure of the donor–acceptor blends. In particular, charge dissociation and charge transport processes are considered to be significantly affected by blend morphology such as domain size, domain composition (purity), and domain connectivity. Controlling the blend morphology is therefore one of the most critical elements in obtaining optimal photovoltaic performances.<sup>42</sup>

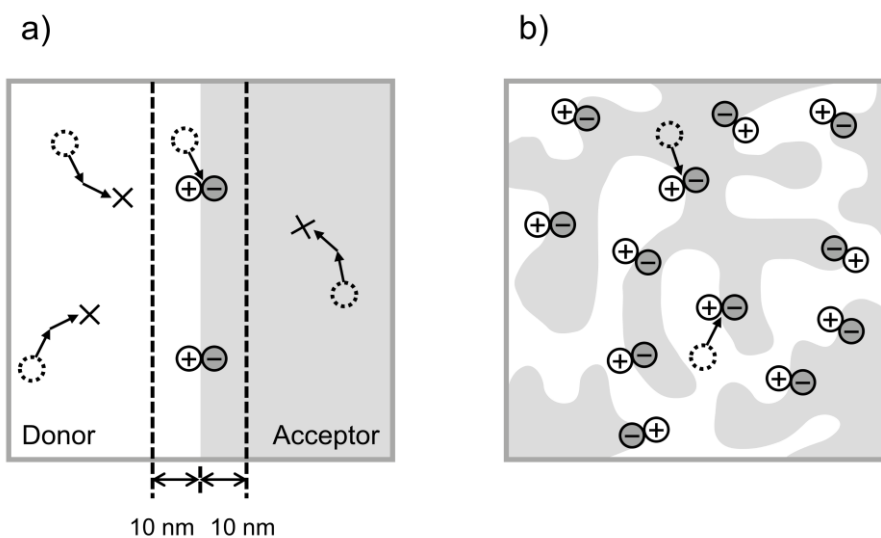


**Figure 1-3.** Schematic illustration of photovoltaic layers: (a) planer heterojunction and (b) bulk heterojunction.

## B. Determining Factors for Photovoltaic Performances

The power conversion efficiency (PCE) of an organic solar cell is determined by the product of short-circuit current density ( $J_{SC}$ ), open-circuit voltage ( $V_{OC}$ ), and fill factor (FF).<sup>33</sup> It is therefore necessary to increase  $J_{SC}$ ,  $V_{OC}$ , and FF simultaneously for enhancing the PCE. The main factor that determines the  $J_{SC}$  of a polymer solar cell is the number of absorbed photons, which is dominated by the optical bandgaps and absorptivities of donor and acceptor materials.  $V_{OC}$  is proportional to the difference in energy between the HOMO level of the donor material and the LUMO level of the acceptor material. Finally, FF is indicative of charge collection efficiency, which is considered to be affected mainly by the charge carrier mobility of the donor and acceptor materials.<sup>17,33</sup> A schematic illustration of the determining factors for each photovoltaic parameter is depicted in Figure 1-4.

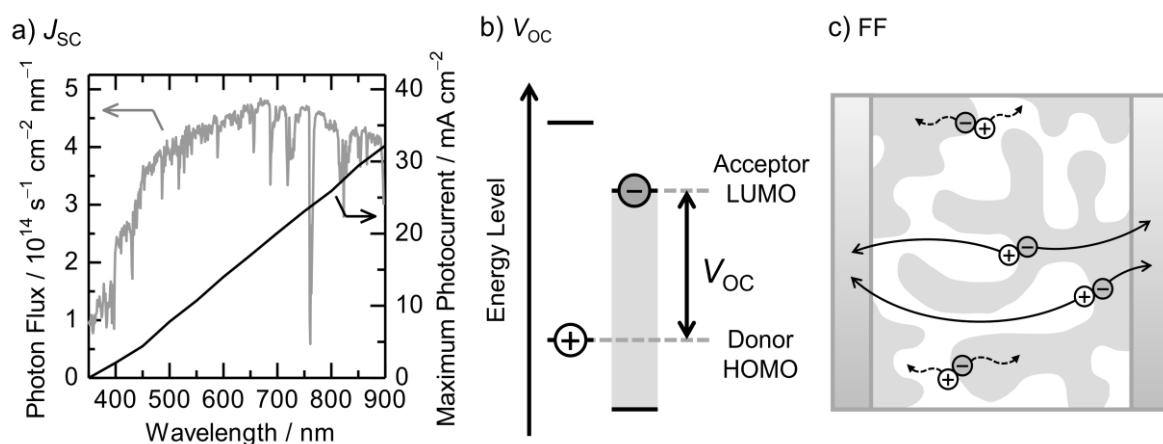


**Figure 1-4.** Schematic illustration of determining factors for each photovoltaic parameter: (a)  $J_{SC}$ ; (b)  $V_{OC}$ ; and (c) FF.

### C. Polymeric Donor Materials for Polymer-Based Solar Cells

After Heeger *et al.* reported the photoinduced electron transfer from the excited state of a poly(*p*-phenylenevinylene)-based conjugated polymer (MEH-PPV, Figure 1-5a) to fullerene C<sub>60</sub>, many researchers began to consider the potential application of conjugated polymers as donor materials for solar cells.<sup>43</sup> In 2001, Brabec *et al.* reported a significant improvement in the PCE of PPV/PCBM BHJ solar cells from 0.9 to 2.5% by the optimization of blend morphology using an appropriate spin-coating solvent. This was also the first investigation into the correlation between the blend morphology and photovoltaic performances.<sup>44</sup> In 2005, Yang *et al.* reported an efficient polymer blend solar cell based on regioregular poly(3-hexylthiophene) (RR-P3HT, Figure 1-5b).<sup>45</sup> The photovoltaic

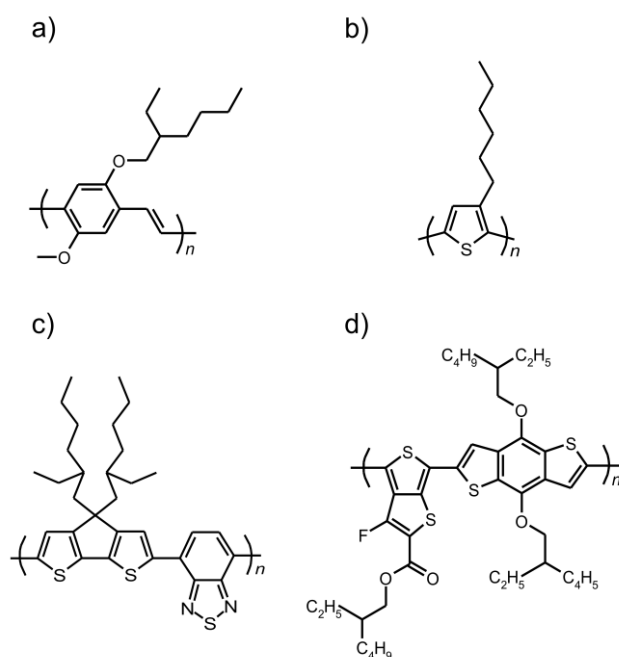


**Figure 1-5.** Chemical structures of polymeric donor materials used in polymer-based solar cells: (a) poly[2-methoxy-5-(2'-ethyl)-hexyloxy-1,4-phenylenevinylene] (MEH-PPV); (b) regioregular poly(3-hexylthiophene) (RR-P3HT); (c) poly[2,6-(4,4-bis-(2-ethylhexyl)- 4*H*-cyclopenta[2,1-*b*;3,4-*b'*]dithiophene)-*alt*-4,7-(2,1,3-benzothiadiazole)] (PCPDTBT); and (d) poly[[4,8-bis[2-ethylhexyloxy]benzo[1,2-*b*:4,5-*b'*]dithiophene-2,6-diyl][3-fluoro-2-[(2-ethylhexyl)carbonyl]thieno[3,4*b*]thiophenediyl]] (PTB7).

performances of P3HT/fullerene solar cells were found to depend on film processing methods<sup>46</sup> such as the selection of spin-coating solvents<sup>47</sup> and annealing temperatures,<sup>48</sup> and on material properties such as regioregularity<sup>49</sup> and the molecular weight of P3HT.<sup>50,51</sup> These factors have been found to cause variations in the degree of ordering of P3HT chains and can thus affect charge transport. Owing to the considerable research effort to obtain the optimum blend morphology, a  $J_{sc}$  exceeding  $10 \text{ mA cm}^{-2}$  and a PCE of over 4% has been achieved for P3HT/PCBM solar cells.<sup>49,52,53</sup> However, as these conjugated polymers, (e.g. PPVs and polythiophenes) can only absorb photons from solar light at wavelengths of up to 650 nm, the maximum obtainable photocurrent is limited to approximately  $12 \text{ mA cm}^{-2}$ .<sup>17</sup> In order to extend the absorption bands from the visible to the near infrared (NIR) region, and thus utilize more photons from solar light, push-pull type low-bandgap polymers (LBPs) were developed.<sup>3,18,19,54,55</sup> One of the most successful LBPs is poly[*N*-9''-heptadecanyl-2,7-carbazole-*alt*-5,5-(4',7'-di-2-thienyl-2',1',3'-benzothia-diazole)] (PCPDTBT, Figure 1-5c), which was reported in 2006 by Brabec *et al.*<sup>56</sup> PCPDTBT has a theoretically optimal optical bandgap of as low as 1.5 eV, and display red-shifted absorption at wavelengths of up to 900 nm. The PCPDTBT/fullerene blend solar cell exhibited  $J_{sc}$  greater than  $15 \text{ mA cm}^{-2}$ , thus resulting in a PCE of 5.5%.<sup>57</sup> This result demonstrated that the use of a low-bandgap polymer was a promising strategy for improving the light-harvesting efficiency and subsequently, the photocurrent. After 2008, a series of alternating copolymers based on thienothiophene (TT) and benzodithiophene (BDT) were reported by several groups.<sup>58-61</sup> One such reported copolymer was poly[[4,8-bis[2-ethylhexyloxy]benzo[1,2-*b*:4,5-*b'*]dithiophene-2,6-diyl][3-fluoro-2-[(2-ethylhexyl)carbonyl]thieno[3,4*b*]thiophenediyl]] (PTB7, Figure 1-5d), which resulted in a PCE as high as 7.4% in PTB7/fullerene blend solar cells.<sup>62,63</sup> More recently, single junction solar cells with a PCE exceeding 10% have been reported.<sup>64,65</sup>

#### D. Acceptor Materials for Polymer-Based Solar Cells

In polymer-based solar cells,  $C_{60}$  fullerene (Figure 1-6a)<sup>43</sup> and its derivatives<sup>18,65-70</sup> have been used as acceptor materials. In particular, a solubilized fullerene, [6,6]-phenyl- $C_{61}$ -butyric acid methyl ester (PCBM, Figure 1-6b) has often been used as an acceptor material.<sup>16-19</sup> As described above, the PCE of polymer/fullerene solar cells have been successfully improved over the past decade, mainly owing to the development of various conjugated donor polymers with rational molecular designs. In the majority of polymer/fullerene solar cells, more than half of the photovoltaic layers consist of small-molecule fullerene derivatives to ensure the presence of sufficient electron transporting networks.<sup>56,57,70,71</sup> However the loading of a large quantity of fullerenes in the photovoltaic layer can lead to some problems to be solved for the further improvement in photovoltaic performances and practical application. Firstly, as the fullerene derivatives can only absorb a small segment of photons present in solar light, they can therefore contribute only a small amount to photocurrent generation. Secondly, the presence of small molecules decreases film-forming ability when they are added to donor polymer films, and cost reduction is limited because a vacuum process is required for the production of fullerenes. There are serious drawbacks for their use in practical application. In order to overcome these problems, electron-accepting conjugated polymers are necessary as alternatives to fullerenes.

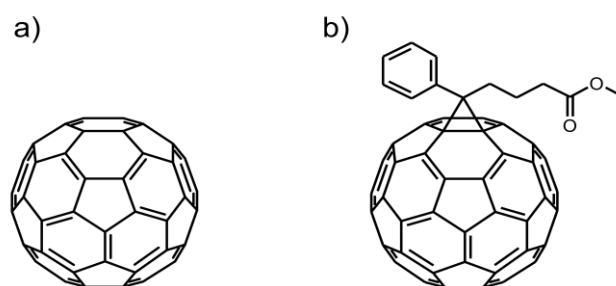


**Figure 1-6.** Chemical structures of acceptor materials used in polymer-based solar cells: (a) fullerene ( $C_{60}$ ) and (b) [6,6]-phenyl- $C_{61}$ -butyric acid methyl ester (PCBM).

### 1.1.3. Polymer/Polymer Blend Solar Cells

#### A. Advantages of Polymer/Polymer Blend Solar Cells

Polymer/polymer blend solar cells, composed of conjugated donor and acceptor polymers, have a number of advantages compared to conventional polymer/fullerene solar cells.<sup>11,20</sup> Of particular importance is the flexible molecular design of not only donor but also acceptor polymers, which allows for the fine tuning of optical, electronic, morphological, and mechanical properties of materials. Firstly, conjugated polymers have high light absorption coefficients in the visible and NIR spectral regions, while fullerenes can absorb photons only at shorter wavelengths of the visible region, as shown in Figure 1-7a. Polymer/polymer solar cells can therefore absorb solar light more efficiently, leading to an increase in  $J_{SC}$ . Secondly, the HOMO–LUMO energy levels of conjugated polymers can be tuned by modifying the chemical structures of their  $\pi$ -conjugated backbones,<sup>54,55,59,60,72</sup>

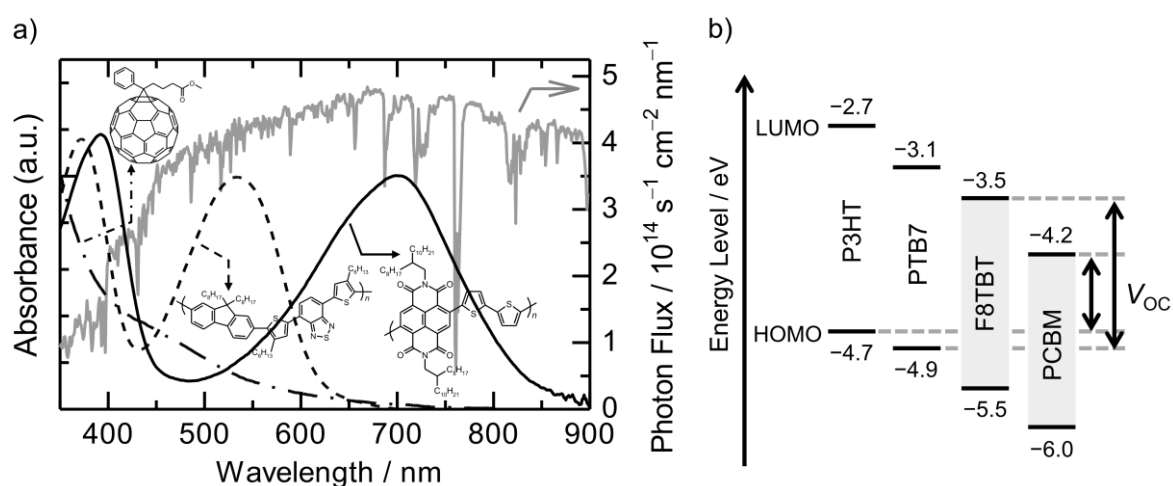


**Figure 1-7.** (a) Absorption spectra of electron-accepting materials: PCBM (black dotted dashed line), F8TBT (black dashed line), and N2200 (black solid line), and photon flux in the AM1.5G solar light under the intensity of  $100 \text{ mW cm}^{-2}$  (gray solid line). (b) HOMO–LUMO energy diagrams of donor (P3HT and PTB7) and acceptor (F8TBT and PCBM) materials.

as shown in Figure 1-7b. A low-lying HOMO level of a donor material and/or a high-lying LUMO level of an acceptor material can result in a  $V_{OC}$  of above 1 V. In addition, the formation of a phase-separated interpenetrating polymer network can offer a continuous pathway for efficient charge transport, thus leading to a high FF. Finally, polymer/polymer blends provide superior flexibility in controlling solution viscosity, which is one of the most important factors for the production of solar cells modules by solution processes. Despite these potential advantages, the PCEs of polymer/polymer solar cells have typically remained below 2% over the last decade,<sup>11,20</sup> lagging far behind those of polymer/fullerene solar cells.<sup>64,65</sup> This is considered to be mainly due to the lack of acceptor polymers with high charge-carrier mobilities, and the difficulty in controlling the phase-separated morphology of polymer/polymer blend films compared to that in polymer/fullerene blends. An extensive effort has therefore been devoted to both the development of acceptor polymers and the control of blend morphology to enhance the photovoltaic performances of polymer/polymer blend solar cells.<sup>11,20,28</sup>

## B. Development of Polymeric Acceptor Materials

In 2007, Friend *et al.* demonstrated that a fluorene-based copolymer, poly[2,7-(9,9-dioctylfluorene)-*alt*-5,5-(4',7'-bis(4-hexyl-2-thienyl)-2',1',3'-benzo-thiadiazole)] (F8TBT, Figure 1-8a), behaves as an acceptor when it is blended with donor P3HT.<sup>73</sup> The P3HT/F8TBT solar cells exhibited a maximum PCE of 1.9% with a high  $V_{OC}$  exceeding 1 V.<sup>74-76</sup> In 2009, Facchetti *et al.* reported a new acceptor polymer, poly{[*N,N'*-bis(2-octyldodecyl)-naphthalene-1,4,5,8-bis(dicarboximide)-2,6-diyl]-*alt*-5,5'-(2,2'-bithiophene)} (N2200, Figure 1-8b), which exhibited not only efficient light absorption at wavelengths ranging from the visible to the NIR regions but also high electron mobility comparable to that of fullerenes.<sup>77,78</sup> One of the most researched polymer/polymer solar

cells based on N2200 as an acceptor is the blend of P3HT and N2200. Although the first-reported P3HT/N2200 solar cells were found to exhibit a PCE of only 0.2%, the optimization of film-preparing conditions resulted in an increase in the PCE of up to 1.4%, with a remarkably high FF of 0.7.<sup>79–82</sup> Other rylene-based electron-accepting polymers have also been prepared.<sup>83,84</sup> In 2011, Hashimoto *et al.* synthesized a series of perylene-3,4,9,10-tetracarboxylic diimide-based copolymers (Figure 1-8c) with different donor units, displaying a wide variety of HOMO and LUMO energy levels. They successfully increased the PCE to 2.2%, with a high  $J_{sc}$  of above  $6 \text{ mA cm}^{-2}$ , through blending the acceptor polymers with polythiophene derivatives as the donor material.<sup>85</sup> Acceptor polymers have therefore contributed to an improvement in the photovoltaic performances of polymer/polymer blend solar cells.<sup>86</sup>

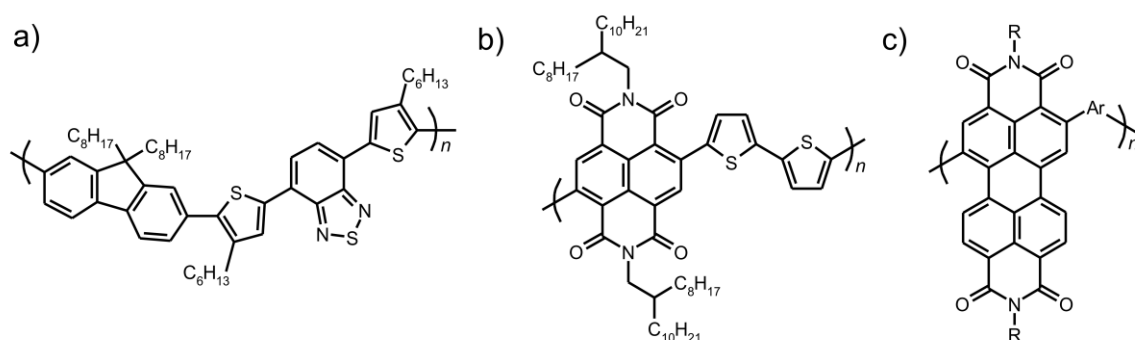


**Figure 1-8.** Chemical structures of polymeric acceptor materials used in polymer/polymer solar cells: (a) poly[2,7-(9,9-dioctylfluorene)-*alt*-5,5-(4',7'-bis(4-hexyl-2-thienyl)-2',1',3'-benzo-thiadiazole)] (F8TBT); (b) poly{[*N,N'*-bis(2-octyldodecyl)-naphthalene-1,4,5,8-bis(dicarboximide)-2,6-diyl]-*alt*-5,5'-(2,2'-bithiophene)} (N2200); and (c) a perylene-3,4,9,10-tetracarboxylic diimide-based copolymer (Ar and R indicate aryl groups and alkyl side chains, respectively).

### C. Morphology of Polymer/Polymer Blend Solar Cells

Considerable effort has been focused on the optimization of phase-separated structure in polymer/polymer blend films. The ideal morphology for the photovoltaic performance is considered to be a nanostructured thin film with bicontinuous interpenetrating networks of pure donor and acceptor domains possessing characteristic spacing similar to the exciton diffusion length (10 nm), which is necessary for efficient charge generation and transport.<sup>11,28</sup> The degree of phase separation of two materials depends on the change in the entropy and enthalpy before and after their mixing. According to the Flory-Huggins theory,<sup>87,88</sup> the expression for the free energy of mixing polymers ( $G_{\text{mix}}$ ) can be derived as follows:

$$\frac{G_{\text{mix}}}{nkT} = \frac{\varphi_A}{N_A} \ln(\varphi_A) + \frac{\varphi_B}{N_B} \ln(\varphi_B) + \chi\varphi_A\varphi_B \quad (1)$$

Here  $\varphi_{A/B}$  is the volume fraction of polymer A/B (with  $\varphi_A + \varphi_B = 1$ ),  $N_{A/B}$  is the degree of polymerization of polymer A/B,  $n$  is the total number of segments, and  $\chi$  is the Flory-Huggins interaction parameter. The first two terms on the right hand side of Equation 1 represent the entropy component, while the final term represents the enthalpy contribution. In the case of polymer/polymer blends, the entropy gain is reduced by a factor of  $N_{A/B}$ , resulting in a lower mixing entropy than that of the polymer blend with small molecules.<sup>11,28,89</sup> In practice, polymer/polymer blends tend to phase-separate on a micrometer scale, which is undesirable with regards to the photovoltaic performance, while polymer/fullerene blends were observed to mix on a nanometer scale.<sup>29,90-93</sup> For polymer/polymer blends, it is therefore critically important to suppress phase separation. In addition, in terms of the enthalpic component,  $\chi$  is an interaction parameter between two materials, where a small value of  $\chi$  is required to obtain a well-mixed structure. Since  $\chi$  depends on the chemical structures of both materials, the selection of donor and acceptor

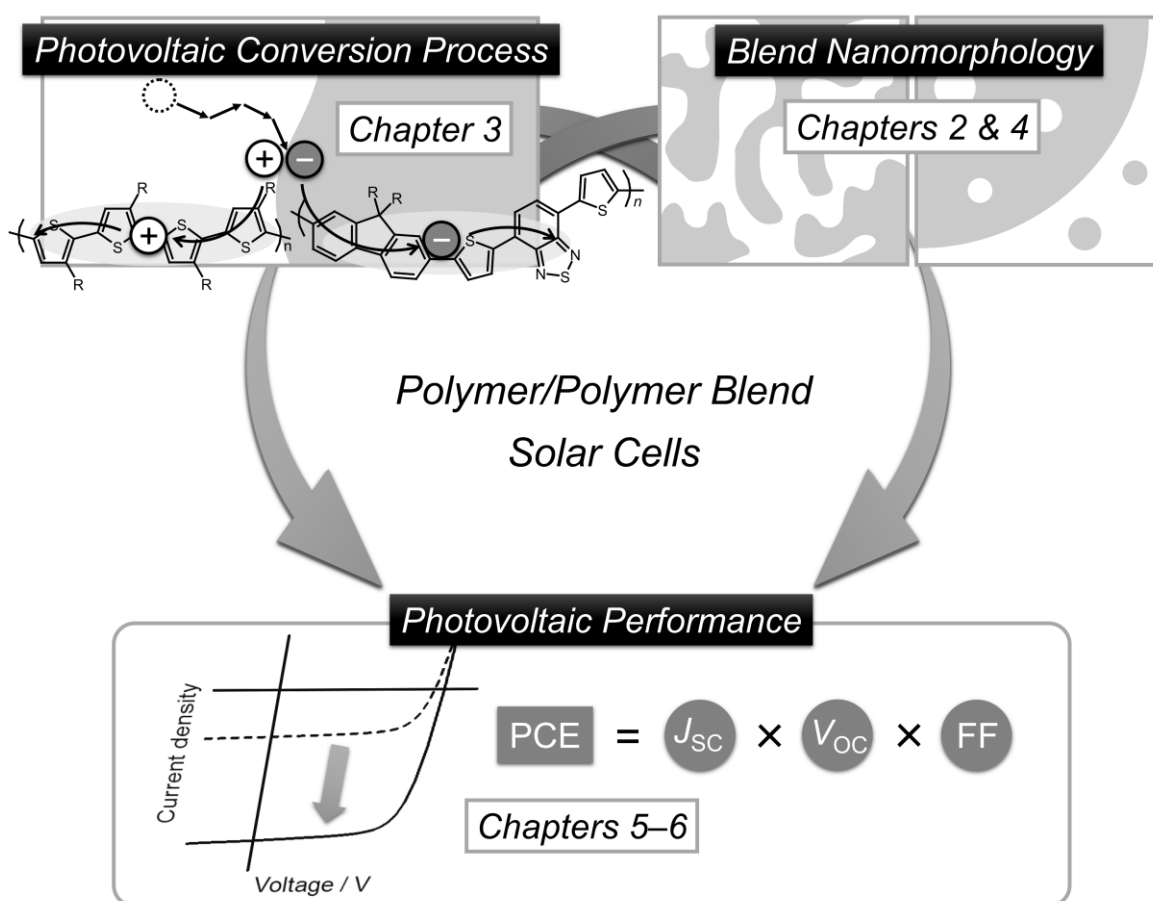
materials from the viewpoint of their miscibility is also important to obtain the ideal blend morphology. It is also well known that the polymer blend films as-prepared by spin coating are not at a thermodynamic equilibrium state. The kinetics of film formation therefore also affect the development of phase-separated structures ranging from well-mixed structures on a nanometer scale to thermodynamically favored demixed structures on a larger scale.<sup>28–30</sup>

A number of groups have attempted to obtain the optimum blend morphology by both thermodynamically and kinetically based approaches. Examples include the design of side chains for adjusting miscibility,<sup>94–97</sup> the use of block copolymers,<sup>98–100</sup> the selection of spin-coating solvents,<sup>79–82,84,85,96,101–104</sup> and either solvent- or thermal-annealing of the film after casting.<sup>74,75,79,89,94,98,100,101</sup> However, tuning of the film morphology of polymer/polymer blends to optimize device performance still appears to be a challenge.

The characterization of the structure of polymer blend films with high chemical specificity and spatial resolution is significantly important. A large number of experimental techniques have been used to investigate the morphology such as transmission electron microscopy,<sup>102</sup> atomic force microscopy,<sup>90–92</sup> and X-ray diffraction and scattering methods.<sup>82,102,105,106</sup> Despite a great deal of research being carried out in this field, the relationship between phase-separated nanostructures of the polymer/polymer blend and their device performance is still under discussion.

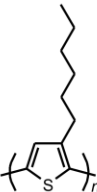
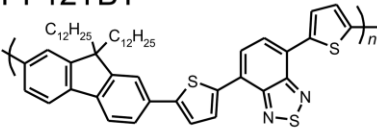
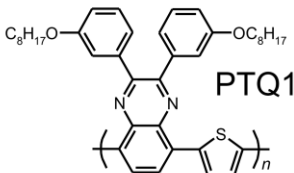
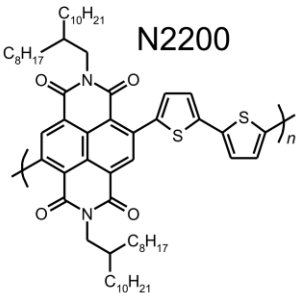
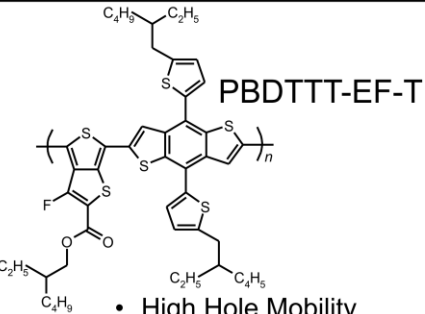
## 1.2. Outline of This Thesis

The objective of this thesis is to develop efficient polymer blend solar cells composed of donor and acceptor conjugated polymers both by controlling the nanoscale blend morphology, and by the appropriate selection of an efficient donor/acceptor polymer combination from the viewpoint of  $J_{SC}$ ,  $V_{OC}$ , and FF. In addition, based on the dynamics of fundamental photovoltaic conversion processes, the correlation between the blend nanomorphology and the photovoltaic performance is discussed. This thesis consists of six chapters. The first chapter describes the background and motivation of the thesis. The following chapters are then divided into two parts.



**Figure 1-9.** Schematic illustration of thesis outline.

In Part I (Chapters 2–4), the correlation between the photovoltaic performances and the nanomorphology of polymer/polymer blend films is examined, where P3HT is used as the donor material and a fluorene-based copolymer (PF12TBT) is used as the acceptor material; both can efficiently absorb photons in the visible region. In Chapter 2, the author prepares devices using different solvents. To address the origin of the different device performances depending on the spin-coating solvent, atomic force microscopy measurements of the blend films are conducted. Moreover, the influence of thermal annealing on device performances is systematically investigated. Combining the annealing-temperature dependence of photovoltaic parameters with the photoluminescence

	<i>Donor Polymer</i>	<i>Acceptor Polymer</i>
<i>Part I</i> <i>Chapters 2 – 4</i>	 <p><b>P3HT</b></p> <ul style="list-style-type: none"> <li>• High Hole Mobility</li> <li>• Light Absorption: Visible</li> </ul>	 <p><b>PF12TBT</b></p> <ul style="list-style-type: none"> <li>• High LUMO Level</li> <li>• Light Absorption: Visible</li> </ul>
<i>Part II</i> <i>Chapter 5</i>	 <p><b>PTQ1</b></p> <ul style="list-style-type: none"> <li>• Light Absorption: NIR</li> </ul>	 <p><b>N2200</b></p> <ul style="list-style-type: none"> <li>• High Electron Mobility</li> <li>• Light Absorption: NIR</li> </ul>
<i>Chapter 6</i>	 <p><b>PBDTTT-EF-T</b></p> <ul style="list-style-type: none"> <li>• High Hole Mobility</li> <li>• Light Absorption: NIR</li> </ul>	

**Figure 1-10.** Donor and acceptor polymer materials used in each chapter of this thesis.

quenching observations, the successful improvement in device performance by thermal annealing is explained on the basis of purification of the nanoscale-phase-separated domains. In Chapter 3, charge carrier generation and recombination dynamics are examined by using transient absorption spectroscopy, in order to clarify the relationship between blend nanomorphology and device performance from the viewpoint of fundamental photovoltaic conversion processes. The improvement in device performance by thermal annealing is explained with reference to an increase in free carrier generation efficiency in the blend films. In Chapter 4, on the basis of the findings obtained from the discussion in Chapters 2 and 3, a further improvement in photovoltaic performance is demonstrated with the use of a high-molecular-weight acceptor polymer. In terms of the annealing-temperature dependence of the device performances and photoluminescence quenching efficiencies in blend films, the effect of molecular weight of the acceptor polymer on nanomorphology and the importance of high-molecular-weight polymers for improving photovoltaic performances are discussed.

In Part II (Chapters 5 and 6), in order to enhance the light-harvesting efficiency in the NIR region, low-bandgap polymers are used as both the donor and acceptor materials. In Chapter 5, the preparation of efficient polymer/polymer blend solar cells using low-bandgap donor and acceptor polymers is described. The compositional dependence of charge generation efficiencies and charge carrier mobilities in blend films is also examined. In terms of charge generation and transport, the origin of the improved performance is discussed. In Chapter 6, the development of highly efficient polymer/polymer blend solar cells using low-bandgap donor and acceptor polymers, with high absorption coefficients in the NIR region and excellent hole and electron mobilities is described.

### 1.3. References

- [1] H. Shirakawa, E. J. Louis, A. G. Macdiarmid, C. K. Chiang, A. J. Heeger, *J. Chem. Soc., Chem. Commun.* **1977**, 578–580.
- [2] C. K. Chiang, C. R. Fincher, Jr., Y. W. Park, A. J. Heeger, H. Shirakawa, E. J. Louis, S. C. Gau, and Alan G. MacDiarmid, *Phys. Rev. Lett.* **1977**, *39*, 1098–1101.
- [3] A. Facchetti, *Chem. Mater.* **2011**, *23*, 733–758.
- [4] A. Tsumura, H. Koezuka, T. Ando, *Appl. Phys. Lett.* **1986**, *49*, 1210–1212.
- [5] M. Muccini, *Nature* **2006**, *5*, 605–613.
- [6] A. Facchetti, *Mater. Today* **2007**, *10*, 28–37.
- [7] J. H. Burroughes, D. D. C. Bradley, A. R. Brown, R. N. Marks, K. Mackay, R. H. Friend, P. L. Burns, A. B. Holmes, *Nature* **1990**, *347*, 539–541.
- [8] N. C. Greenham, S. C. Moratti, D. D. C. Bradley, R. H. Friend, A. B. Holmes, *Nature* **1993**, *365*, 628–630.
- [9] R. H. Friend, R. W. Gymer, A. B. Holmes, J. H. Burroughes, R. N. Marks, C. Taliani, D. D. C. Bradley, D. A. Dos Santos, J. L. Brédas, M. Lögdlund, W. R. Salaneck, *Nature* **1999**, *397*, 121–128.
- [10] A. C. Grimsdale, K. L. Chan, R. E. Martin, P. G. Jokisz, A. B. Holmes, *Chem. Rev.* **2009**, *109*, 897–1091.
- [11] C. R. McNeill, N. C. Greenham, *Adv. Mater.* **2009**, *21*, 3840–3850.
- [12] F. Hide, M. A. Díaz-Gracia, B. J. Schwartz, A. J. Heeger, *Acc. Chem. Res.* **1997**, *30*, 430–436.
- [13] M. D. McGehee, A. J. Heeger, *Adv. Mater.* **2000**, *12*, 1655–1668.
- [14] I. D. W. Samuel, G. A. Turnbull, *Chem. Rev.* **2007**, *107*, 1272–1295.
- [15] H. Hoppe, N. S. Sariciftci, *J. Mater. Res.* **2004**, *19*, 1924–1945.
- [16] A. C. Mayer, S. R. Scully, B. E. Hardin, M. W. Rowell, M. D. McGehee, *Mater.*

*Today* **2007**, *10*, 28–33.

- [17] G. Dennler, M. C. Schaber, C. J. Brabec, *Adv. Mater.* **2009**, *21*, 1323–1338.
- [18] Y. Su, S. Lan, K. Wei, *Mater. Today* **2012**, *15*, 554–562.
- [19] G. Li, R. Zhu, Y. Yang, *Nat. Photon.* **2012**, *6*, 153–161.
- [20] A. Facchetti, *Mater. Today* **2013**, *16*, 123–132.
- [21] X. Gong, M. Tong, Y. Xia, W. Cai, J. S. Moon, Y. Cao, G. Yu, C. Shieh, B. Nilsson, A. J. Heeger, *Science* **2009**, *325*, 1665–1667.
- [22] S. Möller, C. Perlov, W. Jackson, C. Taussig, S. R. Forrest, *Nature* **2003**, *426*, 166–169.
- [23] A. Prakash, J. Ouyang, J. Lin, Y. Yang, *J. Appl. Phys.* **2006**, *100*, 054309.
- [24] O. Bubnova, X. Crispin, *Energy Environ. Sci.* **2012**, *5*, 9345–9362.
- [25] J. W. Barlow, D. R. Paul, *Polym. Eng. Sci.* **2004**, *21*, 985–996.
- [26] C. Koning, M. van Duin, C. Pagnouille, R. Jerome, *Prog. Polym. Sci.* **1998**, *23*, 707–757.
- [27] E. Moons, *J. Phys.: Condens. Matter* **2002**, *14*, 12235–12260.
- [28] C. R. McNeill, *Energy Environ. Sci.* **2012**, *5*, 5653–5667.
- [29] S. Walheim, M. Böltau, J. Mlynek, G. Krausch, U. Steiner, *Macromolecules* **1997**, *30*, 4995–5003.
- [30] S. Nilsson, A. Bernasik, A. Budkowski, E. Moons, *Macromolecules* **2007**, *40*, 8291–8301.
- [31] M. Berggren, D. Nilsson, N. D. Robinson, *Nat. Mater.* **2007**, *6*, 3–5.
- [32] R. R. Søndergaard, M. Hösel, F. C. Krebs, *J. Polym. Sci. Part B: Polym. Phys.* **2012**, *51*, 16–34.
- [33] B. Kippelen, J. Brédas, *Energy Environ. Sci.* **2009**, *2*, 251–261.
- [34] J. J. M. Halls, K. Pichler, R. H. Friend, S. C. Moratti, and A. B. Holmes, *Appl. Phys.*

- Lett.* **1996**, *68*, 3120–3122.
- [35] D. E. Markov, E. Amsterdam, P. W. M. Blom, A. B. Sieval, J. C. Hummelen, *J. Phys. Chem. A* **2005**, *109*, 5266–5274.
- [36] P. E. Shaw, A. Ruseckas, I. D. W. Samuel, *Adv. Mater.* **2008**, *20*, 3516–3520.
- [37] O. V. Mikhnenko, H. Azimi, M. Schaber, M. Morana, P. W. M. Blom, M. A. Loi, *Energy Environ. Sci.* **2012**, *5*, 6960–6965.
- [38] C. W. Tang, *Appl. Phys. Lett.* **1986**, *48*, 183–185.
- [39] M. Hiramoto, H. Fujiwara, M. Yokoyama, *J. Appl. Phys.* **1992**, *72*, 3781–3787.
- [40] G. Yu, J. Gao, J. C. Hummelen, F. Wudl, A. J. Heeger, *Science* **1995**, *270*, 1789–1791.
- [41] J. J. M. Halls, C. A. Walsh, N. C. Greenham, E. A. Marseglia, R. H. Friend, S. C. Moratti, A. B. Holmes, *Nature* **1995**, *376*, 498–500.
- [42] H. Hoppe, N. S. Sariciftci, *J. Mater. Chem.* **2006**, *16*, 45–61.
- [43] N. S. Sacritifi, L. Smilowitz, A. J. Heeger, F. Wudl, *Science* **1992**, *258*, 1474–1476.
- [44] S. E. Shaheen, C. J. Brabec, N. S. Sariciftci, F. Padinger, T. Fromherz, J. C. Hummelen, *Appl. Phys. Lett.* **2001**, *78*, 841–843.
- [45] G. Li, V. Shrotria, J. Huang, Y. Yao, T. Moriarty, K. Emery, Y. Yang, *Nat. Mater.* **2005**, *4*, 864–868.
- [46] M. T. Dang, L. Hirsch, G. Wantz, *Adv. Mater.* **2011**, *23*, 3598–3602.
- [47] M. T. Dang, G. Wantz, H. Bejbouji, M. Urien, O. J. Dautel, L. Vignau, L. Hirsch, *Sol. Energy Mater. Sol. Cells* **2011**, *95*, 3408–3418.
- [48] Y. Kim, S. A. Choulis, J. Nelson, D. D. C. Bradley, S. Cook, J. R. Durrant, *Appl. Phys. Lett.* **2005**, *86*, 063502.
- [49] Y. Kim, S. Cook, S. M. Tuladhar, S. A. Choulis, J. Nelson, J. R. Durrant, D. D. C. Bradley, M. Giles, I. McCulloch, C. Ha, M. Ree, *Nat. Mater.* **2006**, *5*, 197–203.

- [50] R. C. Hiorns, R. Bettignies, J. Leroy, S. Bailly, M. Firon, C. Sentein, A. Khoukh, H. Preud'homme, C. Dagron-Lartigau, *Adv. Funct. Mater.* **2006**, *16*, 2263–2273.
- [51] A. M. Ballantyne, L. Chen, J. Dane, T. Hammant, F. M. Braun, M. Heeney, W. Duffy, I. McCulloch, D. D. C. Bradley, J. Nelson, *Adv. Funct. Mater.* **2008**, *18*, 2373–2380.
- [52] W. Ma, C. Yang, X. Gong, K. Lee, A. J. Heeger, *Adv. Funct. Mater.* **2005**, *15*, 1617–1622.
- [53] J. Y. Kim, S. H. Kim, H. Lee, K. Lee, W. Ma, X. Gong, A. J. Heeger, *Adv. Mater.* **2006**, *18*, 572–576.
- [54] Y. Li, *Acc. Chem. Res.* **2012**, *45*, 723–733.
- [55] E. Zhou, K. Hashimoto, K. Tajima, *Polymer* **2013**, *54*, 6501–6509.
- [56] D. Mühlbacher, M. Scharber, M. Morana, Z. Zhu, D. Waller, R. Gaudiana, C. Brabec, *Adv. Mater.* **2006**, *18*, 2884–2889.
- [57] J. Peet, J. Y. Kim, N. E. Coates, W. L. Ma, D. Moses, A. J. Heeger, G. C. Bazan, *Nat. Mater.* **2007**, *6*, 497–500.
- [58] Y. Liang, Y. Wu, D. Feng, S. Tsai, H. Son, G. Li, L. Yu, *J. Am. Chem. Soc.* **2009**, *131*, 56–57.
- [59] Y. Liang, D. Feng, Y. Wu, S. Tsai, G. Li, C. Ray, L. Yu, *J. Am. Chem. Soc.* **2009**, *131*, 7792–7799.
- [60] H. Chen, J. Hou, S. Zhang, Y. Liang, G. Yang, Y. Yang, L. Yu, Y. Wu, G. Li, *Nat. Photon.* **2009**, *3*, 649–653.
- [61] L. Huo, J. Hou, S. Zhang, H. Chen, Y. Yang, *Angew. Chem. Int. Ed.* **2010**, *122*, 1542–1545.
- [62] Y. Liang, Z. Xu, J. Xia, S. Tsai, Y. Wu, G. Li, C. Ray, L. Yu, *Adv. Mater.* **2010**, *22*, E135–E138.
- [63] C. Gu, Y. Chen, Z. Zhang, S. Xue, S. Sun, C. Zhong, H. Zhang, Y. Lu, F. Li, F. Huang,

- Y. Ma, *Adv. Energy Mater.* **2014**, *4*, 1301771.
- [64] S. Liao, H. Jhuo, P. Yeh, Y. Cheng, Y. Li, Y. Lee, S. Sharma, S. Chen, *Sci. Rep.* **2014**, *4*, 6813.
- [65] Y. Liu, J. Zhao, Z. Li, C. Mu, W. Ma, H. Hu, K. Jiang, H. Lin, H. Ade, H. Yan, *Nat. Commun.* **2014**, *5*, 5293.
- [66] H. W. Kroto, J. R. Heath, S. C. O'Brien, R. F. Curl, R. E. Smalley, *Nature* **1985**, *318*, 162–163.
- [67] C. Zhao, Y. He, Y. Li, *Adv. Mater.* **2010**, *22*, 4355–4358.
- [68] M. Lenes, G.-J. A. H. Wetzelaer, F. B. Kooistra, S. C. Veenstra, J. C. Hummelen, P. W. M. Blom, *Adv. Mater.* **2008**, *20*, 2116–2119.
- [69] L. M. Popescu, P. van 't Hof, A. B. Sieval, H. T. Jonkman, J. C. Hummelen, *Appl. Phys. Lett.* **2006**, *89*, 213507.
- [70] J. K. J. van Duren, X. Yang, J. Loos, C. W. T. Bulle-Lieuwma, A. B. Sieval, J. C. Hummelen, R. A. J. Janssen, *Adv. Funct. Mater.* **2004**, *14*, 425–434.
- [71] L. M. Andersson, F. Zhang, O. Inganäs, *Appl. Phys. Lett.* **2007**, *91*, 071108.
- [72] J. Chen, Y. Cao, *Acc. Chem. Res.* **2009**, *42*, 1709–1718.
- [73] C. R. McNeill, A. Abrusci, J. Zaumseil, R. Wilson, M. J. McKiernan, J. H. Burroughes, J. J. M. Halls, N. C. Greenham, R. H. Friend, *Appl. Phys. Lett.* **2007**, *90*, 193506.
- [74] C. R. McNeill, J. J. M. Halls, R. Wilson, G. L. Whiting, S. Berkebile, M. G. Ramsey, R. H. Friend, N. C. Greenham, *Adv. Funct. Mater.* **2008**, *18*, 2309–2321.
- [75] C. R. McNeill, A. Abrusci, I. Hwang, M. A. Ruderer, P. Müller-Buschbaum, N. C. Greenham, *Adv. Funct. Mater.* **2009**, *19*, 3103–3111.
- [76] X. He, F. Gao, G. Tu, D. Hasko, S. Hüttner, U. Steiner, N. C. Greenham, R. H. Friend, W. T. S. Huck, *Nano Lett.* **2010**, *10*, 1302–1307.

- [77] Z. Chen, Y. Zheng, H. Yan, A. Facchetti, *J. Am. Chem. Soc.* **2009**, *131*, 8–9.
- [78] H. Yan, Z. Chen, Y. Zheng, C. Newman, J. R. Quinn, F. Dötz, M. Kastler, A. Facchetti, *Nature* **2009**, *457*, 679–687.
- [79] J. R. Moore, S. Albert-Seifried, A. Rao, S. Massip, B. Watts, D. J. Morgan, R. H. Friend, C. R. McNeill, H. Sirringhaus, *Adv. Energy Mater.* **2011**, *1*, 230–240.
- [80] M. Schubert, D. Dolfen, J. Frisch, S. Roland, R. Steyrlleuthner, B. Stiller, Z. Chen, U. Scherf, N. Koch, A. Facchetti, D. Neher, *Adv. Energy Mater.* **2012**, *2*, 369–380.
- [81] S. Fabiano, S. Himmelberger, M. Drees, Z. Chen, R. M. Altamimi, A. Salleo, M. A. Loi, A. Facchetti, *Adv. Energy Mater.* **2013**, *4*, 1301409.
- [82] M. Schubert, B. A. Collins, H. Mangold, I. A. Howard, W. Schindler, K. Vandewal, S. Roland, J. Behrends, F. Kraffert, R. Steyrlleuthner, Z. Chen, K. Fostiropoulos, R. Bittl, A. Salleo, A. Facchetti, F. Laquai, H. W. Ade, D. Neher, *Adv. Funct. Mater.* **2014**, *24*, 4068–4081.
- [83] X. Zhan, Z. Tan, B. Domercq, Z. An, X. Zhang, S. Barlow, Y. Li, D. Zhu, B. Kippelen, S. R. Marder, *J. Am. Chem. Soc.* **2007**, *129*, 7246–7247.
- [84] E. Zhou, J. Cong, M. Zhao, L. Zhang, K. Hashimoto, K. Tajima, *Chem. Commun.* **2012**, *48*, 5283–5285.
- [85] E. Zhou, J. Cong, Q. Wei, K. Tajima, C. Yang, K. Hashimoto, *Angew. Chem. Int. Ed.* **2011**, *50*, 2799–2803.
- [86] Y. Kim, E. Lim, *Polymers* **2014**, *6*, 382–407.
- [87] P. J. Flory, *J. Chem. Phys.* **1942**, *10*, 51–61.
- [88] M. L. Huggins, *J. Phys. Chem.* **1942**, *46*, 151–158.
- [89] S. C. Veenstra, J. Loos, J. M. Kroon, *Prog. Photovolt: Res. Appl.* **2007**, *15*, 727–740.
- [90] J. J. M. Halls, A. C. Arias, J. D. MacKenzie, W. Wu, M. Inbasekaran, E. P. Woo, R. H. Friend, *Adv. Mater.* **2000**, *12*, 498–502.

- [91] A. C. Arias, J. D. MacKenzie, R. Stevenson, J. J. M. Halls, M. Inbasekaran, E. P. Woo, D. Richards, R. H. Friend, *Macromolecules* **2001**, *34*, 6005–6013.
- [92] H. J. Snaith, A. C. Arias, A. C. Morteani, C. Silva, R. H. Friend, *Nano Lett.* **2002**, *2*, 1353–1357.
- [93] C. R. McNeill, B. Watts, L. Thomsen, W. J. Belcher, N. C. Greenham, P. C. Dastoor, H. Ade, *Macromolecules* **2009**, *42*, 3347–3352.
- [94] B. Friedel, C. R. McNeill, N. C. Greenham, *Chem. Mater.* **2010**, *22*, 3389–3398.
- [95] T. Earmme, Y. Hwang, N. M. Murari, S. Subramaniyan, S. A. Jenekhe, *J. Am. Chem. Soc.* **2013**, *135*, 14960–14963.
- [96] E. Zhou, J. Cong, K. Hashimoto, K. Tajima, *Adv. Mater.* **2013**, *25*, 6991–6996.
- [97] Y. Zhou, T. Kurosawa, W. Ma, Y. Guo, L. Fang, K. Vandewal, Y. Diao, C. Wang, Q. Yan, J. Reinspach, J. Mei, A. L. Appleton, G. I. Koleilat, Y. Gao, S. C. B. Mannsfeld, A. Salleo, H. Ade, D. Zhao, Z. Bao, *Adv. Mater.* **2014**, *26*, 3767–3772.
- [98] R. C. Mulherin, S. Jung, S. Huettner, K. Johnson, P. Kohn, M. Sommer, S. Allard, U. Scherf, N. C. Greenham, *Nano Lett.* **2011**, *11*, 4846–4851.
- [99] M. Sommer, H. Komber, S. Huettner, R. Mulherin, P. Kohn, N. C. Greenham, W. T. S. Huck, *Macromolecules* **2012**, *45*, 4142–4151.
- [100] K. Nakabayashi, H. Mori, *Macromolecules* **2012**, *45*, 9618–9625.
- [101] X. Liu, S. Huettner, Z. Rong, M. Sommer, R. H. Friend, *Adv. Mater.* **2012**, *24*, 669–674.
- [102] N. Zhou, H. Lin, S. J. Lou, X. Yu, P. Guo, E. F. Manley, S. Loser, P. Hartnett, H. Huang, M. R. Wasielewski, L. X. Chen, R. P. H. Chang, A. Facchetti, T. J. Marks, *Adv. Energy Mater.* **2014**, *4*, 1300785.
- [103] P. Cheng, L. Ye, X. Zhao, J. Hou, Y. Li, Z. Zhan, *Energy Environ. Sci.* **2014**, *7*, 1351–1356.

- [104] T. Earmme, Y. Hwang, S. Subramaniyan, S. A. Jenekhe, *Adv. Mater.* **2014**, *26*, 6080–6085.
- [105] S. Swaraj, C. Wang, H. Yan, B. Watts, J. Lüning, C. R. McNeill, H. Ade, *Nano Lett.* **2010**, *10*, 2863–2869.
- [106] H. Yan, B. A. Collins, E. Gann, C. Wang, H. Ade, C. R. McNeill, *ACS Nano* **2012**, *6*, 677–688.
- [107] Y. Tang, C. R. McNeill, *J. Polym. Sci. Part B: Polym. Phys.* **2013**, *51*, 403–409.



## *Part I*



## Chapter 2

# Efficient Polymer/Polymer Blend Solar Cells Developed by Thermal Purification of Nanoscale-Phase-Separated Morphology

### 2.1. Introduction

Conjugated polymer-based solar cells are attracting attention as a possible inexpensive renewable energy source, owing to their advantages such as high throughput and large-area production by solution processes.<sup>1</sup> The photovoltaic layer of the most studied polymer-based solar cells is based on a blend of a conjugated polymer acting as electron donor and a low molecular-weight fullerene derivative, PCBM, as acceptor.<sup>2</sup> On the other hand, polymer/polymer blend solar cells also have been a subject of active research<sup>3,4</sup> because they have potential advantages over polymer/fullerene blends such as more efficient light absorption due to acceptor polymers and relatively higher open-circuit voltages.<sup>4</sup> However, the power conversion efficiency (PCE) of polymer/polymer blend solar cells is still mostly lower than 2%,<sup>4</sup> which is far below that of polymer/fullerene solar

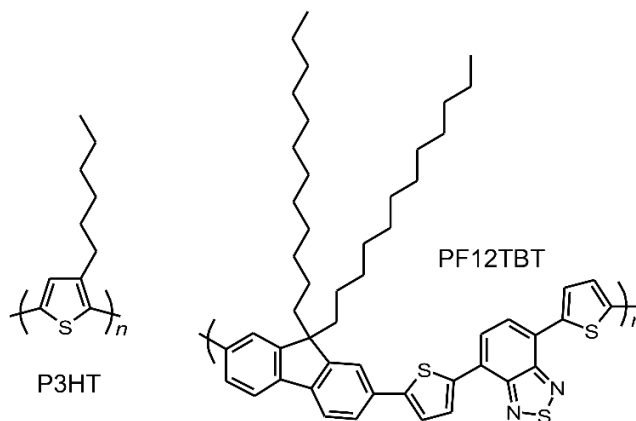


**Figure 2-1.** Chemical structures of P3HT and PF12TBT.

cells.<sup>2</sup> The relatively poor efficiency has been considered to be due to the undesired morphology of blends such as a large phase-separation,<sup>5</sup> inhomogeneous internal phase composition,<sup>6-10</sup> and reduced ordering of polymer chains.<sup>11</sup> The phase separation in polymer/polymer blends is probably different from that in polymer/fullerene blends.<sup>12,13</sup> It is therefore crucial to clarify how the blend morphology affects the device performance and how to obtain the optimal morphology that gives the best performance. In this chapter, the author demonstrates that the PCE of polymer/polymer blend solar cells consisting of poly(3-hexylthiophene) (P3HT, Figure 2-1) and poly[2,7-(9,9-didodecylfluorene)-*alt*-5,5-(4',7'-bis(2-thienyl)-2',1',3'-benzothiadiazole)] (PF12TBT, Figure 2-1) is successfully improved up to 2.0% by optimizing the phase separation.

## 2.2. Results and Discussion

Figure 2-2 shows  $J-V$  characteristics of P3HT/PF12TBT solar cells fabricated from *o*-dichlorobenzene (DCB), chlorobenzene (CB), and chloroform (CF) solutions with annealing at 140 °C for 10 min. The short-circuit current density ( $J_{SC}$ ) was as low as 1 mA cm<sup>-2</sup> for the devices from DCB and CB; these solvents are widely employed for polymer/fullerene solar cells to give a large  $J_{SC}$  and high PCE.<sup>2</sup> In contrast, a significant increase in  $J_{SC}$  up to 4 mA cm<sup>-2</sup> was observed for the device from CF, and hence PCE reached as high as 2.0%.<sup>14</sup> This is one of the best PCE values reported so far among polymer/polymer blend solar cells.<sup>15-17</sup> As shown in Figure 2-3a, the external quantum efficiency (EQE) of the device with a PCE of 2.0% was in good agreement in spectral shape with the UV-visible reflection absorption. This agreement suggests that both P3HT and PF12TBT equally contribute to the photocurrent generation. The EQE reached up to 27% at 560 nm and was still as high as 23% even at 600 nm, owing to the contribution of PF12TBT, which has an absorption peak around 575 nm (Figure 2-3b). The high EQE over

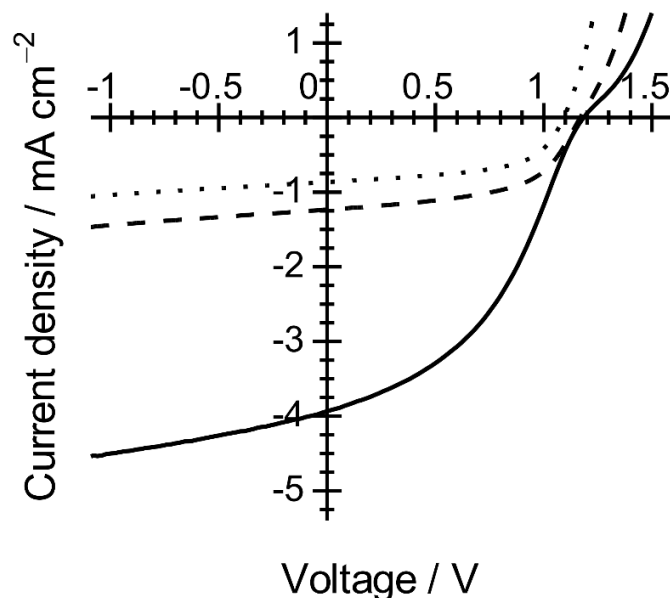


**Figure 2-2.**  $J$ - $V$  characteristics of P3HT/PF12TBT solar cells under AM 1.5G  $100 \text{ mW cm}^{-2}$  illumination. The devices were fabricated by spin-coating from DCB (dotted line), CB (dashed line), and CF (solid line) solutions and annealed at  $140 \text{ }^\circ\text{C}$  for 10 min. The device performances are summarized in Table 2-1.

600 nm can account for the PCE higher than that of another polymer/polymer blend solar cell based on P3HT and poly[2,7-(9,9-dioctylfluorene)-*alt*-5,5-(4',7'-bis(4-hexyl-2-thienyl)-2',1',3'-benzothiadiazole)] (F8TBT, see Figures 2-A1 and 2-A3 in Appendix), which is one of the most efficient polymer/polymer blend solar cells with a PCE of 1.8 – 1.9%.<sup>16,17</sup> Furthermore, the internal quantum efficiency (IQE) was higher than 30% (see Figure 2-A4 in Appendix). Such efficient photocurrent generation is partly due to energy offsets in both the HOMO and LUMO levels (0.8 eV) enough for the charge separation, as shown in the inset in Figure 2-3b. The author therefore concludes that the smaller optical band gap and larger absorption coefficient of PF12TBT than those of F8TBT (see Figure 2-A5 in Appendix) successfully leads to the significant increase in PCE in the optimized device fabricated from CF. The efficient light absorption of PF12TBT might be due to the absence

of hexyl chains at the 4-position of the thiophene, which reduces the steric hindrance and increases planarity of the polymer backbone.<sup>18</sup> The device parameters are summarized in Table 2-1.

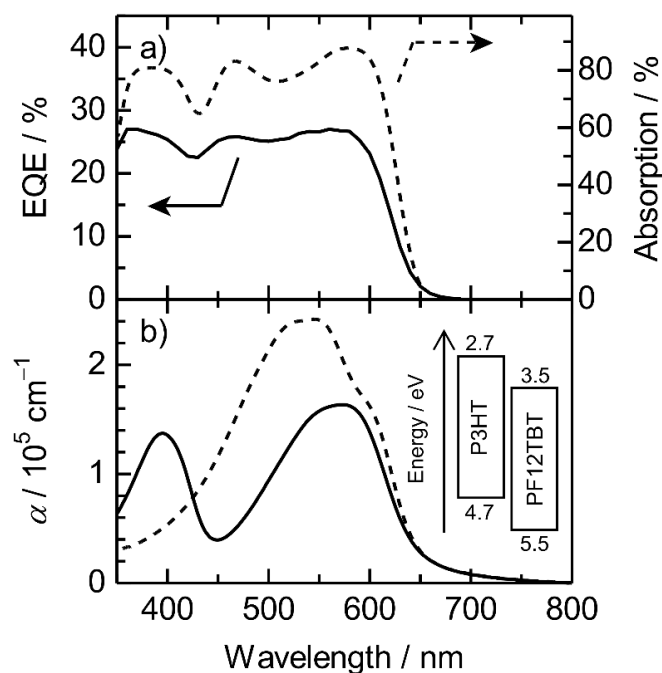


**Figure 2-3.** (a) External quantum efficiency (solid line) and the UV–visible reflection absorption (dashed line) spectra of P3HT/PF12TBT solar cell with a PCE of 2.0%. (b) Absorption coefficients ( $\alpha$ ) of P3HT (dashed line) and PF12TBT (solid line) films. The inset shows the energy level diagram of P3HT and PF12TBT: the HOMO and LUMO levels were estimated by the photoelectron yield spectroscopy and the optical energy gap.

**Table 2-1.** Device performance and photoluminescence quenching efficiency.

Solvent	$J_{SC} / \text{mA cm}^{-2}$	$V_{OC} / \text{V}$	FF	PCE / %	$\Phi_q / \%$
DCB	0.86	1.09	0.57	0.54	$45 \pm 4$
CB	1.23	1.17	0.56	0.80	$50 \pm 4$
CF	3.94	1.19	0.42	2.0	$71 \pm 4$

To address the origin of the different device performance depending on the spin-coating solvents, the author measured atomic force microscope (AFM) phase images of P3HT/PF12TBT blend films before and after thermal annealing. As shown in Figures 2-4a–c, marked difference was observed for the three blend films fabricated from different solutions before thermal annealing. For the blend film spin-coated from DCB, phase-separated structures were clearly observed: each domain was a few micrometers in lateral dimension (Figure 2-4a). For the blend film from CB, smaller but still distinct phase-separated structures were observed: each domain was a few hundred nanometers in lateral dimension (Figure 2-4b). In either case, the phase-separated domains are much larger than

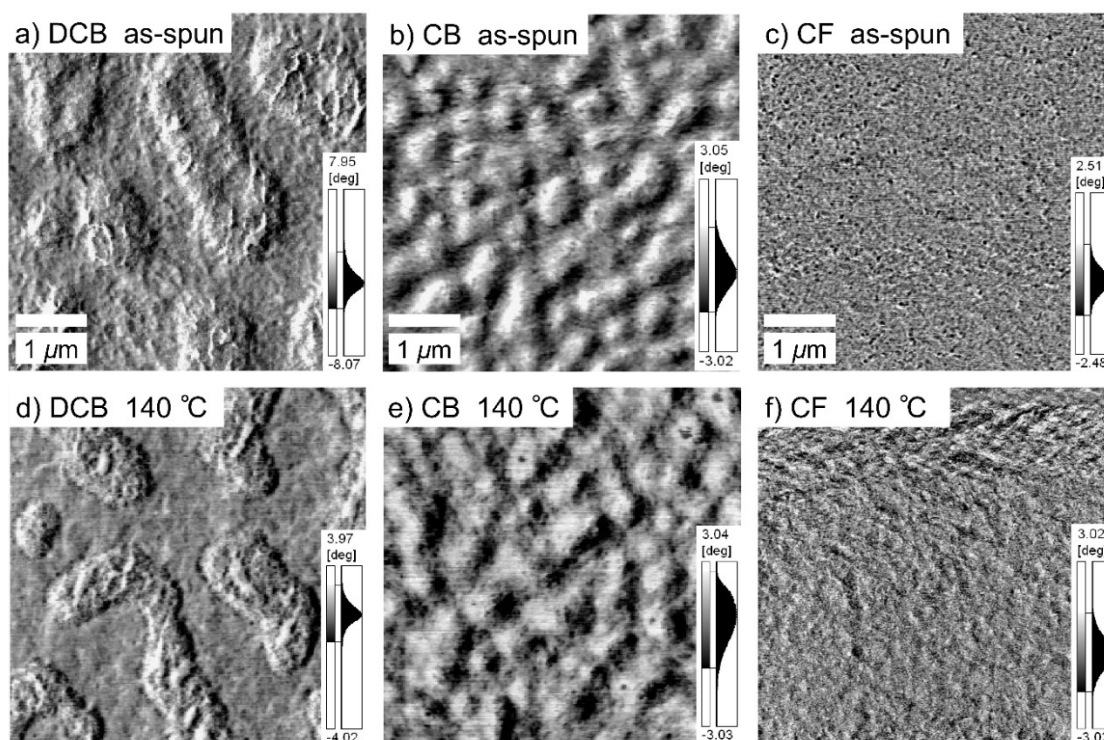


**Figure 2-4.** Tapping-mode AFM phase images ( $5 \mu\text{m} \times 5 \mu\text{m}$ ) of P3HT/PF12TBT blend films spin-coated from (a), (d) DCB, (b), (e) CB, and (c), (f) CF solutions on glass substrates. (a) – (c) As-spun films. (d) – (f) Annealed films at  $140 \text{ }^\circ\text{C}$  for 10 min. The scale bar corresponds to a length of  $1 \mu\text{m}$ .

the exciton diffusion length of typical conjugated polymers ( $\leq 10$  nm).<sup>19</sup> In contrast, no distinct phase-separated structures were observed for the blend film from CF, suggesting well-mixed blend morphology of P3HT and PF12TBT (Figure 2-4c). More importantly, as shown in Figures 2-4d–f, no distinct change in the phase-separated structures was observed for all the blend films before and after the thermal annealing. Even at 200 °C for 10 min, the thermal annealing caused little change in the surface morphology (see Figure 2-A6 in Appendix). The author therefore concludes that large-scaled phase-separated structures are less sensitive to thermal annealing but rather primarily dependent on the spin-coating solvent. The spontaneous large phase separation during spin-coating from DCB and CB solutions is one of the reasons that limit the efficiency of the devices.

The author next measured the photoluminescence (PL) quenching efficiency  $\Phi_q$  of PF12TBT in the P3HT/PF12TBT blend films before and after thermal annealing. Before the thermal annealing,  $\Phi_q$  reached to 89% for CF and was as high as 60% even for DCB and CB. The high  $\Phi_q$  for CF is consistent with well-mixed blend structures observed in the AFM image (Figure 2-4c). In contrast, the high  $\Phi_q$  observed for DCB and CB is apparently inconsistent with large phase-separated structures on a scale of micro- or sub-micrometers as shown in Figures 2-4a and 2-4b. Such disagreement has been reported for blends of conjugated polymers, suggesting that large phase-separated domains are not pure but involve minor counterpart material.<sup>3,5-9</sup> The minor counterpart isolated in the large domains just serves as a quenching site for excitons but cannot contribute to the photocurrent generation, because even if charge carriers are generated from excitons, the minor counterpart cannot transport a carrier to an electrode. This is consistent with the small  $J_{SC}$  observed for DCB and CB. Therefore it can be said that spontaneous large phase separation and undesired exciton quenching by the minor counterpart lead to small  $J_{SC}$  and thus low PCE of the devices fabricated from DCB and CB. Interestingly,  $\Phi_q$  for all the blend films decreased

after the thermal annealing: 71% for CF, 50% for CB, and 45% for DCB. This is again inconsistent with phase-separated structures observed in the AFM images: no change was observed before and after the thermal annealing. The author therefore concludes that thermal annealing does not affect large-scaled phase-separated structures but rather accelerates nanoscale phase separation that expels the minor component from the individual domains.

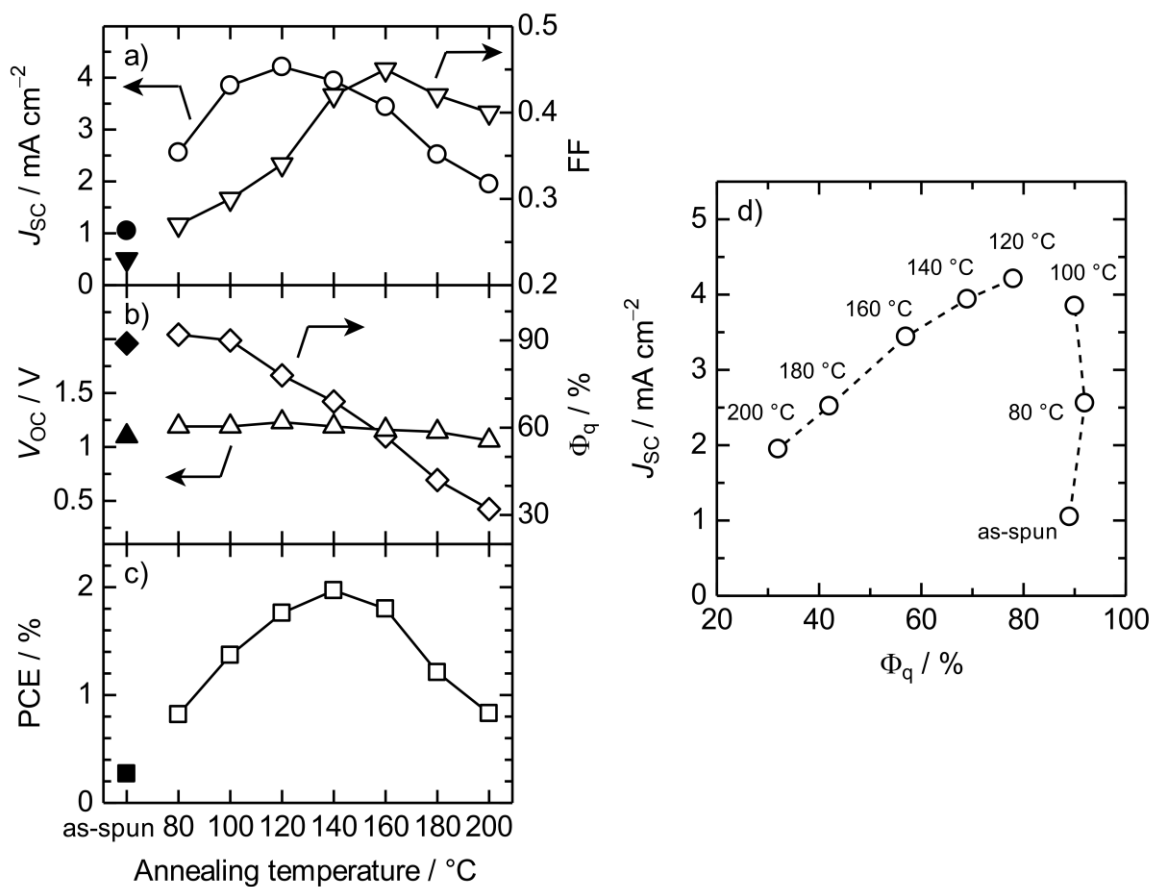


**Figure 2-5.** Dependence of the device parameters and  $\Phi_q$  on the annealing temperature: (a)  $J_{SC}$  (open circles) and FF (open inverted triangles), (b)  $V_{OC}$  (open triangles) and  $\Phi_q$  (open diamonds), and (c) PCE (open squares). The closed symbols represent the device parameters and  $\Phi_q$  before thermal annealing. (d) Plots of  $J_{SC}$  against their respective  $\Phi_q$ . These parameters were measured for P3HT/PF12TBT solar cells fabricated by spin-coating from CF.

Finally, the author focuses on the efficient device fabricated from CF to discuss the relationship between the device performance and the blend morphology in detail on the basis of the dependence of the device parameters and  $\Phi_q$  on the annealing temperature. As shown in Figure 2-5a, with increasing annealing temperature,  $J_{SC}$  increased from 1.1 mA cm<sup>-2</sup> for the as-spun device to 4.2 mA cm<sup>-2</sup> for the device annealed at 120 °C, and then decreased above it. The fill factor (FF) increased from 0.23 for the as-spun device to 0.45 for the device annealed at 160 °C, and then decreased slightly. The open-circuit voltage ( $V_{OC}$ ) was kept constant at around 1.1 to 1.2 V independently of the temperature (Figure 2-5b). Such annealing temperature dependence of  $J_{SC}$ , FF, and  $V_{OC}$  indicates that the maximum PCE at 140 °C results from the balance between  $J_{SC}$  and FF (Figure 2-5c). On the other hand,  $\Phi_q$  was as high as ~90% for the as-spun film and the annealed films at 80 and 100 °C, but as increasing annealing temperature it monotonically decreased and finally to 32% at 200 °C (Figure 2-5b). To elucidate how the nanoscale phase separation impacts on the performance,  $J_{SC}$  was replotted against the  $\Phi_q$  in Figure 2-5d. As shown in Figure 2-5d,  $J_{SC}$  steeply increased from 1.1 mA cm<sup>-2</sup> for the as-spun device to 3.9 mA cm<sup>-2</sup> for the annealed device at 100 °C even though  $\Phi_q$  remains at high ~90%. In contrast,  $J_{SC}$  decreased from 4.2 to 2.0 mA cm<sup>-2</sup> in proportion to  $\Phi_q$  for the devices annealed above 120 °C. Thermal annealing should increase the domain purity or the domain size. The improvement in the domain purity results in the increase in  $J_{SC}$  because undesirable exciton quenching is reduced and carrier transport would be improved. The growth in the domain size causes the decrease in the domain interface and hence in  $J_{SC}$ . Thus, the increase in  $J_{SC}$  below 100 °C is indicative of the improvement in the domain purity and the decrease in  $J_{SC}$  above 120 °C is ascribable to the growth in the domain size. A recent Monte Carlo simulation has demonstrated that the domain purity should be almost 100% to account for  $\Phi_q$  smaller than 90%, assuming that the domain size is less than 80 nm.<sup>20</sup> The author

therefore concludes that thermal annealing below 100 °C mainly improves the purity of small domains, and above 120 °C it further induces the growth of the purified domain in size on a nanometer scale.

### 2.3. Conclusions

The author have found that phase-separated structures on a scale of micro- or sub-micrometers are less sensitive to thermal annealing but rather primarily dependent on the spin-coating solvent, and that thermal annealing rather induces the purification of nanoscale phase-separated domains. Based on these findings, the author has fabricated highly-efficient polymer/polymer blend solar cells by spin-coating from CF with thermal annealing. The low-boiling solvent of CF gives well-mixed blend morphology consisting of nanoscale phase-separated domains. The thermal annealing improves the domain purity at low temperatures and promotes the growth of the domain size on a nanometer scale at high temperatures. The best PCE of 2.0% is achieved with an optimum phase-separated structure, which cannot be obtained from DCB and CB solutions because of the micro-scale phase-separated structures containing a minority counterpart.

### 2.4. Experimental

*Materials:* Poly(3-hexylthiophene) (P3HT,  $M_w = 42,300$ , regioregularity > 90 %) was purchased from Aldrich. Poly[2,7-(9,9-didodecylfluorene)-*alt*-5,5-(4',7'-bis(2-thienyl)-2',1',3'-benzothiadiazole)] (PF12TBT,  $M_w = 20,000$ ,  $M_w/M_n = 2.0$ ,  $T_g = 76$  °C) was developed by Sumitomo Chemical Co., Ltd.

*Device Fabrication:* Indium-tin-oxide (ITO)-coated glass substrates (10  $\Omega$  per square) were washed by ultrasonication in toluene, acetone, and ethanol for 15 min each in this order and then dried with N<sub>2</sub> flow. The washed substrates were further treated with a UV–O<sub>3</sub> cleaner

(Nippon Laser & Electronics Lab., NL-UV253S) for 30 min. A thin layer (~40 nm) of PEDOT:PSS (H. C. Starck PH500) was spin-coated onto the ITO substrate at a spin rate of 3000 rpm for 99 s and dried at 140 °C for 10 min in air. A blend layer of P3HT/PF12TBT (~70 nm) was spin-coated on the PEDOT:PSS film at 3000 rpm for 60 s from CF, at 3000 rpm for 60 s from CB, and at 1000 rpm for 180 s from DCB solution, respectively. The blend solutions were prepared by dissolving P3HT (5 mg) and PF12TBT (5 mg) in 1 mL of CF, P3HT (10 mg) and PF12TBT (10 mg) in 1 mL of CB, and P3HT (10 mg) and PF12TBT (10 mg) in 1 mL of DCB, respectively. The P3HT/PF12TBT photoactive layer was thermally annealed for 10 min in an N<sub>2</sub>-filled glove box after vacuum deposition of a lithium fluoride (LiF, 1 nm) and aluminum electrode (Al, 70 nm).

*Measurements:* The  $J$ - $V$  characteristics of the devices were measured in an N<sub>2</sub> atmosphere under AM1.5G simulated solar light at 100 mW cm<sup>-2</sup>. The light intensity was corrected with a calibrated silicon photodiode reference cell (Peccell, PECSI01). The EQE spectra were measured with a digital electrometer (Advantest, R8252) under monochromatic light illumination from a 500-W xenon lamp (Thermo Oriel, 66921) with optical cut filters and a monochromator (Thermo Oriel, UV-visible Cornerstone). The active area of the device was 0.07 cm<sup>2</sup>. The illumination was carried out from ITO side. All these measurement were performed in N<sub>2</sub> atmosphere at room temperature. At least 6 devices were fabricated to ensure reproducibility of the  $J$ - $V$  characteristics. Absolute reflectivity was measured for the device samples at an incident angle of 5° normal to the substrate (Hitachi, U-4100). The light was irradiated from the ITO side. The AFM images were collected in tapping mode (Shimadzu, SPM-9600) using silicon probes with a tip radius typically smaller than 8 nm. The PL quenching efficiency of PF12TBT was evaluated from the ratio of the PL intensity excited at 392 nm for P3HT/PF12TBT blend films to that for a PF12TBT neat film, spin-

coated on glass substrates. The HOMO level of a P3HT and PF12TBT neat film was estimated by the photoelectron yield spectroscopy (Riken Keiki, AC-3).

## 2.5. Appendix

### 2.5.1. Device Fabrication of P3HT/F8TBT Solar Cells

Poly[2,7-(9,9-dioctylfluorene)-*alt*-5,5-(4',7'-bis(4-hexyl-2-thienyl)-2',1',3'-benzothiadiazole)] (F8TBT,  $M_w = 240,000$ ,  $M_w/M_n = 2.0$ ,  $T_g = 97\text{ }^\circ\text{C}$ ) were developed by Sumitomo Chemical Co., Ltd. A blend layer of P3HT/F8TBT ( $\sim 70\text{ nm}$ ) was spin-coated on the PEDOT:PSS film at 3000 rpm for 60 s from a CF solution. The blend solution was prepared by dissolving P3HT (4 mg) and F8TBT (4 mg) in 1 mL of CF. The P3HT/F8TBT photoactive layer was thermally annealed at  $180\text{ }^\circ\text{C}$  for 10 min in an  $\text{N}_2$ -filled glove box after vacuum deposition of Ca (15 nm) and Al electrode (70 nm).

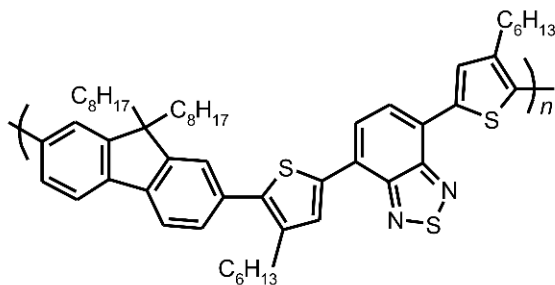


**Figure 2-A1.** Chemical structure of F8TBT.

## 2.5.2. Device Structure

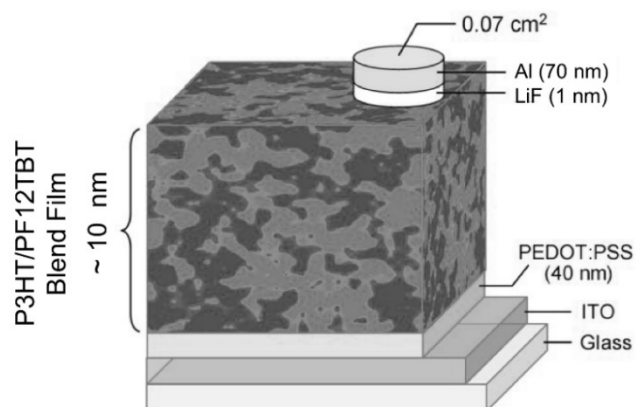


**Figure 2-A2.** Schematic illustration of a P3HT/PF12TBT solar cell.

## 2.5.3. EQE Spectra

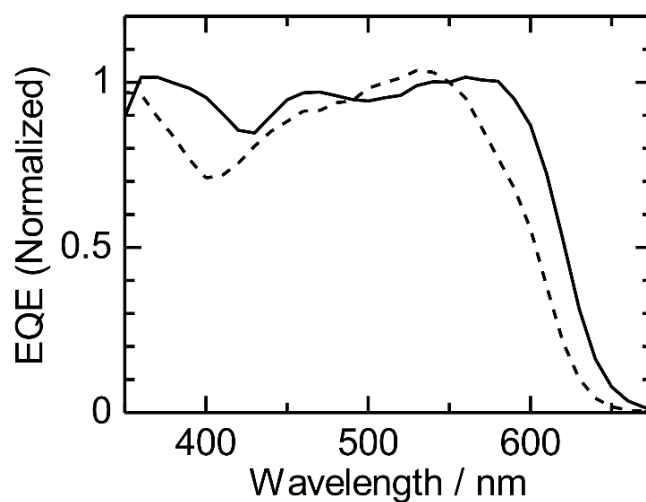


**Figure 2-A3.** Normalized EQE spectra of P3HT/PF12TBT (solid line) and P3HT/F8TBT (dashed line) blend solar cells. These devices were prepared by spin-coating from a chloroform solution of polymer blends (1:1 by weight) and annealed at 140 °C (P3HT/PF12TBT) and 180 °C (P3HT/F8TBT) for 10 min after deposition of the Al electrode. PCE of the P3HT/PF12TBT and P3HT/F8TBT solar cells in this figure are 2.0% and 1.3%, respectively.

#### 2.5.4. Internal Quantum Efficiency (IQE)

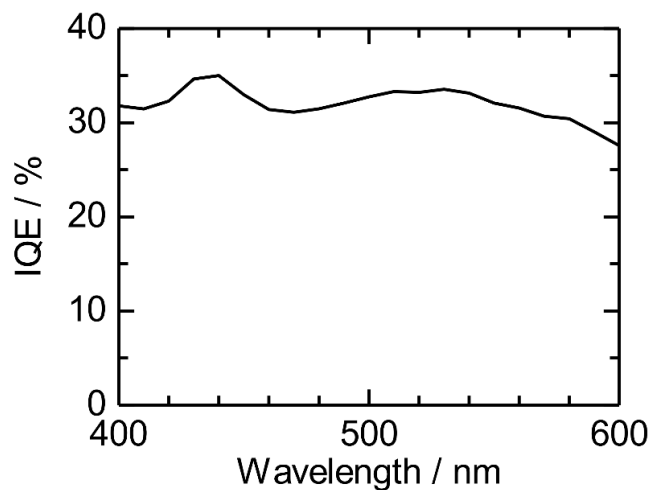


**Figure 2-A4.** Internal quantum efficiency (IQE) of P3HT/PF12TBT solar cell with PCE of 2.0%. The IQE spectrum was calculated from EQE and UV–visible reflection absorption spectrum.

#### 2.5.5. Absorption Coefficients

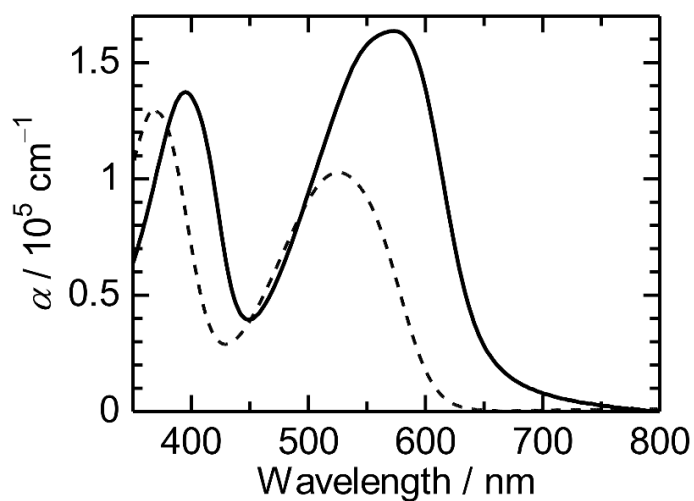


**Figure 2-A5.** Absorption coefficients ( $\alpha$ ) of PF12TBT (solid line) and F8TBT (dashed line) neat films, spin-coated from CF solution on glass substrates.

### 2.5.6. AFM Images

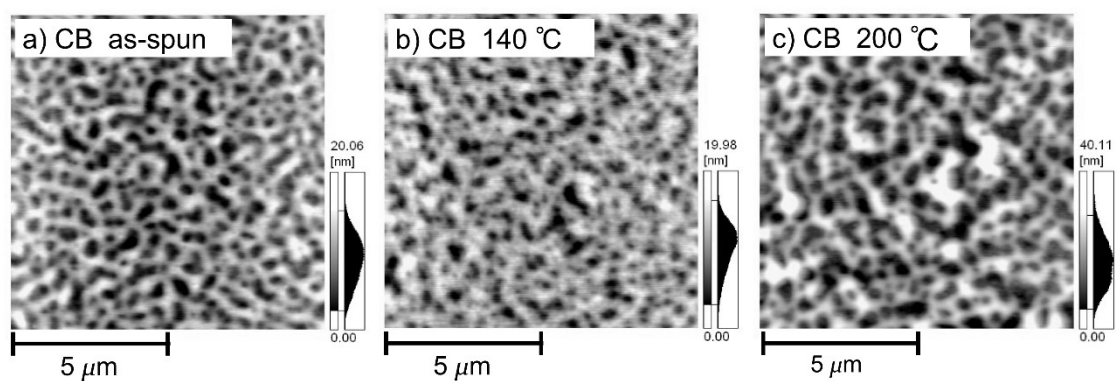


**Figure 2-A6.** Tapping-mode AFM topographic images ( $10 \mu\text{m} \times 10 \mu\text{m}$ ) of P3HT/PF12TBT blend films spin-coated from CB solution on glass substrates. (a) As-spun film, (b) annealed film at  $140 \text{ }^\circ\text{C}$  for 10 min, and (c) annealed film at  $200 \text{ }^\circ\text{C}$  for 10 min. The scale bar corresponds to a length of  $5 \mu\text{m}$ .

## 2.6. References and Note

- [1] F. C. Krebs, T. Tromholt, M. Jørgensen, *Nanoscale* **2010**, *2*, 873–886.
- [2] G. Dennler, M. C. Scharber, C. J. Brabec, *Adv. Mater.* **2009**, *21*, 1323–1338.
- [3] S. C. Veenstra, J. Loos, J. M. Kroon, *Prog. Photovolt: Res. Appl.* **2007**, *15*, 727–740.
- [4] C. R. McNeill, N. C. Greenham, *Adv. Mater.* **2009**, *21*, 3840–3850.
- [5] A. C. Arias, J. D. MacKenzie, R. Stevenson, J. J. M. Halls, M. Inbasekaran, E. P. Woo, D. Richards, R. H. Friend, *Macromolecules* **2001**, *34*, 6005–6013.
- [6] H. J. Snaith, A. C. Arias, A. C. Morteani, C. Silva, R. H. Friend, *Nano Lett.* **2002**, *2*, 1353–1357.
- [7] R. Shikler, M. Chiesa, R. H. Friend, *Macromolecules* **2006**, *39*, 5393–5399.
- [8] C. R. McNeill, B. Watts, L. Thomsen, W. J. Belcher, N. C. Greenham, R. C. Dastoor, H. Ade, *Macromolecules* **2009**, *42*, 3347–3352.
- [9] S. Swaraj, C. Wang, H. Yan, B. Watts, J. Lüning, C. R. McNeill, H. Ade, *Nano Lett.* **2010**, *10*, 2863–2869.
- [10] J. R. Moore, S. Albert-Seifried A. Rao, S. Massip, B. Watts, D. J. Morgan, R. H. Friend, C. R. McNeill, H. Sirringhaus, *Adv. Energy Mater.* **2011**, *1*, 230–240.
- [11] C. R. McNeill, A. Abrusci, I. Hwang, M. A. Ruderer, P. Müller-Buschbaum, N. C. Greenham, *Adv. Funct. Mater.* **2009**, *19*, 3103–3111.
- [12] S. Nilsson, A. Bernasik, A. Budkowski, E. Moons, *Macromolecules* **2007**, *40*, 8291–8301.
- [13] C. Müller, T. A. M. Ferenczi, M. Campoy-Quiles, J. M. Frost, D. D. C. Bradley, P. Smith, N. Stingelin-Stutzmann, J. Nelson, *Adv. Mater.* **2008**, *20*, 3510–3515.
- [14] An inflection point near  $V_{OC}$  in the  $J$ – $V$  curve measured for the device from CF would be caused by the unoptimized thickness of the LiF layer. The slightly thick LiF layer may have negative impact on the charge collection from the polymer blend to

the Al electrode.

- [15] E. Zhou, J. Cong, Q. Wei, K. Tajima, C. Yang K. Hashimoto, *Angew. Chem. Int. Ed.* **2011**, *50*, 2799–2803.
- [16] C. R. McNeill, A. Abrusci, J. Zaumseil, R. Wilson, M. J. McKiernan, J. H. Burroughes, J. J. M. Halls, N. C. Greenham, R. H. Friend, *Appl. Phys. Lett.* **2007**, *90*, 193506.
- [17] X. He, F. Gao, G. Tu, D. Hasko, S. Hüttner, U. Steiner, N. C. Greenham, R. H. Friend, W. T. S. Huck, *Nano Lett.* **2010**, *10*, 1302–1307.
- [18] W. Li, R. Qin, Y. Zhou, M. Andersson, F. Li, C. Zhang, B. Li, Z. Liu, Z. Bo, F. Zhang, *Polymer* **2010**, *51*, 3031–3038.
- [19] D. E. Markov, E. Amsterdam, P. W. M. Blom, A. B. Sieval, J. C. J. Hummelen, *Phys. Chem. A* **2005**, *109*, 5266–5274.
- [20] C. R. McNeill, S. Westenhoff, C. Groves, R. H. Friend, N. C. Greenham, *J. Phys. Chem. C* **2007**, *111*, 19153–19160.

## Chapter 3

# Charge Generation and Recombination Dynamics in Efficient Polymer/Polymer Blend Solar Cells with Nanoscale-Phase-Separated Morphology

### 3.1. Introduction

Conjugated polymer-based solar cells have gained increasing attention as an inexpensive source of renewable energy because of their high throughput and the relatively low expense of printing samples with a large area.<sup>1</sup> The most widely studied polymer-based solar cells have a bulk-heterojunction (BHJ) structure in which a polymer acting as an electron donor is mixed with an electron acceptor, typically a low-molecular-weight fullerene derivative, such as [6,6]-phenyl-C<sub>61</sub>-butyric acid methyl ester (PCBM).<sup>2,3</sup> On the other hand, polymer/polymer BHJ solar cells, which consist of a donor polymer and an acceptor polymer, have also been a subject of active research because they yield several potential advantages over conventional polymer/fullerene devices.<sup>4-6</sup> For example, flexibility in molecular design of both donor and acceptor polymers allows for the fine tuning of optical, electronic, and morphological properties. However, despite these attractive features, the developments of polymer/polymer BHJ solar cells have been lagged far behind the polymer/fullerene counterparts<sup>7,8</sup> and their power conversion efficiencies (PCEs) have remained 2% over the last decade.<sup>9-11</sup>

A great deal of synthetic effort of acceptor polymers has been dedicated toward the design of efficient donor/acceptor polymer combinations and optimizing their blend morphology.<sup>4,6,12-15</sup> Fluorene and benzothiadiazole-based copolymers are one of the promising candidates for acceptor materials alternative to fullerenes,<sup>9,10,16-18</sup> because of their

large absorption coefficients in the visible region and higher energy levels of the lowest unoccupied molecular orbital (LUMO); these features in turn increase light absorption and open-circuit voltages ( $V_{oc}$ ), respectively. In Chapter 2, the author reported a polymer/polymer BHJ solar cell containing poly(3-hexylthiophene) (P3HT) as the donor and poly[2,7-(9,9-didodecylfluorene)-*alt*-5,5-(4',7'-bis(2-thienyl)-2',1',3'-benzothiadiazole)] (PF12TBT) as the acceptor (Figure 3-1a).<sup>9,10</sup> For this P3HT/PF12TBT blend system, the energy difference between the highest occupied molecular orbital (HOMO) of the donor and

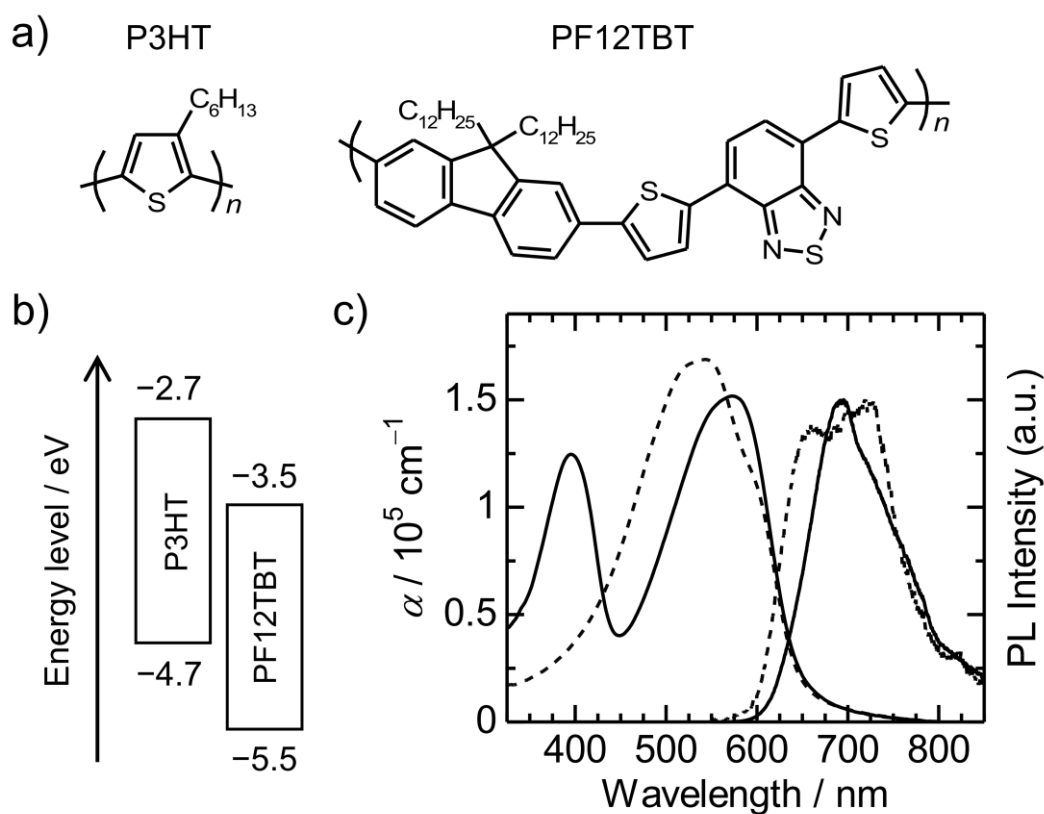


**Figure 3-1.** (a) Chemical structures of P3HT and PF12TBT. (b) Energy level diagram of P3HT and PF12TBT neat films. HOMO levels were determined by photoelectron yield spectroscopy, while LUMO levels were estimated by adding the optical bandgap energy, calculated from the 0-0 transition, to the HOMO energy. (c) Absorption coefficients ( $\alpha$ ) and photoluminescence spectra of P3HT (broken line) and PF12TBT (solid line) neat films.

the LUMO of the acceptor is larger than 1 eV. Moreover, the 0.8 eV offset between the two LUMOs allowed for efficient charge transfer (Figure 3-1b). As expected, a higher  $V_{OC}$  of 1.2 V is obtained compared to that of P3HT/PCBM blend devices ( $V_{OC} \sim 0.6$  V). Thermal annealing of well-mixed blend films improves both the short-circuit current density ( $J_{SC}$ ) and the fill factor (FF), resulting in the enhancement of PCE. However, the maximum external quantum efficiency (EQE) of the device is still lower than 30%,<sup>9</sup> which is far below the EQE of 70 – 80% reported for P3HT/PCBM devices.<sup>2</sup> Note that the potential PCE would exceed 7% owing to the high  $V_{OC}$ , if the EQE comparable to P3HT/PCBM are achieved by the further optimization.

The relatively poor EQE is not specific to the P3HT/PF12TBT blend system but is rather common for other combinations of donor and acceptor polymers.<sup>16–22</sup> Such low EQEs of polymer/polymer BHJ solar cells are considered to be due to substantial charge loss by geminate recombination, which might be inherent to the molecular electronic structure at the polymer/polymer interface<sup>23</sup> and/or the result of phase separation due to non-optimized morphology.<sup>19–22</sup> It is therefore necessary to gain a better understanding of the photovoltaic conversion processes in the nanoscale phase-separated morphology of blend films. In Chapter 2, the charge generation efficiency and blend morphology were discussed on the basis of steady-state photoluminescence quenching measurements. In this chapter, the influence of the blend morphology on the charge generation and recombination dynamics is examined in detail by femtosecond to nanosecond transient absorption (TA) measurements. In addition, charge-carrier mobility measurements are also conducted to study the morphological evolution of the PF12TBT and P3HT domains caused by thermal annealing. As a result, the author has found that the free carrier generation efficiency is increased by both the purification and the growth of nanoscale phase-separated domains, leading to the improvement in the photovoltaic performances.

## 3.2. Results

### 3.2.1. Influence of Thermal Annealing on External Quantum Efficiency

The author first examined the influence of thermal annealing on EQEs of P3HT/PF12TBT BHJ solar cells. Figures 3-2a and b show the EQE spectra and the corresponding values at 400 nm for various annealing temperatures. At this wavelength, PF12TBT mainly contributes to the photocurrent generation because 73%<sup>24</sup> of the absorbed photons by the P3HT/PF12TBT (50:50, w/w) blend film is owed to absorption of PF12TBT. As shown in Figure 3-2, the EQEs were varied sensitively by thermal annealing: the EQE at 400 nm increased from 8% for the as-spun (un-annealed) device to 27% for the device annealed at 80 – 120 °C, and then decreased to 18% for the device annealed at 160 °C.

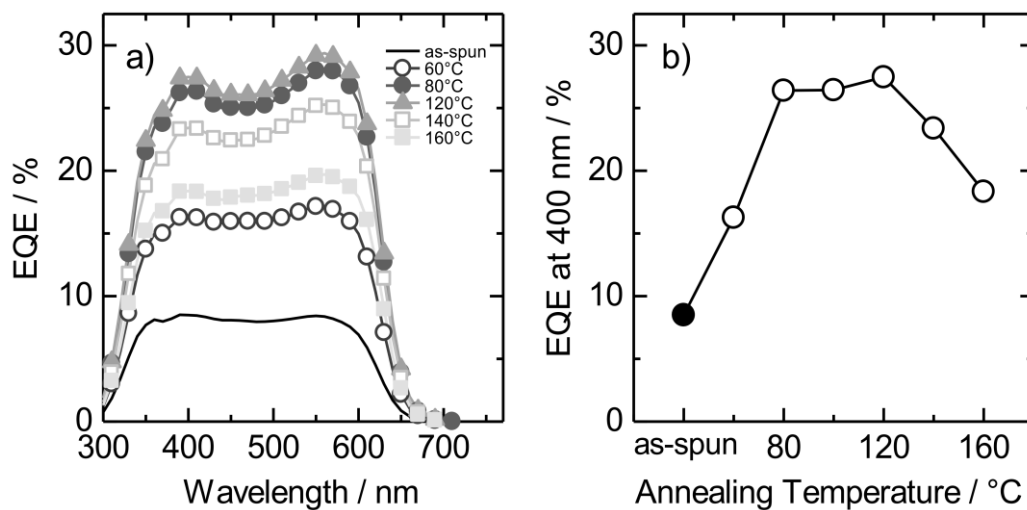


**Figure 3-2.** (a) EQE spectra of P3HT/PF12TBT BHJ solar cells annealed at various temperatures. (b) The annealing temperature dependence of EQE at 400 nm.

### 3.2.2. Temperature Dependence of Photoluminescence Quenching Efficiency

The author utilized steady-state photoluminescence (PL) quenching as a probe of the charge generation efficiency in the blend films. Figure 3-3 shows the PL spectra of a PF12TBT neat and P3HT/PF12TBT blend films excited mainly PF12TBT at 392 nm: the excitation fraction of PF12TBT was 75%. A PF12TBT neat film showed strong PL with a peak centered at 695 nm. On the other hand, the PL intensity in the as-spun blend film showed a significant decrease in comparison to that of the PF12TBT neat film, indicating efficient charge generation from the excited state of PF12TBT. The PL intensity of annealed blend films, however, recovered as temperature is higher. Annealing-temperature dependence of PL quenching efficiency ( $\Phi_q$ ) is shown in Figure 3-3b. The  $\Phi_q$  was as high as 85 – 90% for the as-spun film and the annealed films at 60 – 80 °C, but with increasing the temperature, it monotonically decreased and finally was as low as 50% at 160 °C.

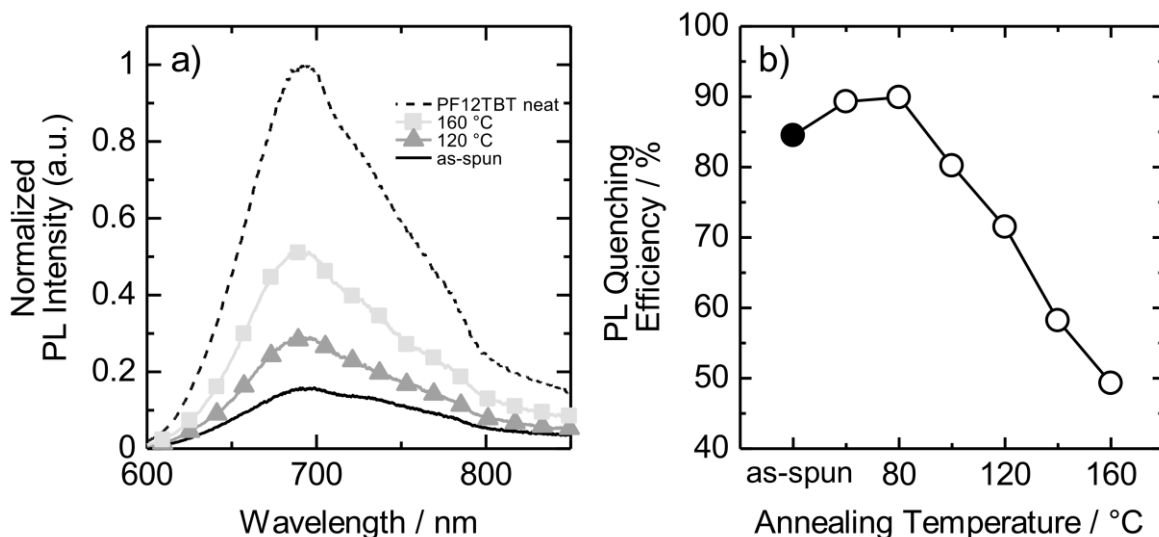


**Figure 3-3.** (a) The PL spectra of PF12TBT neat and P3HT/PF12TBT blend films excited at 392 nm. (b) The annealing temperature dependence of PL quenching efficiency of P3HT/PF12TBT blend films.

### 3.2.3. Temperature Dependence of Charge-Carrier Mobility

Charge-carrier mobilities for both the neat and blend films were measured to study the morphological evolution of PF12TBT and P3HT domains caused by thermal annealing. Electron mobility  $\mu_e$  of PF12TBT was decreased by a factor of 4, from  $2.9 \times 10^{-5}$  to  $0.66 \times 10^{-5} \text{ cm}^2 \text{ V}^{-1} \text{ s}^{-1}$ , by blending with P3HT. On the other hand, hole mobility  $\mu_h$  of P3HT was decreased by more than a factor of 20, from  $25 \times 10^{-5}$  to  $1.2 \times 10^{-5} \text{ cm}^2 \text{ V}^{-1} \text{ s}^{-1}$ , by blending with PF12TBT. Figure 3-4 shows the dependence of charge-carrier mobilities on the annealing temperature.  $\mu_e$  of blend films increased with temperature, reaching  $1.8 \times 10^{-5} \text{ cm}^2 \text{ V}^{-1} \text{ s}^{-1}$  at  $120 \text{ }^\circ\text{C}$ ; this is close very close to the value of the PF12TBT neat film.  $\mu_h$  of blend films was insensitive to thermal annealing at temperatures up to  $80 \text{ }^\circ\text{C}$ , but it increased at temperatures above  $80 \text{ }^\circ\text{C}$ . The blend film annealed at  $120 \text{ }^\circ\text{C}$  showed an improved  $\mu_h$  almost 10 times greater than the as-spun blend film.

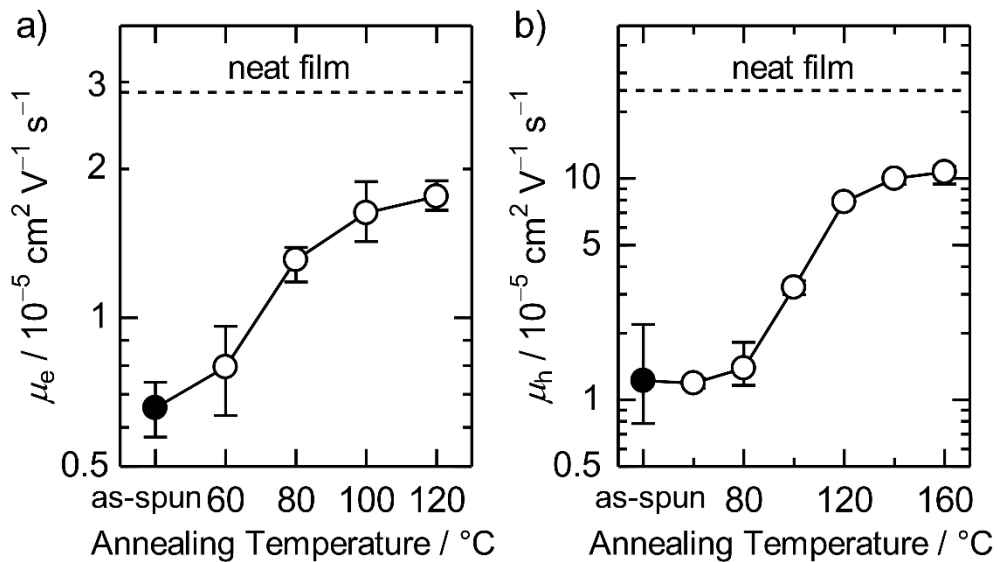


**Figure 3-4.** (a) Electron and (b) hole mobility of P3HT/PF12TBT blend films with respect to annealing temperature. The dotted lines in each figure indicate mobility values of PF12TBT and P3HT neat films, respectively.

### 3.2.4. Transient Absorption Spectra

#### A. Neat Films

The author next investigated the photovoltaic conversion processes by transient absorption spectroscopy to study the kinetics of charge generation and recombination in the P3HT/PF12TBT blend films. Figure 3-5 shows the TA spectra of the P3HT and PF12TBT neat films measured at 0.5, 10, 100, and 3000 ps after excitation at a wavelength of 400 nm. P3HT (Figure 3-5a) showed a negative TA signal below 650 nm, with distinct vibronic peaks at 560 and 610 nm; this is attributed to the transient ground-state bleach (GSB), which was determined by comparing the data with the steady-state absorption spectrum (Figure 3-1c). Meanwhile, the weak negative signal in the PL region (650 – 800 nm) is due to stimulated

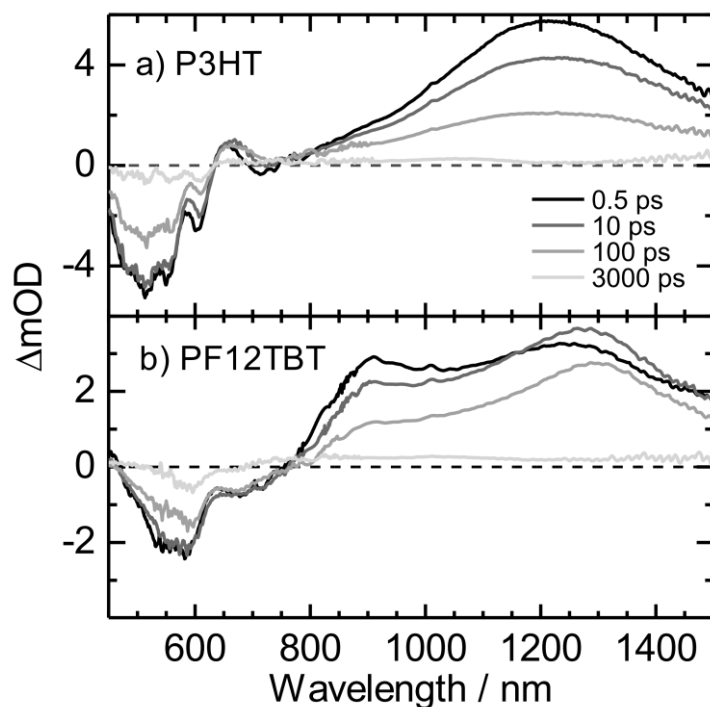


**Figure 3-5.** TA spectra for the (a) P3HT and (b) PF12TBT neat films measured at delay times of 0.5 ps, 10 ps, 100 ps, and 3000 ps after excitation. The excitation wavelength was 400 nm and the fluence was  $7.5 \mu\text{J cm}^{-2}$ . The  $\Delta\text{OD}$  values were corrected for variations in absorptions at 400 nm. The black dashed line indicates  $\Delta\text{OD} = 0$ .

emission (SE) from the P3HT singlet excitons. On the other hand, the broad TA signal which covers the entire NIR wavelength range of 800 – 1500 nm and peaks at 1200 nm is assigned to P3HT singlet excitons.<sup>25,26</sup> PF12TBT (Figure 3-5b) also gave a negative TA signal at wavelengths shorter than 650 nm; again, this is likely the result of the GSB. Similarly, the negative signal at 650 – 800 nm is the result of the SE from PF12TBT singlet excitons. The positive TA signal featured with bimodal peaks at 900 nm and 1200 – 1300 nm is assigned to PF12TBT singlet excitons; this was evident due to the fact that the TA signal showed the same decay lifetime as the SE signal (see Figure 3-A1 in Appendix). The change in the relative TA intensity ( $\Delta OD$ ) between these two peaks observed within the first 10 ps is ascribed to the relaxation of singlet excitons from the higher energy excitonic state to the lower energy intramolecular charge transfer state<sup>27</sup> (see Appendix).

## B. Blend Films

The author first simulated TA spectra of a blend film, assuming no interactions between the excited states of P3HT and PF12TBT. Figure 3-6a shows the simulated TA spectra of a P3HT/PF12TBT blend film: they are constructed by adding the corresponding TA spectra of the two neat films at the same delay time after correcting for the previously calculated excitation fractions. Meanwhile, Figure 3-6b shows the TA spectra of the as-spun P3HT/PF12TBT blend films. The as-spun blend film showed the spectral features clearly different from the simulated spectra. Even within the 0.5 ps after excitation, the positive TA signal was observed at 650 – 800 nm, where slightly negative TA due to SE was expected from the simulated spectra. The positive TA signal increased in intensity until 100 ps after excitation, while the TA signal of singlet excitons at around 1200 – 1300 nm decreased. After 3000 ps, the new transient species was clearly distinguished from the

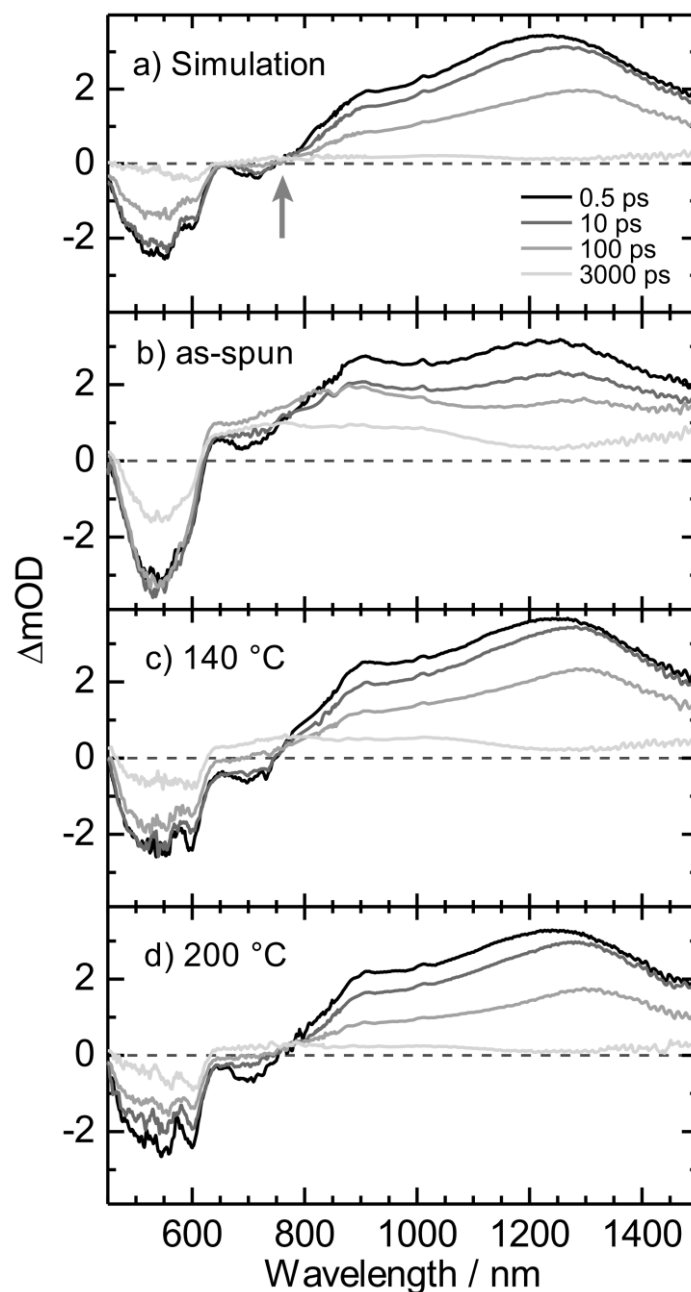


**Figure 3-6.** (a) Simulated TA spectra for the P3HT/PF12TBT blend film calculated by adding the weighted TA spectra of P3HT and PF12TBT neat films. The arrow indicates a wavelength at 760 nm. TA spectra for (b) as-spun, (c) 140 °C-annealed, and (d) 200 °C-annealed P3HT/PF12TBT blend films measured at delay times of 0.5 ps, 10 ps, 100 ps, and 3000 ps after excitation. The excitation wavelength was 400 nm and the excitation pulse intensity was  $7.5 \mu\text{J cm}^{-2}$ . The  $\Delta\text{OD}$  values were corrected for variations in absorptions at 400 nm. The black dashed lines indicate for  $\Delta\text{OD} = 0$ .

singlet excitons. This long-lived signal from 650 to 1200 nm is assigned to the charge induced absorption of both the P3HT hole and PF12TBT electron polarons. The spectral assignment for these polarons is shown in Appendix. Overall, this suggests that the positive TA signal of initially formed charges overlaps with the negative SE signals. The SE contribution then decreases as the conversion of singlet excitons into charges proceeds, and then a TA feature of charges became dominant in the wavelength range of 650 – 1200 nm at longer delay times.

The TA spectra of the blend film annealed at 140 °C (Figure 3-6c) matched the simulated spectra initially, and then slowly developed a long-lived TA signal. On the other hand, the TA spectra of the blend film annealed at 200 °C (Figure 3-6d) were almost identical to the simulated spectra throughout the time range, indicating that most of the singlet excitons decayed to the ground state without being converted into charges. In addition, the spectral shape of the GSB changed due to thermal annealing; the as-spun blend film showed structureless GSB spectra, while the annealed blend films contained more pronounced vibronic structures due to  $\pi$ -stacking of the P3HT chains.<sup>25,28,29</sup> These TA spectra show that charges are formed in the blend films but their generation yield and kinetics are influenced by the thermal annealing.

### 3.2.5. Charge Generation and Recombination Dynamics

#### A. As-spun Blend Film

The author first shows the charge generation and recombination dynamics in the as-spun blend film in this section, and then discuss the dependence of their dynamics on annealing temperature in the next section. As described above, the TA signal from charges is clearly observed in the blend films at the wavelength range of 650 – 800 nm, where positive signals are not expected from the simulated spectra. Note that the simulated

spectra in Figure 3-6a show a TA intensity of effectively zero for a wavelength of 760 nm over the whole time range, an effect that results from negligible contributions from both constituent materials. Therefore, the generation and recombination kinetics of the transient species that are additionally generated in the blend films can be extracted by tracking the time evolution of the TA signal at this wavelength. The corresponding time evolution for the as-spun blend film is shown in Figure 3-7 as open circles. The author first focuses on the time domain shorter than 150 ps, where charge generation kinetics are highlighted. In the as-spun blend film, 64% of charges generated promptly within 0.5 ps and subsequent generation of the remaining charges almost completed within 50 ps after excitation. The

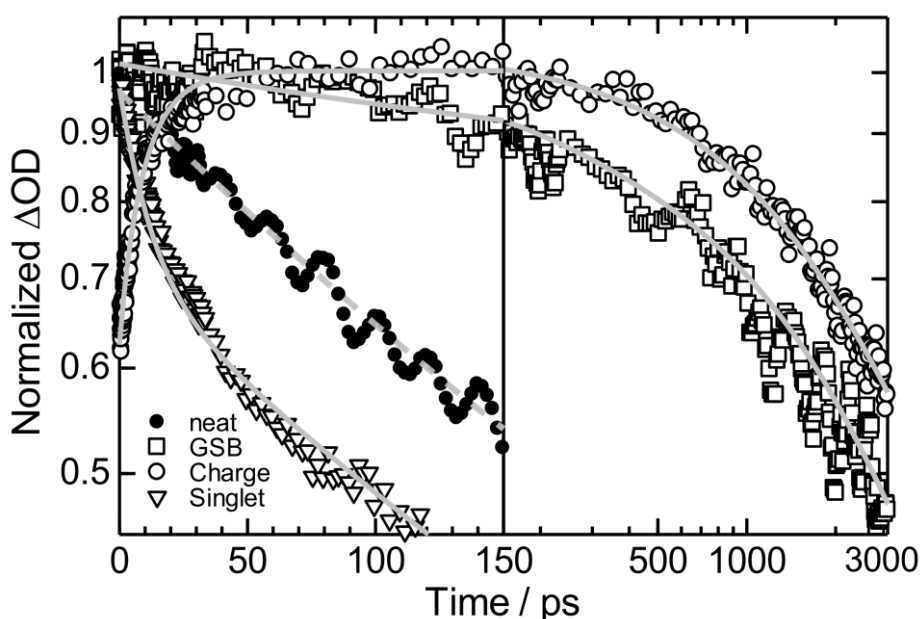


**Figure 3-7.** Normalized TA signals in the as-spun blend film: the charge induced absorption (open circles), singlet excitons (open triangles), and the GSB (open squares) observed at 760 nm, 1200 nm, and 550 nm, respectively. The closed circles show the TA signal of singlet excitons recorded at 1200 nm in the PF12TBT neat film. The  $\Delta OD$  was normalized, with the maximum intensities set to 1. The gray solid lines represent the best fitting curves, while the gray dashed line tracks exponential decay with a lifetime of 190 ps. The excitation wavelength was 400 nm and the excitation fluence was  $7.5 \mu J cm^{-2}$ .

charge generation dynamics can be fitted by Equation (1) with a rise time ( $\tau_R$ ) of 11 ps:

$$\Delta OD(t) = A [1 - \exp(-t/\tau_R)] + B \quad (1)$$

On the other hand, the TA signal from singlet excitons, monitored at 1200 nm, showed two exponential decay lifetimes (Figure 3-7, open triangles); one was 11 ps, the same as  $\tau_R$ , while the other was 190 ps. The longer lifetime of 190 ps matches the lifetime of the PF12TBT singlet excitons measured under identical excitation fluence (Figure 3-7, closed circles). Meanwhile, the GSB TA intensity measured at 550 nm (Figure 3-7, open squares) recovered slightly with the lifetime of 190 ps, while the corresponding TA intensity of charges still remained constant. These data suggest that some fraction of the PF12TBT excitons decay to the ground state without dissociating into charges, which agrees with the incomplete PL quenching of PF12TBT as mentioned above.

The author next focuses on the recombination kinetics of the charges over a longer range of delay times, from 150 to 3000 ps. The decay dynamics monitored at 760 nm can be fitted by Equation (2), with a lifetime  $\tau_D$  of 2500 ps (64 %) and a constant (36%):

$$\Delta OD(t) = G \exp(-t/\tau_D) + C \quad (2)$$

On the other hand, the kinetics for the corresponding GSB recovery are described by two exponential functions (72%) and a constant (28%). The major component of the recovery has a lifetime of 2500 ps (61%), while the minor component has a lifetime of 190 ps (11%), which well correspond to the decay lifetime of charges and the PF12TBT singlet excitons, respectively. By subtracting the contribution of the minor component from the total GSB recovery, the author calculated that the fraction of the major component was 68% and that of constant was 32%, which were very close to the decay (64%) and constant (36%) fractions shown by the recombination dynamics of charges at 760 nm. The author therefore concludes that charges are not transformed into triplet excitons, back to the ground state.

In addition, the TA signals observed in the microsecond time domain were not quenched in an oxygen atmosphere, suggesting that no triplet excitons were generated through recombination of the charge carriers (see Figure 3-A3 in Appendix).

Recombination dynamics were further investigated by examining the dependence of  $\tau_D$  on fluence. Monomolecular recombination occurs at the same rate irrespective of charge density  $n(t)$ , while the rate depends on  $n(t)$  if bimolecular recombination is the dominant process. Figure 3-8 shows the decay dynamics under different  $n(t)$  measured for excitation fluences ranging from 1.5, 2.0, and 3.8  $\mu\text{J cm}^{-2}$  ( $n(t)$  was calculated as described in Appendix). Overall, the  $n(t)$  varied linearly with excitation fluences. However, the decay dynamics were independent of  $n(t)$  and charges decayed monoexponentially with an inverse rate of 2500 ps, even at a fluence as low as 1.5  $\mu\text{J cm}^{-2}$ . Therefore, monomolecular charge

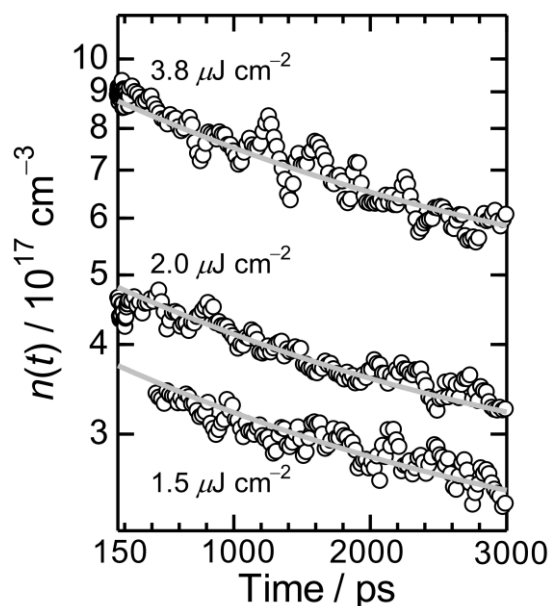


**Figure 3-8.** The dependence of charge recombination dynamics on fluence for the as-spun P3HT/PF12TBT blend film, observed at a wavelength of 760 nm. The solid lines represent single exponential fits with an inverse rate of 2500 ps. The excitation wavelength was 400 nm, with excitation fluences of 1.5, 2.0, and 3.8  $\mu\text{J cm}^{-2}$ .

recombination occurs predominantly in the sub-nanosecond to several nanosecond range.<sup>30,31</sup> Meanwhile, the charges represented by C in Equation (2) began to decay after tens of nanoseconds; these are assigned to bimolecularly recombining free charges, as described in the next section.

## B. Annealed Blend Films

The author next investigated the annealing-temperature dependence of the charge generation and recombination dynamics. Figure 3-9 shows the kinetics of charge generation monitored at a wavelength of 760 nm for the blend films annealed at various temperatures. As mentioned before, all blend films showed both the prompt and delayed charge generation, which can be described using Equation (1). The fitting parameters are summarized in Table 3-1, which shows influence from thermal annealing. As temperature increased, the generation time  $\tau_R$  increases, while the amount of total generated charges (amplitude of the maximum  $\Delta OD$ ) decreased. The fraction of promptly generated charges, defined as  $B/(A+B)$ , decreased as well, meaning that charge generation became increasingly dominated by the delayed process.

**Table 3-1.** Fitting parameters of the charge generation dynamics shown in Figure 3-9, obtained using Equation (1).

Anneal. Temp.	As-spun	60 °C	80 °C	100 °C	120 °C	140 °C	160 °C
$\tau_R$ / ps	11	14	13	33	87	126	182
A/(A+B)	36%	38%	40%	42%	49%	63%	69%
B/(A+B)	64%	62%	60%	58%	51%	37%	31%

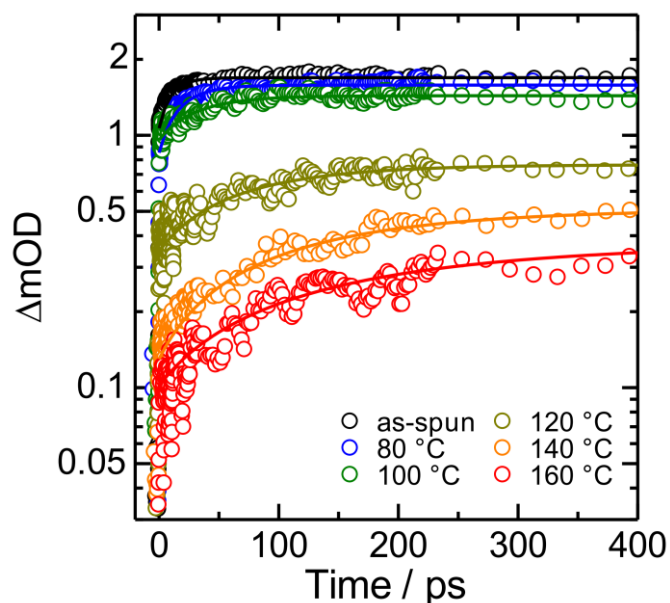


**Figure 3-9.** The dependence of charge generation dynamics on annealing temperature, observed at a wavelength of 760 nm. The solid lines represent the best fitting curves. The excitation wavelength was 400 nm and the excitation fluence was  $7.5 \mu\text{J cm}^{-2}$ . The  $\Delta\text{OD}$  values were corrected for variations in absorption at 400 nm.

Figure 3-10 shows the decay dynamics of charges, following to the charge generation as shown in Figure 3-9. The decay profiles were also influenced by thermal annealing, and were fitted by Equation (2), as shown by the solid lines; fitting parameters are summarized in Table 3-2. The fraction of monomolecular recombination, represented by  $G/(G+C)$ , decreased from 64% for the as-spun blend film to 26% for the blend film annealed at 160 °C, while the decay lifetime  $\tau_D$  is insensitive to the annealing temperature. These results reveal that thermal annealing suppresses the monomolecular decay of charges and non-decaying (long-lived) charges become to be more dominant. The author therefore tracked the long-lived charges represented by C in Equation (2) by measuring the dynamics over a wider time domain of several tens of nanoseconds, and showed that they decayed in this time frame. Moreover, the decay dynamics were dependent on the excitation fluence (see Figure 3-A5 in Appendix). These results reveal that bimolecular (nongeminate)

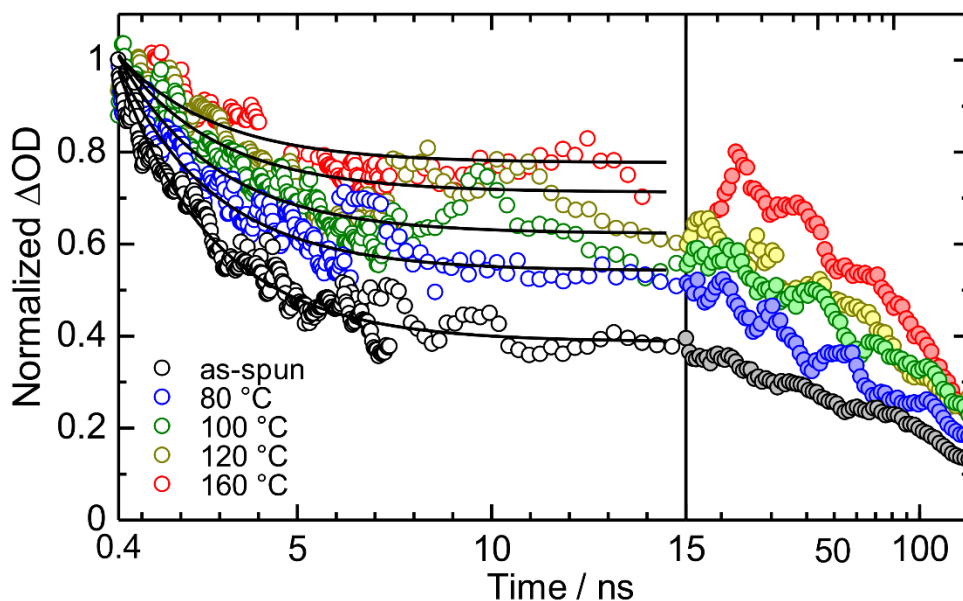


**Figure 3-10.** The dependence of charge recombination dynamics on annealing temperature, observed at a wavelength of 760 nm. The solid lines represent the best fitting curves. The excitation wavelength was 400 nm and the excitation fluence was  $3.8 \mu\text{J cm}^{-2}$ .

charge recombination occurs on a time scale of several tens of nanoseconds. Therefore, the non-decaying charges can be assigned to the spatially-separated free charges.<sup>30</sup> On the basis of these assignments, the generation efficiency for the free charges ( $\eta_{\text{free}}$ ) from fraction C can be estimated; overall,  $\eta_{\text{free}}$  increased by thermal annealing from 36% for the as-spun blend film to 74% for the sample annealed at 160 °C.

**Table 3-2.** Fitting parameters of the geminate recombination shown in Figure 3-10, obtained using Equation (2).

Anneal. Temp.	As-spun	60 °C	80 °C	100 °C	120 °C	140 °C	160 °C
$\tau_D$ / ps	2500	2500	2500	2500	2500	2500	2500
G/(G+C)	64%	58%	49%	42%	33%	37%	26%
C/(G+C)	36%	42%	51%	58%	67%	63%	74%

### 3.3. Discussion

#### 3.3.1. Development of Nanoscale Phase Separation by Thermal Annealing

All P3HT/PF12TBT blend films show charge generation dynamics characterized by the prompt charge generation on a time scale of less than 0.5 ps and the subsequent delayed charge generation that ends from tens to hundreds of picoseconds, depending on the annealing temperature. The prompt charge generation is likely the result of singlet excitons formed directly on the polymer chains adjacent to the donor/acceptor domain interfaces and/or on the isolated polymer chains in the matrix of the other polymer. The existence of the prompt charge generation for all the blend films demonstrates that charge transfer at the interface occurs so quickly that it does not limit the overall charge generation rate, as has been reported for polymer/PCBM blend films.<sup>26,30,31</sup> The efficient charge transfer between PF12TBT and P3HT is consistent with the sufficient LUMO–LUMO and/or HOMO–HOMO energy offsets of 0.8 eV. On the other hand, delayed charge generation is attributed to a diffusion-controlled process, which should be influenced by the nanomorphology of the blend films. Assuming that charge generation is diffusion limited,  $\tau_R$  represents the migration time of the singlet excitons to reach the distributed heterojunction interfaces.<sup>30</sup> The mean distance that polymer excitons must diffuse to an interface prior to dissociation is calculated from the equation  $r = \sqrt{6D\tau_R}$ ,<sup>32</sup> where  $D$  is the diffusion coefficient of singlet excitons. The  $r$  values calculated using the reported  $D$  value of PF12TBT ( $D = 9.8 \times 10^{-4} \text{ cm}^2 \text{ s}^{-1}$ )<sup>33</sup> were plotted as a function of annealing temperature in Figure 3-11a.

The author discusses the size and quality of the nanoscale-phase-separated domains on the basis of  $r$  and charge carrier mobilities of the blend films. Before thermal annealing, the value of  $r$  was estimated to be approximately 3 nm. This suggests that, in the as-spun blend film, P3HT and PF12TBT are well mixed with each other on the length scale shorter than the typical exciton diffusion length of polymers.<sup>32–35</sup> The value of  $r$  shows a weak

dependence on thermal annealing at temperatures below 80 °C, and it increases steeply above 80 °C, representing that domain growth is accelerated at temperatures above this point. This coarsening of phase separation is in agreement with the glass transition temperature  $T_g$  of PF12TBT (76 °C).<sup>9,10</sup> Above  $T_g$  of at least one of polymers in the blend film, the polymer chain becomes more mobile and can redistribute to decrease the free energy of the system, resulting in demixing of polymers.<sup>[36]</sup>

The electron and hole mobilities of the blend films provide additional information regarding the morphological evolution. The fact that  $\mu_e$  increases steadily even at temperatures below 80 °C, suggesting that the PF12TBT-rich domains increase in purity, even if domain coarsening is frozen. The electron transport will be improved by the exclusion of the isolated P3HT chains from the PF12TBT domains. Meanwhile, the significant decreased in  $\mu_h$  in the as-spun blend film suggests that the ordering of the P3HT chains is disturbed. The amorphous nature of the P3HT is also revealed from the structureless GSB spectra in Figure 3-6b. In turn, thermal annealing improves chain order, as revealed by the pronounced vibronic structures of the GSB spectra (Figure 3-6c). Furthermore, the increase in  $\mu_h$  at temperatures above 80 °C correlates to the growth of P3HT domains, resulting in the formation of interconnected P3HT crystalline phases. The author therefore concludes that the purification of PF12TBT-rich domains and ordering of P3HT chains proceed by thermal annealing, and that, at temperatures higher than 80 °C, domains coarsening is accelerated to form crystalline P3HT networks.

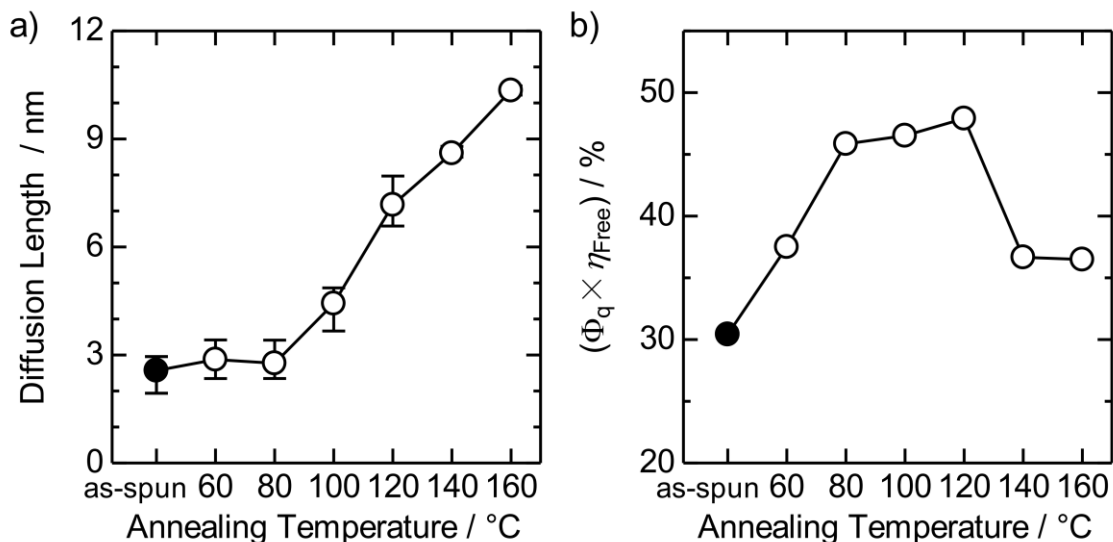


**Figure 3-11.** (a) Diffusion length for singlet exciton and (b) the product of  $\Phi_q$  and  $\eta_{\text{free}}$  in P3HT/PF12TBT blend films as a function of annealing temperature.

### 3.3.2. Influence of Morphology on Free Carrier Generation Efficiency

In general, the monomolecular decay of charges on a sub-nanosecond to several nanosecond timescale has been assigned to the geminate recombination of strongly bound interfacial radical pairs (charge-transfer state) and/or electron–hole pairs that are spatially confined by the physical size of their respective domains.<sup>30,31</sup> The generation of spatially confined charge pairs is considered to be formed from charge transfer at the interface of intimately mixed donor and acceptor polymer chains, or on isolated polymer chains inside another polymer domains. In other words, geminate recombination is not only inherent to the molecular electronic nature of a particular donor/acceptor interface but it also should be influenced by the blend morphologies.<sup>37,38</sup> As discussed above, thermal annealing increases ordering of P3HT chains and the purity of PF12TBT-rich domains. Moreover, it promotes the interconnection between P3HT crystalline phases and induces the growth of pure PF12TBT domains. As to the molecular electronic nature at the donor/acceptor domain interface, ordering of P3HT chains plays an important role to in circumventing

charge pair recombination, because it enables polarons to delocalize within  $\pi$ -stacking P3HT chains, and moreover, it increases local hole mobility. Both of them are considered to facilitate free carrier generation.<sup>38-40</sup> On the other hand, as listed in Table 3-1, a majority of charges are generated from the excitons that diffuse from the inside of domains to the preferred domain interface: for the blend film annealed at 160 °C, as much as 69% of overall charge generation process arises from the exciton diffusion, and 36% even in the as-spun blend film. Therefore domain purification is also critically important for suppressing undesired quenching of excitons by the isolated polymer chains on the way to the domain interface. The importance of domain purity is not limited to just P3HT/PF12TBT but rather common for polymer/polymer blends, which are more likely to phase-separate on a larger scale than that of the polymer/fullerene blends are.<sup>4,5,9</sup>

### 3.3.3. Relevance to Device Performance

Finally, the author discusses the correlation between  $\eta_{\text{free}}$  and the EQE. Among the generated charges, only free carriers can contribute to photocurrent. Therefore geminate recombination of charges reduce photocurrent and thus the EQE. In the as-spun blend film, the 64% of total generated charges decayed geminately with a characteristic inverse rate of 2500 ps. This dominant geminate recombination accounts for the poor EQE for the as-spun device, although a well-mixed blend morphology results in the high conversion yield of singlet excitons into charges. The degree of PL quenching provides information on the charge generation efficiency of the PF12TBT excitons. Therefore combining the  $\Phi_{\text{q}}$  and  $\eta_{\text{free}}$ , the author estimated the overall generation yield of free carriers in each blend film by the product of  $\Phi_{\text{q}}$  and  $\eta_{\text{free}}$ . Figure 3-11b shows the temperature dependence of  $\Phi_{\text{q}} \times \eta_{\text{free}}$ , which is in good agreement with the EQE values provided in Figure 3-2b. This suggests that the free carrier generation yield is one of the major factors that limits the value of EQEs

in this polymer/polymer blend system. The EQE increases with annealing temperature up to 80 °C, because  $\eta_{\text{free}}$  increases without suffering from a reduction in  $\Phi_{\text{q}}$ . Annealing at temperatures above 80 °C leads to the further increase in  $\eta_{\text{free}}$  but it reduces charge generation efficiency due to domain coarsening. Consequently, EQE is maximized at 80 – 120 °C, then decreases above that point. For P3HT/PF12TBT BHJ solar cells, thermal annealing of the blend film without domain coarsening is required to achieve larger EQE values.

These results on the basis of TA measurements revealed that  $\eta_{\text{free}}$  approaches 74% for the blend film annealed at 160 °C. This finding indicates that efficient free carrier generation is not restricted to the polymer/fullerene domain interface but can be obtained at polymer/polymer domain interface, which is also supported by the large EQEs exceeding 50% achieved in the state-of-the-art polymer/polymer solar cells.<sup>41–43</sup> In addition, efficient free carrier generation in the blend films composed of crystalline P3HT and amorphous PF12TBT suggests that crystalline acceptor polymers are not necessarily required for free carriers generation. This result offers the new design guide for combinations of donor/acceptor polymers toward the development of polymer/polymer blend solar cells.

### 3.4. Conclusions

The author has found that charge generation and recombination dynamics are significantly affected by thermal annealing. Singlet excitons are efficiently converted into charges in the as-spun blend film because P3HT and PF12TBT are sufficiently mixed with each other on the length scale shorter than their exciton diffusion lengths. This mixing of the polymer phases and the disordered nature of the P3HT chains primarily resulted in monomolecular recombination. However, thermal annealing promotes demixing of the polymers, forming relatively pure domains and ordering of the P3HT chains. As a result, monomolecular recombination loss is suppressed with increasing temperature, while  $\eta_{\text{free}}$

increases. However, thermal annealing also causes domain coarsening, decreasing the donor/acceptor domain interface area and thus reducing charge generation efficiency. The good correlation between the temperature dependence of  $\Phi_q \times \eta_{\text{free}}$  and EQE reveals that the overall yield of free carrier generation from singlet excitons is one of the major factors that limits EQE, even when  $\eta_{\text{free}}$  itself is improved. The P3HT/PF12TBT domain interface possesses a potential for efficient free carrier generation. Suppressing domain coarsening during thermal annealing is key to improving EQEs and the overall photovoltaic performance.

### 3.5. Experimental

*Materials:* PF12TBT was synthesized and characterized by Sumitomo Chemical Co., Ltd. The weight-average molecular weight  $M_w$ , polydispersity index (PDI, given by  $M_w/M_n$ , where  $M_n$  is the number-average molecular weight), and glass transition temperature  $T_g$  of PF12TBT are  $M_w = 20,000 \text{ g mol}^{-1}$ , PDI = 2.0, and  $T_g = 76 \text{ }^\circ\text{C}$ , respectively. P3HT was purchased from Aldrich Chemical Co. (Lot MKBD3325). The head-to-tail regioregularity,  $M_w$ , and PDI provided on the Certificate of Analysis were 90.0%, 42,300  $\text{g mol}^{-1}$ , and 1.9, respectively. Poly(3,4-ethylenedioxythiophene) polystyrene sulfonate (PEDOT:PSS) was purchased from H.C. Starck PH-500.

*Film Fabrication Method:* Sapphire substrates were washed by ultrasonication with toluene, then acetone, and finally ethanol for 15 min each and then dried under an  $\text{N}_2$  flow. The washed substrates were further treated with a UV- $\text{O}_3$  cleaner (Nippon Laser & Electronics Lab., NL-UV253S) for 30 min. P3HT and PF12TBT neat films were spin-coated onto cleaned sapphire substrates from chloroform (CF) solution with the solution concentration of 16  $\text{mg mL}^{-1}$  for P3HT and 18  $\text{mg mL}^{-1}$  for PF12TBT. P3HT/PF12TBT blend films were spin-coated from CF solution with a total solution concentration of 18  $\text{mg mL}^{-1}$ , and then

annealed at the different temperature ranging from 60 to 200 °C for 10 min in an N<sub>2</sub>-filled glove box. The spinning rate were kept at 3000 rpm (rotations per minute) for all films.

*Device Fabrication Method and Characterization:* Indium–tin–oxide (ITO)-coated glass substrates (10 Ω per square) were cleaned, and then a 40-nm-thick topcoat layer of PEDOT:PSS was spin-coated onto the ITO substrate as described above. A blend layer of P3HT/PF12TBT was spin-coated onto the PEDOT:PSS film at 3000 rpm for 60 s from CF solutions. The blend solution was prepared by mixing P3HT and PF12TBT with a weight ratio of 1:1 in CF: P3HT (6.5 mg) and PF12TBT (6.5 mg) were dissolved in 1 mL of CF. The thickness of the P3HT/PF12TBT blend layers was approximately 65 nm. After film deposition, thermal annealing was conducted at the different temperature ranging from 60 to 200 °C for 10 min in an N<sub>2</sub>-filled glove box. Finally, a calcium interlayer (Ca, 10 nm) and an aluminum electrode (Al, 70 nm) were vacuum-deposited through a shadow mask at  $2.5 \times 10^{-4}$  Pa. The active area of the device was 0.07 cm<sup>2</sup>, which was determined from the area of the top Ca/Al electrode. The EQE spectra were measured by using an ECT-250D integrated system made by Bunko-Keiki Co. under the illumination of monochromatic light from a 300-W xenon lamp with optical cut filters and a double monochromator. The power of the incident monochromatic light was kept under 0.05 mW cm<sup>-2</sup>, as measured by a calibrated silicon reference cell.

*Photoluminescence Quenching Measurements:* The photoluminescence (PL) spectra were measured for a neat PF12TBT film and P3HT/PF12TBT blend films spin-coated on a glass substrate by using a calibrated fluorescence spectrophotometer (Hitachi, F-4500). Excitation was performed at 392 nm to excite a PF12TBT component mainly (excitation fraction of each component was 75% (PF12TBT) and 25% (P3HT)) and at an incident angle of 30° normal to the substrate. Emission was collected normal to the excitation light. The PL quenching efficiency of PF12TBT in the blend film was evaluated from the ratio of the

PL intensity for the P3HT/PF12TBT blend films to that for a neat PF12TBT film after each PL intensity was corrected by variations for PF12TBT absorption at 392 nm.

*Fabrication Method of Single Carrier Device and Mobility Measurement:* Single carrier devices for charge carrier mobility measurements were fabricated as follows: for hole-only devices a P3HT/PF12TBT blend layer was spin-coated on separate ITO substrates covered with 40-nm-thick PEDOT:PSS, which acted as the anode. After spin-coating blend films were annealed at various temperatures in an N<sub>2</sub>-filled glove box. A gold electrode (Au, 50 nm) was then vacuum-deposited on each layer as the cathode (ITO|PEDOT:PSS|P3HT/PF12TBT|Au). Thickness of a P3HT/PF12TBT blend layer was approximately 90 nm. For electron-only devices a 50-nm-thick Al layer, which acted as the anode, was vacuum-deposited on a glass substrate covered with 20-nm-thick poly(sodium 4-styrenesulfonate) ( $M_w = 70,000 \text{ g mol}^{-1}$ ). A P3HT/PF12TBT blend layer was spin-coated onto each Al electrode and then annealed at various temperatures in an N<sub>2</sub>-filled glove box. A Ca interlayer (10 nm) and an Al (70 nm) layer were then vacuum-deposited as the cathode (Al|P3HT/PF12TBT|Ca|Al). Thickness of the P3HT/PF12TBT blend layer was approximately 80 nm. The Ca layer was used to enhance the efficiency of electron injection. The dark  $J$ - $V$  characteristics of the devices were measured under an N<sub>2</sub> atmosphere by using a direct-current voltage and a current source/monitor (Advantest, R6243). The P3HT/PF12TBT blend layer was spin-coated under the same conditions used for the device fabrication.

*Transient Absorption Measurements:* Transient absorption data were collected using a femtosecond pump and probe transient absorption spectroscopy system. The pump and probe femtosecond transient absorption spectroscopy system consists of a transient absorption spectrometer (Ultrafast Systems, Helios) and a regenerative amplified Ti:sapphire laser (Spectra-Physics, Hurricane). The amplified Ti:sapphire laser provided

800-nm fundamental pulses at a repetition rate of 1 kHz, with an energy of 0.8 mJ, and with a pulse width of 100 fs (FWHM); the pulses were split into two optical beams with a beam splitter to generate pump and probe pulses. One fundamental beam was converted into pump pulses at 400 nm with a second harmonic generator (Spectra-Physics, TP-F). The other fundamental beam was converted into white light continuum pulses for use as probe pulses in the wavelength region from 400 to 1500 nm. The pump pulses were modulated mechanically at a repetition rate of 500 Hz. The temporal evolution of the probe intensity was recorded with a Si CCD-array photodetector (Ocean Optics, S2000) for the visible measurement and with an InGaAs digital line scan camera (Sensors Unlimited, SU-LDV) for the near-IR measurement. The excitation fluence was varied from 7.5 to 1.5  $\mu\text{J cm}^{-2}$ , as measured by a calibrated photodiode (OPHIR, PD300-UV) connected to an energy meter (OPHIR, Nova). TA spectra were obtained over a time range of  $-5$  ps to 8 ns. Typically, 2500–5000 laser shots were averaged on each delay time to obtain a detectable absorbance change as small as  $10^{-5}$ – $10^{-3}$  depending on the monitor wavelength range and the excitation fluence. In order to cancel out orientation effects on the dynamics, the polarization direction of the linearly polarized probes pulse was set at a magic angle of  $54.7^\circ$  with respect to that of the pump pulse. The sample films were sealed in an  $\text{N}_2$ -filled quartz cuvette. The nanosecond transient absorption data were collected with a pump-probe transient absorption system (Ultrafast System, EOS). The excitation source was used the same as that was employed in the femtosecond system. The probe pulse (0.5 ns pulse width, 20 kHz repetition rate) was generated by focusing a Nd:YAG laser pulse into a photonic crystal fiber. The probe pulses were synchronized with the femtosecond amplifier, and the delay time was controlled by a digital delay generator electrically (CNT-90, Pendulum Instruments). The excitation fluence was varied from 60 to 3.8  $\mu\text{J cm}^{-2}$ ,

### 3.6. Appendix

#### 3.6.1. TA Dynamics from Singlet Exciton and SE in a PF12TBT Neat Film

To confirm the assignment of the TA spectra of PF12TBT singlet excitons, the author compared the dynamics of singlet excitons monitored at 1200 nm with that of the SE recorded at 650 nm. Figure 3-A1 shows the TA dynamic tracked at the wavelengths of 1200 nm and 650 nm. These two dynamics coincide with each other. The author therefore attributes the broad absorption band observed in the wavelength region of 800 – 1500 nm to the absorption of PF12TBT singlet excitons.

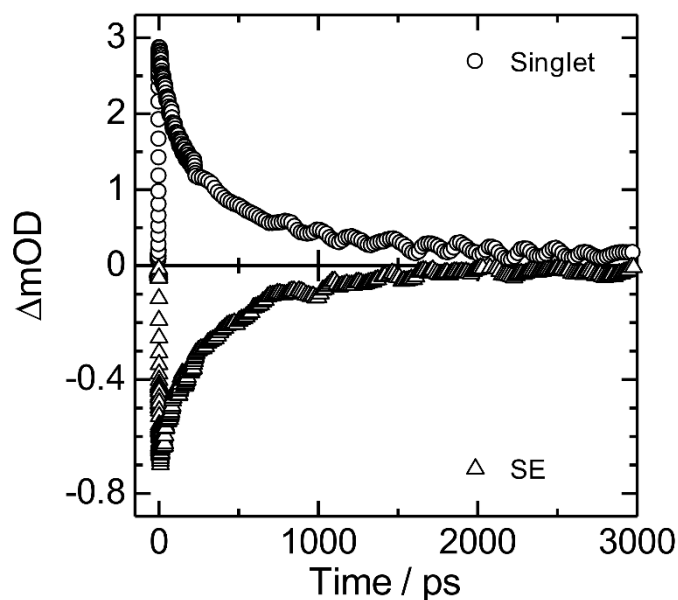


**Figure 3-A1.** TA signals from singlet excitons (circles) and SE (triangles) in a PF12TBT neat film recorded at 1200 nm and 650 nm, respectively. The excitation wavelength was 400 nm and the excitation fluence was  $7.5 \mu\text{J cm}^{-2}$ .

### 3.6.2. TA Spectra of a PF12TBT Neat Film

To address the origin of the spectral change observed in Figure 3-4b, the author measured the TA spectra of PF12TBT neat film by changing the excitation wavelength (energy). Figure 3-A2 shows the TA spectra of the PF12TBT neat film recorded by the 560 nm excitation. Little change in the spectral shape was observed compared to the spectra obtained by the 400 nm excitation as shown Figure 3-5b. In general, copolymers based on fluorene (F) and 4,7-dithiophene-2-yl-benzo[1,2,5]thiadiazole (TBT) units have two distinct absorption bands: a blue band below 450 nm attributed to a fully-delocalized excitonic  $\pi-\pi^*$  transition, a red band around 580 nm ascribed to a localized charge transfer state with the excited electron confined to the TBT unit.<sup>25</sup> In the case of the 560 nm excitation, singlet excitons are generated at the charge transfer state immediately after the excitation. The author therefore attributes the spectral change within 10 ps after excitation observed by the 400 nm excitation (Figure 3-4b) to the relaxation of singlet excitons from the higher energy excitonic state to the lower energy charge transfer state.

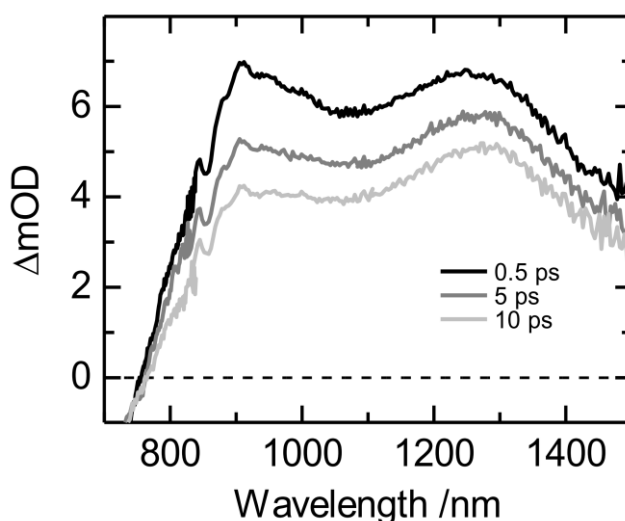


**Figure 3-A2.** TA spectra of a PF12TBT neat film excited at the wavelength of 560 nm at delay times of 0.5 ps, 5 ps, and 10 ps. The excitation fluence was  $10 \mu\text{J cm}^{-2}$ .

### 3.6.3. Assignment of Charge Induced Absorption

To confirm the assignment of the long-lived transient species, the author measured the TA spectra of the as-spun blend film in the microsecond time range. Figure 3-A3 shows the microsecond TA spectra and decays. The long-lived transient species observed at 3000 ps also exists in the microsecond time range with the similar spectral shape. Furthermore, the decay rate of the TA signal was not changed even under O<sub>2</sub> atmosphere. The author therefore concludes that the long-lived species observed in the blend films is the polarons of P3HT and PF12TBT.

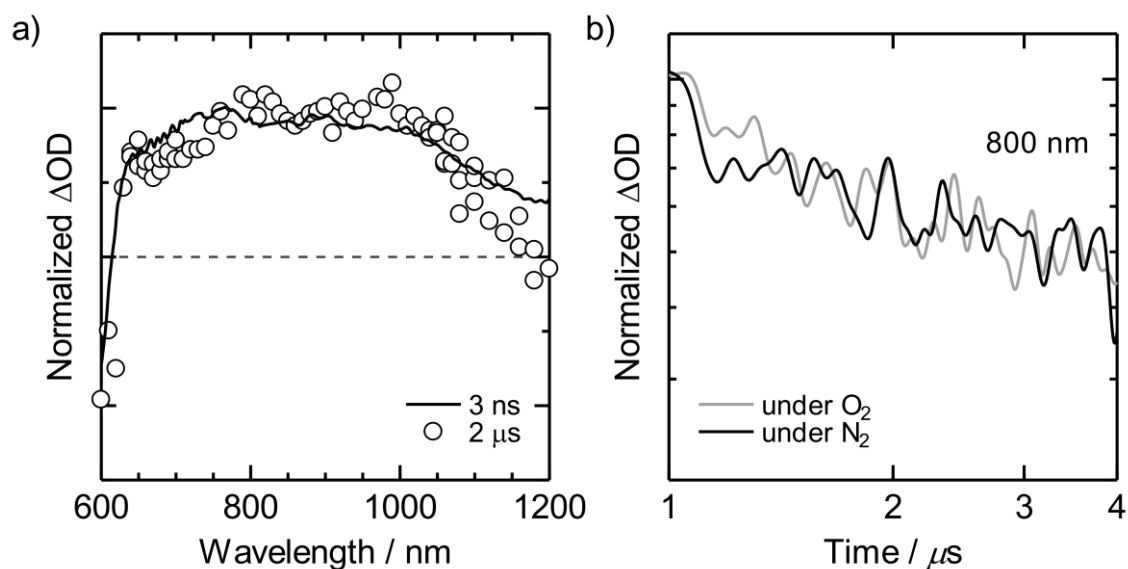


**Figure 3-A3.** (a) Normalized TA spectra of the as-spun blend film measured at delay times of 3 ns (solid line) and 2  $\mu s$  (open circles). (b) TA decay signals recorded at 800 nm under N<sub>2</sub> (blue line) and O<sub>2</sub> (red line) atmosphere. The excitation wavelength was 400 nm and the excitation fluence of microsecond TA measurements was 20  $\mu J cm^{-2}$ .

### 3.6.4. Estimation of Molar Absorption Coefficient of Charge Induced Absorption

To estimate molar absorption coefficient ( $\epsilon$ ) of the charge induced absorption observed in P3HT/PF12TBT blend films, the author first estimated the spectral shape of PF12TBT anion. The absorption spectra of PF12TBT anion was obtained by spectroelectrochemical measurements of a PF12TBT neat film coated on a conductive substrate. On the other hand, the TA spectra of P3HT cation polarons have been reported by Guo *et al.*<sup>24,A1</sup> They found two types of P3HT cation polarons: delocalized and localized polarons. The spectral shape of the charge induced absorption is constructed by summing these three absorption spectra, and then its molar absorption coefficient is estimated based on the molar absorption coefficient of the P3HT localized polaron reported in Reference A1.

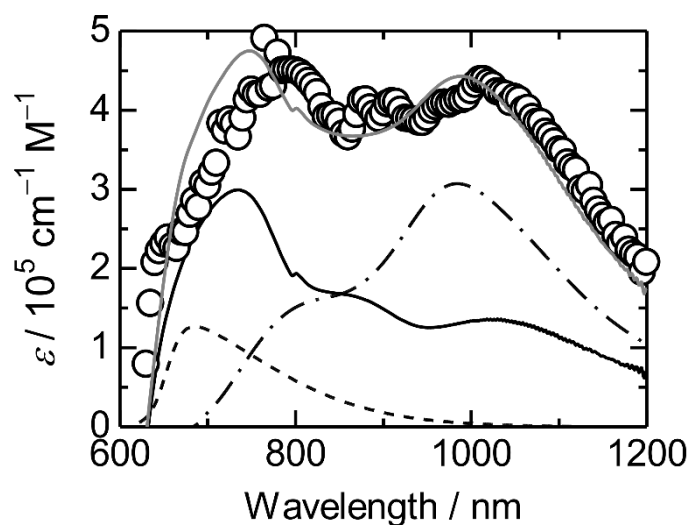


**Figure 3-A4.** Molar absorption coefficient ( $\epsilon$ ) of the charge induced absorption of a blend film (black circles). The gray solid line represents the absorption spectrum estimated by the sum of each absorption spectrum of charges: P3HT delocalized cation polaron (black dashed line), P3HT localized cation polaron (black dashed dotted line), and PF12TBT anion (black solid line).

### 3.6.5. Fluence Dependence of Charge Induced Absorption at Nanosecond Time Range

To investigate the dynamics of the charge induced absorption remained at the time range from sub-nanosecond to sub-microsecond, the author measured the fluence dependence of charge recombination dynamics in the 140 °C-annealed blend film. As shown in Figure 3-A5, the fluence-dependent charge recombination was observed: as the excitation intensity was higher, charge recombination became faster. The author therefore concludes that charges remained at this time range can be assigned to free charges and their recombination shows bimolecular kinetics.

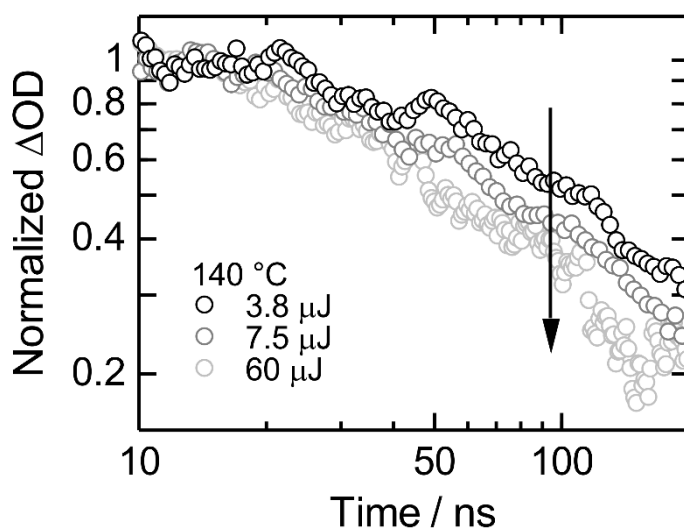


**Figure 3-A5.** Fluence dependence of charge recombination dynamics in the 140 °C-annealed blend film at the time range from sub-nanosecond to sub-microsecond monitored at 760 nm. The excitation wavelength was 400 nm and the excitation fluence was 3.8, 7.5, and 60  $\mu J cm^{-2}$ .

### 3.7. References and Note

- [1] R. Søndergaard, M. Hösel, D. Angmo, T. T. Larsen-Olsen, F. C. Krebs, *Mater. Today* **2012**, *15*, 36–49.
- [2] G. Dennler, M. C. Schaber, C. J. Brabec, *Adv. Mater.* **2009**, *21*, 1323–1338.
- [3] H. Ohkita, S. Ito, *Polymer* **2011**, *52*, 4397–4417.
- [4] C. R. McNeill, N. C. Greenham, *Adv. Mater.* **2009**, *21*, 3840–3850.
- [5] C. R. McNeill, *Energy Environ. Sci.* **2012**, *5*, 5653–5667.
- [6] A. Facchetti, *Mater. Today* **2013**, *16*, 123–132.
- [7] S. Liao, H. Jhuo, P. Yeh, Y. Cheng, Y. Li, Y. Lee, S. Sharma, S. Chen, *Sci. Rep.* **2014**, *4*, 6813.
- [8] Y. Liu, J. Zhao, Z. Li, C. Mu, W. Ma, H. Hu, K. Jiang, H. Lin, H. Ade, H. Yan, *Nat. Commun.* **2014**, *5*, 5293.
- [9] See Chapter 2.
- [10] See Chapter 4.
- [11] E. Zhou, J. Cong, Q. Wei, K. Tajima, C. Yang, K. Hashimoto, *Angew. Chem. Int. Ed.* **2011**, *50*, 2799–2803.
- [12] E. Zhou, J. Cong, K. Hashimoto, K. Tajima, *Adv. Mater.* **2013**, *25*, 6991–6996.
- [13] T. Earmme, Y. Hwang, N. M. Murari, S. Subramaniyan, S. A. Jenekhe, *J. Am. Chem. Soc.* **2013**, *135*, 14960–14963.
- [14] Y. Zhou, T. Kurosawa, W. Ma, Y. Guo, L. Fang, K. Vandewal, Y. Diao, C. Wang, Q. Yan, J. Reinspach, J. Mei, A. L. Appleton, G. I. Koleilat, Y. Gao, S. C. B. Mannsfeld, A. Salleo, H. Ade, D. Zhao, Z. Bao, *Adv. Mater.* **2014**, *26*, 3767–3772.
- [15] Z. Chen, Y. Zheng, H. Yan, A. Facchetti, *J. Am. Chem. Soc.* **2009**, *131*, 8–9.
- [16] C. R. McNeill, A. Abrusci, J. Zaumseil, R. Wilson, M. J. McKiernan, J. H. Burroughes, J. J. M. Halls, N. C. Greenham, R. H. Friend, *Appl. Phys. Lett.* **2007**, *90*,

- [17] C. R. McNeill, J. J. M. Halls, R. Wilson, G. L. Whiting, S. Berkebile, M. G. Ramsey, R. H. Friend, N. C. Greenham, *Adv. Funct. Mater.* **2008**, *18*, 2309–2321.
- [18] C. R. McNeill, A. Abrusci, I. Hwang, M. A. Ruderer, P. Müller-Buschbaum, N. C. Greenham, *Adv. Funct. Mater.* **2009**, *19*, 3103–3111.
- [19] C. R. McNeill, S. Westenhoff, C. Groves, R. H. Friend, N. C. Greenham, *J. Phys. Chem. C* **2007**, *111*, 19153–19160.
- [20] J. R. Moore, S. Albert-Seifried, A. Rao, S. Massip, B. Watts, D. J. Morgan, R. H. Friend, C. R. McNeill, H. Sirringhaus, *Adv. Energy Mater.* **2011**, *1*, 230–240.
- [21] M. Schubert, D. Dolfen, J. Frisch, S. Roland, R. Steyrlleuthner, B. Stiller, Z. Chen, U. Scherf, N. Koch, A. Facchetti, D. Neher, *Adv. Energy Mater.* **2012**, *2*, 369–380.
- [22] N. Zhou, H. Lin, S. J. Lou, X. Yu, P. Guo, E. F. Manley, S. Loser, P. Hartnett, H. Huang, M. R. Wasielewski, L. X. Chen, R. P. H. Chang, A. Facchetti, T. J. Marks, *Adv. Energy Mater.* **2014**, *4*, 1300785.
- [23] J. N. Hodgkiss, A. R. Campbell, R. A. Marsh, A. Rao, S. Albert-Seifried, R. H. Friend, *Phys. Rev. Lett.* **2010**, *104*, 177701.
- [24] The value was calculated from absorption coefficients of P3HT and PF12TBT.
- [25] J. Guo, H. Ohkita, H. Benten, S. Ito, *J. Am. Chem. Soc.* **2009**, *131*, 16869–16880.
- [26] J. Guo, H. Ohkita, H. Benten, S. Ito, *J. Am. Chem. Soc.* **2010**, *132*, 6154–6164.
- [27] K. G. Jespersen, W. J. D. Beenken, Y. Zaushitsyn, A. Yartsev, M. Andersson, T. Pullerits, *J. Chem. Phys.* **2004**, *121*, 12613.
- [28] P. J. Brown, H. Sirringhaus, M. Harrison, M. Shkunov, R. H. Friend, *Phys. Rev. B* **2001**, *63*, 125204.
- [29] J. Clark, C. Silva, R. H. Friend, F. C. Spano, *Phys. Rev. Lett.* **2007**, *98*, 206406.
- [30] I. A. Howard, R. Mauer, M. Meister, F. Laquai, *J. Am. Chem. Soc.* **2010**, *132*, 14866–

- 14876.
- [31] S. De, T. Pascher, M. Maiti, K. G. Jespersen, T. Kesti, F. Zhang, O. Inganäs, A. Yartsev, V. Sundström, *J. Am. Chem. Soc.* **2008**, *129*, 8466–8472.
- [32] O. V. Mikhnenko, H. Azimi, M. Schaber, M. Morana, P. W. M. Blom, M. A. Loi, *Energy Environ. Sci.* **2012**, *5*, 6960–6965.
- [33] Y. Wang, H. Benten, S. Ohara, D. Kawamura, H. Ohkita, S. Ito, *ACS Appl. Mater. Interfaces* **2014**, *6*, 14108–14115.
- [34] D. E. Markov, E. Amsterdam, P. W. M. Blom, A. B. Sieval, J. C. J. Hummelen, *J. Phys. Chem. A* **2005**, *109*, 5266–5274.
- [35] P. E. Shaw, A. Ruseckas, I. D. W. Samuel, *Adv. Mater.* **2008**, *20*, 3516–3520.
- [36] S. C. Veenstra, J. Loos, J. M. Kroon, *Prog. Photovolt: Res. Appl.* **2007**, *15*, 727–740.
- [37] T. W. Holcombe, J. E. Norton, J. Rivnay, C. H. Woo, L. Goris, C. Piliago, G. Griffini, A. Sellinger, J. Brédas, A. Salleo, J. M. J. Fréchet, *J. Am. Chem. Soc.* **2011**, *133*, 12106–12114.
- [38] D. Veldman, Ö. İpek, S. C. J. Meskers, J. Sweelssen, M. M. Koetse, S. C. Veenstra, J. M. Kroon, S. S. van Bavel, J. Loos, R. A. J. Janssen, *J. Am. Chem. Soc.* **2008**, *130*, 7721–7735.
- [39] C. Deibel, T. Strobel, V. Dyakonov, *Phys. Rev. Lett.* **2009**, *103*, 036402
- [40] F. C. Jamieson, E. B. Domingo, T. McCarthy-Ward, M. Heeney, N. Stingelin, J. R. Durrant, *Chem. Sci.* **2012**, *3*, 485–492.
- [41] See Chapter 5.
- [42] T. Earmme, Y. Hwang, S. Subramaniyan, S. A. Jenekhe, *Adv. Mater.* **2014**, *26*, 6080–6085.
- [43] See Chapter 6.
- [A1] J. Guo, H. Ohkita, H. Benten, S. Ito, *J. Am. Chem. Soc.* **2010**, *132*, 9631–9637.



## Chapter 4

### Influence of Molecular Weight of Acceptor Polymer on the Performance of Polymer/Polymer Blend Solar Cells

#### 4.1. Introduction

To develop all-polymer solar cells with a power conversion efficiency (PCE) comparable to that of polymer/fullerene solar cells,<sup>1-4</sup> it is necessary to understand and control the blend nanomorphology, and considerable efforts have been made to this end.<sup>5-11</sup> However, the PCEs of most all-polymer solar cells are still lower than 2.0%<sup>11-13</sup> because of the blend having undesirable morphological characteristics, such as large phase separation,<sup>14</sup> inhomogeneous internal phase composition,<sup>15-19</sup> and poor crystallinity.<sup>20</sup> Although there are several reports on the control of the phase-separated structures of polymer/polymer blends through the use of cosolvents<sup>13,21,22</sup> and through thermal annealing of the as-spun films,<sup>10,11</sup> it is still a challenge to obtain an optimal blend morphology that supports both efficient charge generation and charge transport at the same time.

In this chapter, the author fabricates polymer/polymer solar cells by blending poly(3-hexylthiophene) (P3HT, Figure 4-1), which is an electron donor, with poly[2,7-(9,9-didodecylfluorene)-*alt*-5,5-(4',7'-bis(2-thienyl)-2',1',3'-benzothiadiazole)] (PF12TBT, Figure 4-1), which is as an electron acceptor. The rate of phase separation during thermal annealing is strongly dependent on the molecular weight of PF12TBT, and a maximum PCE of 2.7% is achieved for the device based on high-molecular-weight PF12TBT, as shown in Figure 4-1. Therefore, the author concludes that molecular weight is a key factor that should be considered for improving the PCE of polymer/polymer solar cells.

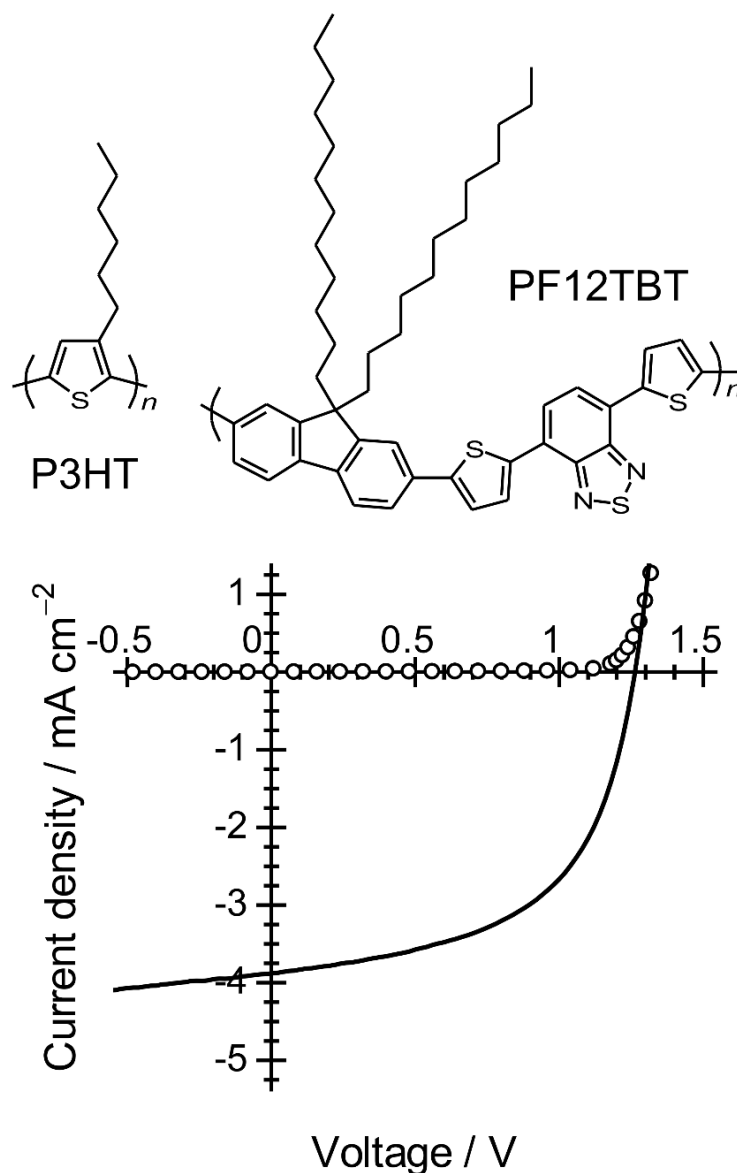


**Figure 4-1.** Chemical structures of P3HT and PF12TBT, and  $J$ - $V$  characteristics of a P3HT/PF12TBT solar cell with 2.7% PCE under AM 1.5G illumination from a calibrated solar simulator with an intensity of  $100 \text{ mW cm}^{-2}$  (solid line) and the dark condition (open circles). The molecular weight of PF12TBT was  $M_w = 78,000 \text{ g mol}^{-1}$ . The device was fabricated by spin-coating a CF solution of P3HT and PF12TBT (1:1 weight ratio) and annealed at  $140 \text{ }^\circ\text{C}$  for 10 min. The device parameters are listed in Table 4-2.

## 4.2. Results and Discussion

P3HT/PF12TBT solar cells were fabricated by using PF12TBT with three different molecular weights; the weight-average molecular weights ( $M_w$ ) are listed in Table 4-1. The best performance of each device is shown in Table 4-2. All the devices were fabricated by spin-coating chloroform (CF) solutions. With an increase in  $M_w$ , the PCE improved from 1.9% ( $M_w = 8,500 \text{ g mol}^{-1}$ ) to 2.0% ( $M_w = 20,000 \text{ g mol}^{-1}$ ) and 2.7% ( $M_w = 78,000 \text{ g mol}^{-1}$ ), which is one of the highest value reported so far for an all-polymer solar cell. Thus, it is clear that  $M_w$  has a significant impact on the solar cell efficiency. As evident from Table 4-2, the improvement in the PCE can be mainly ascribed to an increase in the fill factor (FF) since both short-circuit current density ( $J_{SC}$ ) and open-circuit voltage ( $V_{OC}$ ) were almost identical irrespective of  $M_w$ . Furthermore, the optimal annealing temperature increased from 100 to 140 °C with an increase in  $M_w$ , suggesting that the rate of evolution of the blend morphology during annealing varied with  $M_w$ . The difference in the blend morphology is confirmed by atomic force microscopy (AFM) images of the blend films before and after thermal annealing at 140 °C for 10 min. For the P3HT/*L*-PF12TBT, as shown in Figures 4-2a and 4-2b, surface roughness was increased from 4 nm to larger than 8 nm and coarsening of the morphology was observed after annealing. For the P3HT/*H*-PF12TBT,

**Table 4-1.** Weight-average molecular weight  $M_w$ , number-average molecular weight  $M_n$ , polydispersity index (PDI), and glass transition temperature ( $T_g$ ) of PF12TBT acceptor polymers used in this study.

Acceptor	$M_w / \text{g mol}^{-1}$	$M_n / \text{g mol}^{-1}$	PDI	$T_g / \text{°C}$
<i>L</i> -PF12TBT	8,500	4,900	1.7	60
<i>M</i> -PF12TBT	20,000	10,200	2.0	76
<i>H</i> -PF12TBT	78,000	28,000	2.8	90

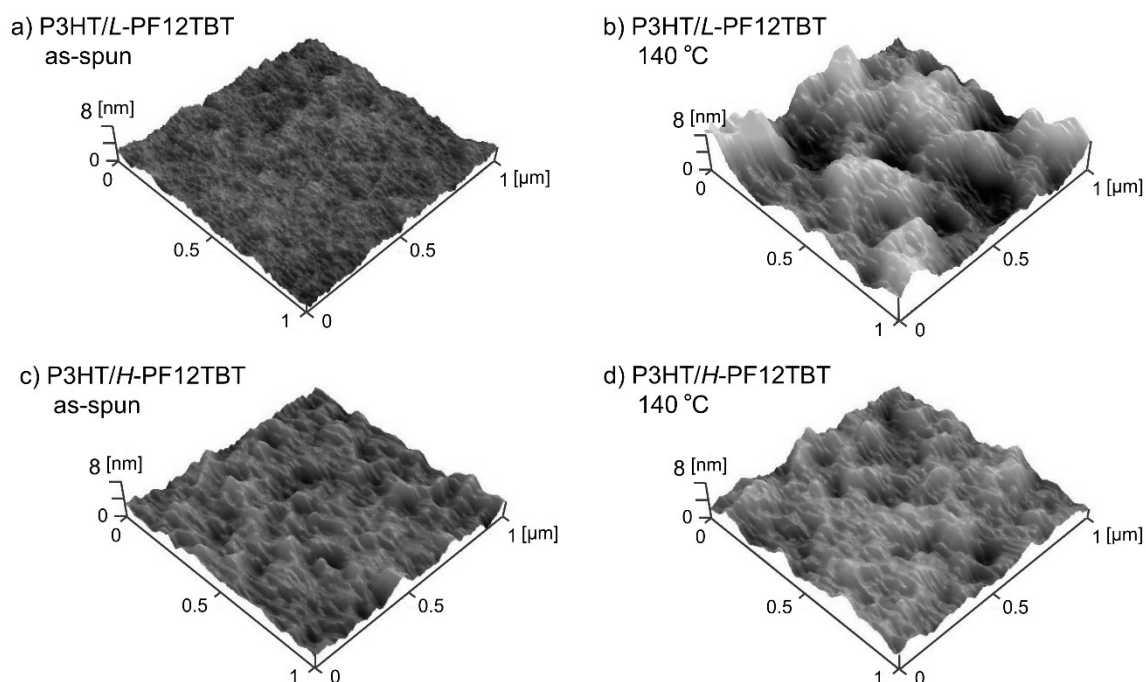


**Figure 4-2.** Tapping-mode AFM topographic images ( $1 \mu\text{m} \times 1 \mu\text{m}$ ) of (a and b) P3HT/L-PF12TBT and (c and d) P3HT/H-PF12TBT blend films spin-coated from CF solutions of P3HT and PF12TBT (1:1 weight ratio) on glass substrates: (a and c) as-spun films; (b and d) annealed films at  $140 \text{ }^\circ\text{C}$  for 10 min.

**Table 4-2.** Best PCE and device parameters of P3HT/PF12TBT solar cells measured under AM 1.5G simulated solar light irradiation (intensity:  $100 \text{ mW cm}^{-2}$ ).

Acceptor	$J_{\text{SC}} / \text{mA cm}^{-2}$	FF	$V_{\text{OC}} / \text{V}$	PCE / % <sup>a</sup>	Annealing Temperature / $^\circ\text{C}$ <sup>b</sup>
L-PF12TBT	3.80	0.41	1.22	1.90	100
M-PF12TBT	3.30	0.50	1.24	2.04	120
H-PF12TBT	3.88	0.55	1.26	2.70	140

<sup>a</sup> At least five devices were fabricated. The average values were 1.85% for L-PF12TBT, 1.93% for M-PF12TBT, and 2.61% for H-PF12TBT. <sup>b</sup> The annealing temperature corresponding to the highest PCE for each device.

as shown in Figures 4-2c and 4-2d, no distinct change in the surface morphology was observed before and after annealing. The different morphological evolution is resulted from the difference in the chain mobility of polymers; it is high for the blend with *L*-PF12TBT and low for *H*-PF12TBT.

First, the author focuses on the temperature dependence of the photoluminescence quenching efficiency of PF12TBT ( $\Phi_q$ ) and  $J_{SC}$  to discuss the nanoscale phase-separated morphology of PF12TBT in the blends. Before thermal annealing, as shown in Figure 4-3a, the  $\Phi_q$  values were in the range 80–90%, irrespective of  $M_w$ , suggesting that all the as-spun blends had well-mixed structures on a nanometer scale. After thermal annealing,  $\Phi_q$  decreased above a certain annealing temperature that depended on  $M_w$ : 80 °C for P3HT/*L*-PF12TBT, 100 °C for P3HT/*M*-PF12TBT, and 120 °C for P3HT/*H*-PF12TBT. On the other hand, as shown in Figure 4-3b, the maximum  $J_{SC}$  was obtained at 80 °C for P3HT/*L*-PF12TBT, 100 °C for P3HT/*M*-PF12TBT, and 120 °C for P3HT/*H*-PF12TBT. These results indicate that  $J_{SC}$  increased at the annealing temperatures at which  $\Phi_q$  was constant and it decreased over the temperature range where  $\Phi_q$  decreased. As discussed in Chapter 2, the  $\Phi_q$  value provides information about the purity and size of the PF12TBT-rich domains. The high  $\Phi_q$  (close to 90%) in the case of the P3HT/PF12TBT blends spin-coated from CF was related to nanometer-size domains containing P3HT as the minor constituent.<sup>11</sup> Thermal annealing should increase the domain purity or domain size. An increase in the domain purity results in an increase in  $J_{SC}$  because of the suppression of undesirable exciton quenching inside the domain. On the other hand, an increase in the domain size causes a decrease in the area of the domain interface necessary for charge generation. Thus, the  $\Phi_q$  value, which remained constant at 90% during the annealing, indicates that the domain size had a length scale smaller than that of exciton diffusion (about 10 nm), although purification proceeded in the domains. The subsequent decrease in  $\Phi_q$  at higher annealing temperatures

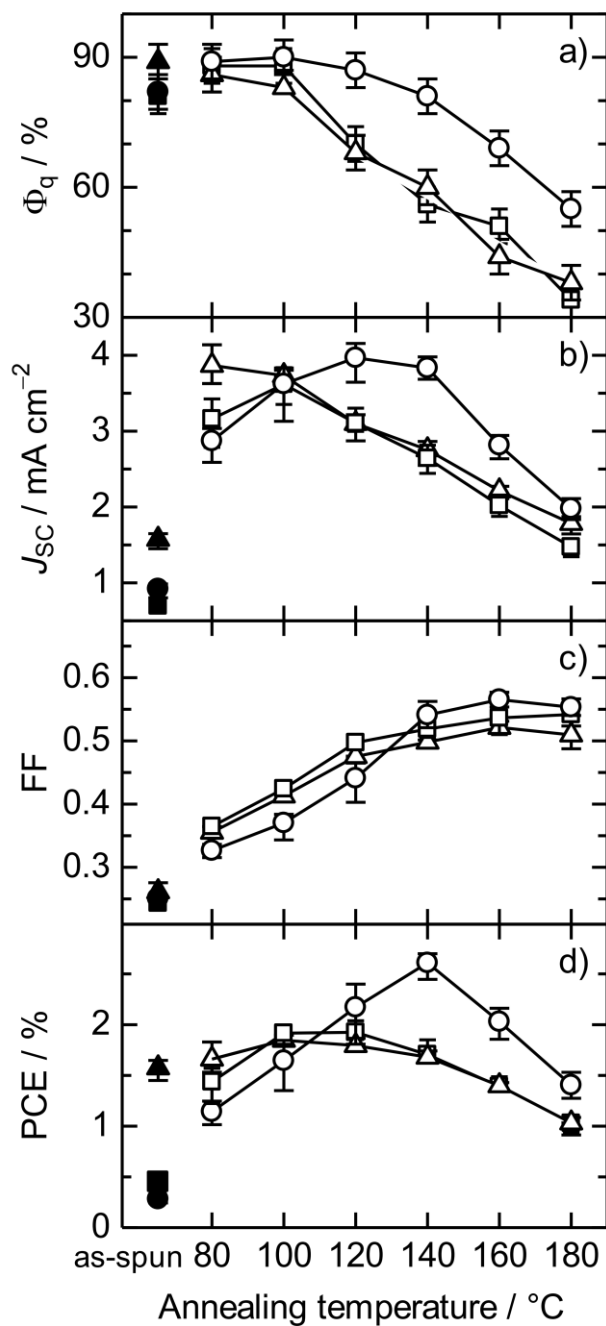


**Figure 4-3.** Dependence of  $\Phi_q$  and device parameters of the P3HT/L-PF12TBT (open triangles), P3HT/M-PF12TBT (open squares), and P3HT/H-PF12TBT (open circles) devices on the annealing temperature under AM 1.5G illumination from a calibrated solar simulator with an intensity of  $100 \text{ mW cm}^{-2}$ . The closed symbols represent  $\Phi_q$  and the device parameters for the as-spun devices. All devices were fabricated by spin-coating a CF solution of P3HT and PF12TBT (1:1 weight ratio) and annealed for 10 min.

suggests an increase in the domain size. Therefore,  $\Phi_q$  in Figure 4-3a shows that domain bloating was effectively suppressed in P3HT/*H*-PF12TBT until the blend was annealed at 140 °C, but it was accelerated in P3HT/*L*-PF12TBT even at low annealing temperatures. The slow domain bloating in P3HT/*H*-PF12TBT can be explained in terms of the high glass transition temperature of *H*-PF12TBT ( $T_g = 90$  °C, Table 4-1) and the reduced chain mobility of high-molecular-weight PF12TBT chains above  $T_g$ .<sup>5,23</sup> The author concludes that the rate of phase separation can be controlled by varying the  $M_w$  value of PF12TBT.

The author next focuses on the FF to discuss the molecular-weight dependence of the morphological evolution necessary for charge transport. As shown in Figure 4-3c, the FF increased from 0.25 for as-spun devices to 0.5 – 0.6 for the devices annealed at 160 °C, and it saturated at higher temperatures. The increase in the FF with temperature can be explained in terms of the purification of PF12TBT-rich domains and the formation of interconnected networks of the domains, since these factors contribute to efficient electron transport. For the P3HT/*L*-PF12TBT device, the FF increased with temperature because of the increase in the domain size. In contrast, for the P3HT/*H*-PF12TBT device annealed at high temperatures, the FF was as high as 0.5 – 0.6, although the large  $\Phi_q$  is indicative of well-mixed blend morphology. This finding suggests that the annealing of blends with high-molecular-weight PF12TBT is likely to result in the formation of interconnected networks without increasing the domain size. In addition to the PF12TBT morphology, the P3HT morphology should be considered in order to account for the increase in the FF with temperature. In blends consisting of P3HT and the fluorene-based copolymer poly[2,7-(9,9-dioctylfluorene)-*alt*-5,5-(4',7'-bis(4-hexyl-2-thienyl)-2',1',3'-benzothiadiazole)] (F8TBT), the hole mobility increased by nearly two orders of magnitude upon annealing at 180 °C, because of the ordering of the P3HT chains.<sup>20,24</sup> Indeed, the ordering of P3HT chains by annealing was found in this P3HT/PF12TBT blend from transient ground-state

bleaching (GSB) that were analyzed by transient absorption (TA) measurements. The TA measurements were performed for the as-spun and annealed P3HT/*H*-PF12TBT films at temperatures of 100, 120, and 140 °C. In Figure 4-4, transient GSB (a negative change in the optical density  $\Delta OD$ ) bands are observed at 3 ns, suggesting that holes and electrons were generated on P3HT and PF12TBT, respectively, because singlet excitons of both polymers had already decayed at 3 ns. The charge-induced GSB spectrum of the film annealed at 140 °C showed the most pronounced bleaching peaks at 550 and 600 nm, which are ascribed to the  $\pi$ -stacked P3HT chains.<sup>25-27</sup> The improved  $\pi$ -stacking in the P3HT-rich

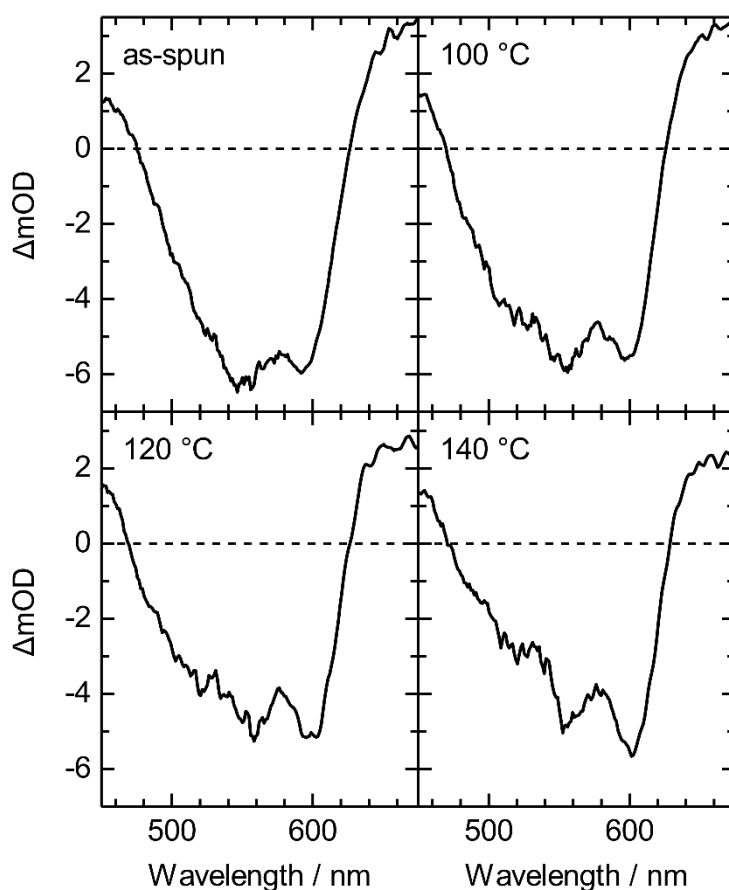


**Figure 4-4.** TA spectra for as-spun and annealed P3HT/*H*-PF12TBT blend films measured 3 ns after 400-nm photoexcitation with a 100-fs pulsed laser. The excitation fluence was  $45 \mu\text{J cm}^{-2}$  ( $9.1 \times 10^{13}$  photons  $\text{cm}^{-2}$ ) for all measurements.

phase should contribute to efficient hole transport<sup>28</sup> and thus to an increase in the FF. The author therefore concludes that both electron transport and hole transport are improved in P3HT/*H*-PF12TBT as a result of the excellent interconnectivity and thermal purification of the PF12TBT-rich phase and the ordering of P3HT chains; consequently, an increase in the FF is observed.

The author finally explains the molecular-weight dependence of the PCE in terms of the balance between  $J_{SC}$  and the FF. When P3HT/*L*-PF12TBT was annealed at 80 °C, the FF was still as low as 0.36; in other words, charge transport was poor because of the incomplete formation of interconnected networks of PF12TBT domains and the incomplete ordering of P3HT chains, although the maximum value of  $J_{SC}$  was achieved as a result of the purification of the PF12TBT domains. At annealing temperatures above 80 °C, the FF increased but  $J_{SC}$  decreased as a result of an increase in the domain size. Consequently, the device performance was determined by the balance between the decrease in  $J_{SC}$  and the increase in the FF. Thus, the P3HT/*L*-PF12TBT device showed the best PCE at 100 °C. This was also the case for the high-molecular-weight P3HT/*H*-PF12TBT device. However, efficient charge transport can be achieved through the purification of the interconnected PF12TBT phase and the ordering of P3HT chains in P3HT-rich domains at high annealing temperatures without drastically increasing the domain size. Due to the slow domain bloating,  $J_{SC}$  reached the maximum value at 120 °C and remained almost unchanged even at 140 °C. The author therefore concludes that the highest PCE of 2.7% can be achieved at 140 °C because the FF can be improved to up to 0.55 without decreasing the maximum value of  $J_{SC}$ .

### 4.3. Conclusions

The molecular-weight dependence of the PCE is attributed to the difference in the rate of phase separation during annealing. In the blend containing *H*-PF12TBT, the domain size of phase separation has a length scale comparable to that of exciton diffusion even at high annealing temperatures owing to the reduced diffusional mobility of the PF12TBT chains; such a domain size is necessary for efficient charge generation. Further, a blend morphology consisting of interconnected networks of pure PF12TBT domains and ordered P3HT chains, which is necessary for efficient charge transport, can be achieved by annealing. This blend morphology is responsible for the PCE of 2.7%, which is one of the highest ever reported for an all-polymer solar cell.

### 4.4. Experimental

*Materials:* PF12TBT samples with three different molecular weights were synthesized and characterized at Sumitomo Chemical Co., Ltd. The weight-average molecular weight  $M_w$ , polydispersity index (PDI, given by  $M_w/M_n$ , where  $M_n$  is the number-average molecular weight), and glass transition temperature  $T_g$  of each PF12TBT sample were as follows: *L*-PF12TBT,  $M_w = 8,500 \text{ g mol}^{-1}$ , PDI = 1.7, and  $T_g = 60 \text{ }^\circ\text{C}$ ; *M*-PF12TBT,  $M_w = 20,000 \text{ g mol}^{-1}$ , PDI = 2.0, and  $T_g = 76 \text{ }^\circ\text{C}$ ; *H*-PF12TBT,  $M_w = 78,000 \text{ g mol}^{-1}$ , PDI = 2.8, and  $T_g = 90 \text{ }^\circ\text{C}$ . P3HT was purchased from Aldrich Chemical Co. (Lot MKBD3325). The head-to-tail regioregularity,  $M_w$ , and PDI provided on the Certificate of Analysis were 90.0%, 42,300  $\text{g mol}^{-1}$ , and 1.9, respectively.

*Device Fabrication and Measurements:* Indium-tin-oxide (ITO)-coated glass substrates (10  $\Omega$  per square) were washed by ultrasonication in toluene, acetone, and ethanol for 15 min each in this order and then dried with  $\text{N}_2$  flow. The washed substrates were further treated with a UV- $\text{O}_3$  cleaner (Nippon Laser & Electronics Lab., NL-UV253S) for 30 min.

A thin layer (~40 nm) of poly(3,4-ethylenedioxythiophene):poly(4-styrenesulfonate) (PEDOT:PSS, H.C. Stark PH-500) was spin-coated onto the ITO substrate at a spin rate of 3000 rpm for 99 s and dried at 140 °C for 10 min in air. A blend layer of P3HT/PF12TBT was spin-coated on the PEDOT:PSS film at 3000 rpm for 60 s from CF solutions. All P3HT/PF12TBT blend films used in this study were spin-coated from CF solutions which were prepared by mixing P3HT and PF12TBT with a weight ratio of 1:1 as follows: three blend solutions were prepared by dissolving P3HT (6 mg) and *L*-PF12TBT (6 mg) in 1 mL of CF, P3HT (6 mg) and *M*-PF12TBT (6 mg) in 1 mL of CF, and P3HT (5.5 mg) and *H*-PF12TBT (5.5 mg) in 1 mL of CF, respectively. Thickness of the P3HT/PF12TBT blend layers was typically 60 nm. The photoactive layer was thermally annealed for 10 min in an N<sub>2</sub>-filled glove box, and then, a calcium interlayer (Ca, 15 nm) and an aluminum electrode (Al, 70 nm) were vacuum-deposited. The *J–V* characteristics of the devices were measured by using a direct-current voltage and a current source/monitor (Advantest model R6243) under illumination with AM1.5G simulated solar light with 100 mW cm<sup>-2</sup>. The light intensity was corrected with a calibrated silicon photodiode reference cell (Bunko-Keiki, BS-520). The active area of the device was 0.07 cm<sup>2</sup>. Illumination was carried out from the ITO side. All measurements were performed in N<sub>2</sub> atmosphere at room temperature. At least five devices were fabricated to ensure reproducibility of the *J–V* characteristics.

*AFM Measurements:* AFM images were collected in tapping mode (Shimadzu, SPM-9600) using silicon probes with a resonant frequency of ~330 kHz and a force constant of ~42 N m<sup>-1</sup> (Nanoworld, NCHR).

*Photoluminescence Quenching Measurements:* The photoluminescence (PL) spectra were measured for a PF12TBT neat film and P3HT/PF12TBT blend films spin-coated on a glass substrate by using a calibrated fluorescence spectrophotometer (Hitachi, F-4500). Excitation was performed at 392 nm to excite a PF12TBT component mainly (excitation

fraction of each component was 73% (PF12TBT) and 27% (P3HT)) and at an incident angle of 30° normal to the substrate. Emission was collected normal to the excitation light. The PL quenching efficiency of PF12TBT in the blend film was evaluated from the ratio of the PL intensity for the P3HT/PF12TBT blend films to that for a PF12TBT neat film after each PL intensity was corrected by variations for PF12TBT absorption at 392 nm.

*TA Measurements:* TA data were collected using a femtosecond pump-probe transient absorption spectroscopy system.<sup>29,30</sup> The pump and probe femtosecond transient absorption spectroscopy system consists of a transient absorption spectrometer (Ultrafast Systems, Helios) and a regenerative amplified Ti:sapphire laser (Spectra-Physics, Hurricane). The amplified Ti:sapphire laser provided 800-nm fundamental pulses at a repetition rate of 1 kHz, with an energy of 0.8 mJ, and with a pulse width of 100 fs (FWHM); the pulses were split into two optical beams with a beam splitter to generate pump and probe pulses. One fundamental beam was converted into pump pulses at 400 nm with a second harmonic generator (Spectra-Physics, TP-F). The other fundamental beam was converted into white light continuum pulses for use as probe pulses in the wavelength region from 400 to 800 nm. The pump pulses were modulated mechanically at a repetition rate of 500 Hz. The temporal evolution of the probe intensity was recorded with a Si CCD-array photodetector (Ocean Optics, S2000). Transient absorption spectra were obtained over the time range from -5 ps to 3 ns.

## 4.5. Appendix

### 4.5.1. Dark $J$ - $V$ Curve (Logarithmic Scale)

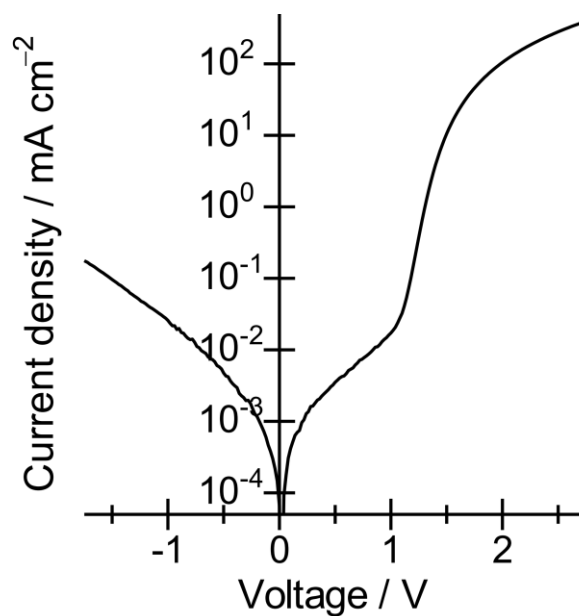


**Figure 4-A1.** Dark  $J$ - $V$  characteristic of a P3HT/PF12TBT solar cell with 2.7% PCE. The molecular weight of PF12TBT was  $M_w = 78,000 \text{ g mol}^{-1}$ . The device was fabricated by spin-coating a CF solution of P3HT and PF12TBT (1:1 weight ratio) and annealed at 140 °C for 10 min. The device parameters are listed in Table 4-2.

#### 4.5.2. Annealing-Temperature Dependence of $J-V$ Characteristics

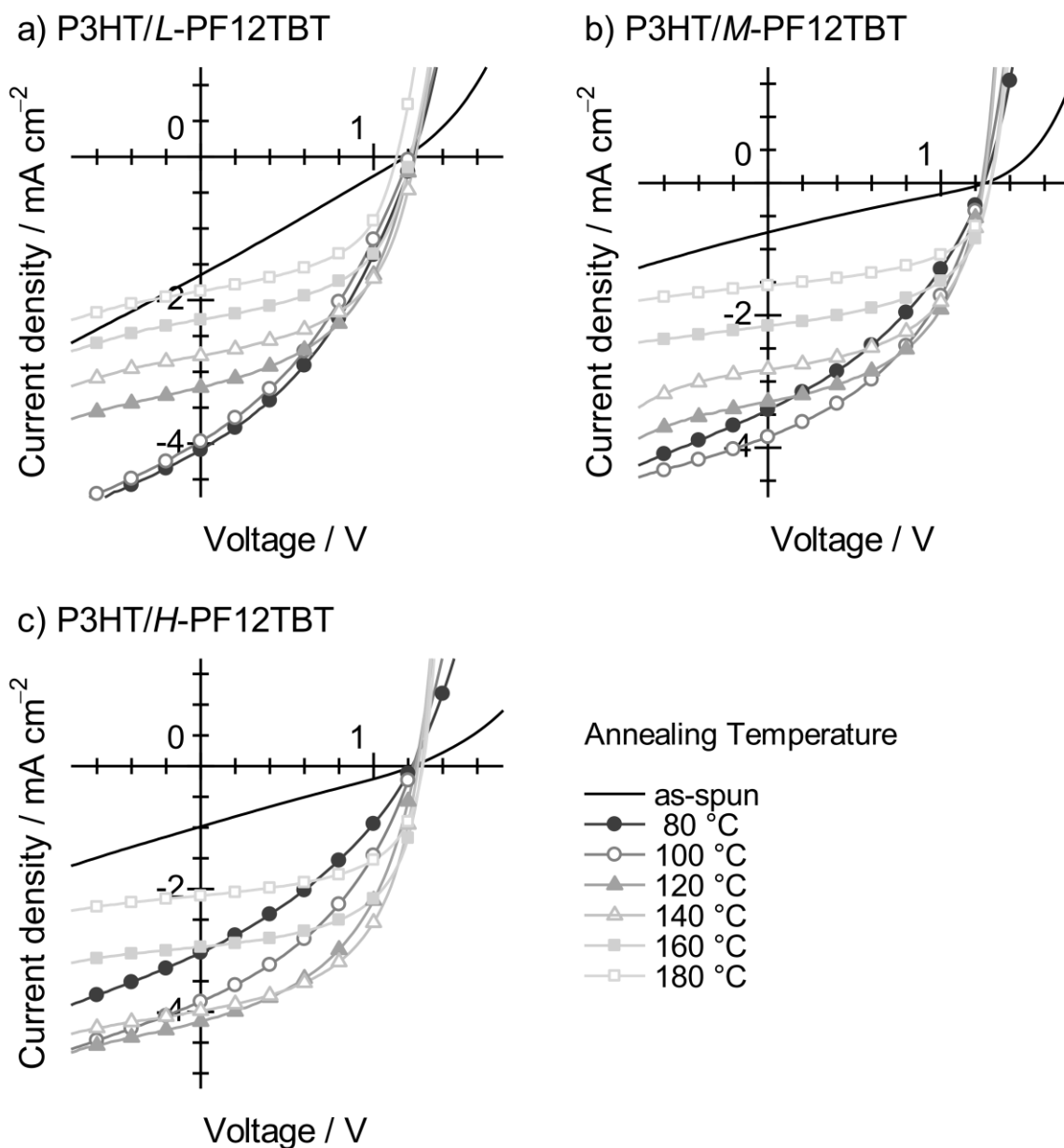


**Figure 4-A2.** Annealing-temperature dependence of  $J-V$  characteristics measured for (a) P3HT/L-PF12TBT, (b) P3HT/M-PF12TBT, and (c) P3HT/H-PF12TBT under AM 1.5G illumination from a calibrated solar simulator with an intensity of  $100 \text{ mW cm}^{-2}$ . The devices were fabricated by spin-coating a CF solution of P3HT and PF12TBT (1:1 weight ratio) and annealed for 10 min.

#### 4.6. References

- [1] J. Nelson, *Mater. Today* **2011**, *14*, 462–470.
- [2] H. Ohkita, S. Ito, *Polymer* **2011**, *52*, 4397–4417
- [3] G. Li, R. Zhu, Y. Yang, *Nat. Photon.* **2012**, *6*, 153–161
- [4] G. Dennler, M. C. Scharber, C. J. Brabec, *Adv. Mater.* **2009**, *21*, 1323–1338
- [5] S. C. Veenstra, J. Loos, J. M. Kroon, *Prog. Photovolt: Res. Appl.* **2007**, *15*, 727–740.
- [6] C. R. McNeill, N. C. Greenham, *Adv. Mater.* **2009**, *21*, 3840–3850.
- [7] H. Yan, B. A. Collins, E. Gann, C. Wang, H. Ade, C. R. McNeill, *ACS Nano* **2012**, *6*, 677–688.
- [8] X. He, F. Gao, G. Tu, D. Hasko, S. Hüttner, U. Steiner, N. C. Greenham, R. H. Friend, W. T. S. Huck, *Nano Lett.* **2010**, *10*, 1302–1307.
- [9] R. C. Mulherin, S. Jung, S. Huettner, K. Johnson, P. Kohn, M. Sommer, S. Allard, U. Scherf, N. C. Greenham, *Nano Lett.* **2011**, *11*, 4846–4851.
- [10] C. R. McNeill, S. Westenhoff, C. Groves, R. H. Friend, N. C. Greenham, *J. Phys. Chem. C* **2007**, *111*, 19153–19160.
- [11] See Chapter 2.
- [12] T. W. Holcombe, C. H. Woo, D. F. J. Kavulak, B. C. Thompson, J. M. J. Fréchet, *J. Am. Chem. Soc.* **2009**, *131*, 14160–14161.
- [13] E. Zhou, J. Cong, Q. Wei, K. Tajima, C. Yang, K. Hashimoto, *Angew. Chem. Int. Ed.* **2011**, *50*, 2799–2803.
- [14] C. Arias, J. D. MacKenzie, R. Stevenson, J. J. M. Halls, M. Inbasekaran, E. P. Woo, D. Richards, R. H. Friend, *Macromolecules* **2001**, *34*, 6005–6013.
- [15] H. J. Snaith, A. C. Arias, A. C. Morteani, C. Silva, R. H. Friend, *Nano Lett.* **2002**, *2*, 1353–1357.
- [16] R. Shikler, M. Chiesa, R. H. Friend, *Macromolecules* **2006**, *39*, 5393–5399.

- [17] C. R. McNeill, B. Watts, L. Thomsen W. J. Belcher, N. C. Greenham, P. C. Dastoor, H. Ade, *Macromolecules* **2009**, *42*, 3347–3352.
- [18] S. Swaraj, C. Wang, H. Yan, B. Watts, J. Lüning, C. R. McNeill, H. Ade, *Nano Lett.* **2010**, *10*, 2863–2869.
- [19] J. R. Moore, S. Albert-Seifried, A. Rao, S. Massip, B. Watts, D. J. Morgan, R. H. Friend, C. R. McNeill, H. Sirringhaus, *Adv. Energy Mater.* **2011**, *1*, 230–240.
- [20] C. R. McNeill, A. Abrusci, I. Hwang, M. A. Ruderer, P. Müller-Buschbaum, N. C. Greenham, *Adv. Funct. Mater.* **2009**, *19*, 3103–3111.
- [21] R. Campbell, J. M. Hodgkiss, S. Westenhoff, I. A. Howard, R. A. Marsh, C. R. McNeill, R. H. Friend, N. C. Greenham, *Nano Lett.* **2008**, *8*, 3942–3947.
- [22] M. Schubert, D. Dolfen, J. Frisch, S. Roland, R. Steyrlleuthner, B. Stiller, Z. Chen, U. Scherf, N. Koch, A. Facchetti, D. Neher, *Adv. Energy Mater.* **2012**, *2*, 369–380.
- [23] L. H. Sperling, In *Introduction to Physical Polymer Science*, 4th ed.; Wiley-Interscience: Hoboken, New Jersey, **2006**.
- [24] H. G. Flesch, R. Resel, C. R. McNeill, *Org. Electron.* **2009**, *10*, 1549–1555.
- [25] P. J. Brown, H. Sirringhaus M. Harrison, M. Shkunov, R. H. Friend, *Phys. Rev. B* **2001**, *63*, 125204.
- [26] J. Clark, C. Silva, R. H. Friend, F. C. Spano, *Phys. Rev. Lett.* **2007**, *98*, 206406.
- [27] J. Guo, H. Ohkita, H. Benten, S. Ito, *J. Am. Chem. Soc.* **2009**, *131*, 16869–16880
- [28] J. F. Chang, J. Clark, N. Zhao, H. Sirringhaus, D. W. Breiby, J. W. Andreasen, M. M. Nielsen, M. Giles, M. Heeney, I. McCulloch, *Phys. Rev. B* **2006**, *74*, 115318.
- [29] J. Guo, H. Ohkita, H. Benten, S. Ito, *J. Am. Chem. Soc.* **2009**, *131*, 16869–16880
- [30] S. Honda, S. Yokoya, H. Ohkita H. Benten, S. Ito, *J. Phys. Chem. C* **2011**, *115*, 11306–11317

## *Part II*



## Chapter 5

### Improvement in Light-Harvesting Efficiency by Using Low-Bandgap Donor and Acceptor Polymers

#### 5.1. Introduction

Conjugated polymer-based solar cells have gained increasing attention as a possible inexpensive source of renewable energy owing to their advantages such as high throughput and large-area production with low-cost printing processes.<sup>1</sup> The most studied polymer-based solar cells have a bulk-heterojunction (BHJ) active layer in which an electron donor polymer is mixed with an acceptor of low molecular weight fullerene derivative. The power-conversion efficiency (PCE) of the polymer/fullerene BHJ solar cells has steadily increased over the last ten years.<sup>2-5</sup> On the other hand, polymer/polymer BHJs consisting of a polymeric donor and acceptor have also been a subject of active research because of a number of potential advantages over conventional polymer/fullerene systems.<sup>6,7</sup> In particular, the flexible molecular design of both donor and acceptor polymers affords large scope for tuning the optical, electronic, and morphological properties of the materials. For instance, the blends of donor and acceptor polymers with high absorption coefficients in the visible and near-infrared ranges of wavelengths are able to harvest a large portion of sun light to yield a large photocurrent density  $J_{SC}$ . Further, the adjustment of the highest occupied molecular orbital (HOMO) and lowest unoccupied molecular orbital (LUMO) levels of the donor and acceptor polymers will allow the open-circuit voltage ( $V_{OC}$ ) to rise above 1 V. In addition, the phase-separated interpenetrating polymer morphologies will offer continuous pathways for charge-carrier transport, leading to a high fill factor (FF). However, despite these attractive features, the PCE of polymer/polymer BHJ solar cells

mostly remains at ~2%,<sup>8-10</sup> lagging far behind the efficiency of polymer/fullerene BHJ solar cells.<sup>11</sup>

Regioregular poly(3-hexylthiophene) (P3HT) is one of the most widely used donor polymers in the polymer/polymer BHJ solar cells because of its excellent hole mobility owing to the  $\pi$ - $\pi$  interchain stacking in crystals. However, the external quantum efficiencies (EQEs) reported for the P3HT/acceptor-polymer BHJ solar cells are below 30% regardless of the nature of the polymers used as acceptors.<sup>9,12-14</sup> These values are significantly different from the EQEs ranging from 70 to 80% shown by the P3HT/fullerene systems.<sup>4</sup> The poor PCEs of polymer/polymer BHJ solar cells reported so far are mainly attributed to the undesirable morphology of the blends such as large phase-separated domain sizes, inhomogeneous internal phase composition, and reduced crystallinity.<sup>6-9,12,14-17</sup> Therefore, some researchers attempt to control the nanoscale structure of phase separation by thermal annealing<sup>8,9</sup> and/or by using solvent additives<sup>13</sup> and donor-acceptor diblock copolymers.<sup>18</sup> In Chapter 4, a PCE of 2.7% has been achieved by using P3HT as a donor and a high molecular weight fluorene-based copolymer (PF12TBT) as an acceptor.<sup>8</sup> In this chapter, the author utilized poly[2,3-bis-(3-octyloxy-phenyl)quinoxaline-5,8-diyl-*alt*-thiophene-2,5-diyl] (PTQ1)<sup>19</sup> as a donor polymer in polymer/polymer BHJ solar cells (Figure 5-1a). As shown in Figure 5-1c, PTQ1 exhibited a longer absorption edge to up to ~700 nm and an intramolecular charge transfer absorption band centered at 630 nm, leading to more efficient light absorption at long wavelengths compared to P3HT. Moreover, PTQ1 films showed sufficient hole transport in the BHJ structures<sup>19</sup> even in the amorphous phase, which would eliminate the difficulties in controlling the crystallization. Poly{[*N,N'*-bis(2-octyldodecyl)-naphthalene-1,4,5,8-bis(dicarboximide)-2,6-diyl]-*alt*-5,5'-(2,2'-bithiophene)} [P(NDI2OD-T2); PolyeraActivInk™ N2200]<sup>20</sup> was used as the acceptor polymer owing to its high electron mobility, high electron affinity, and light absorption

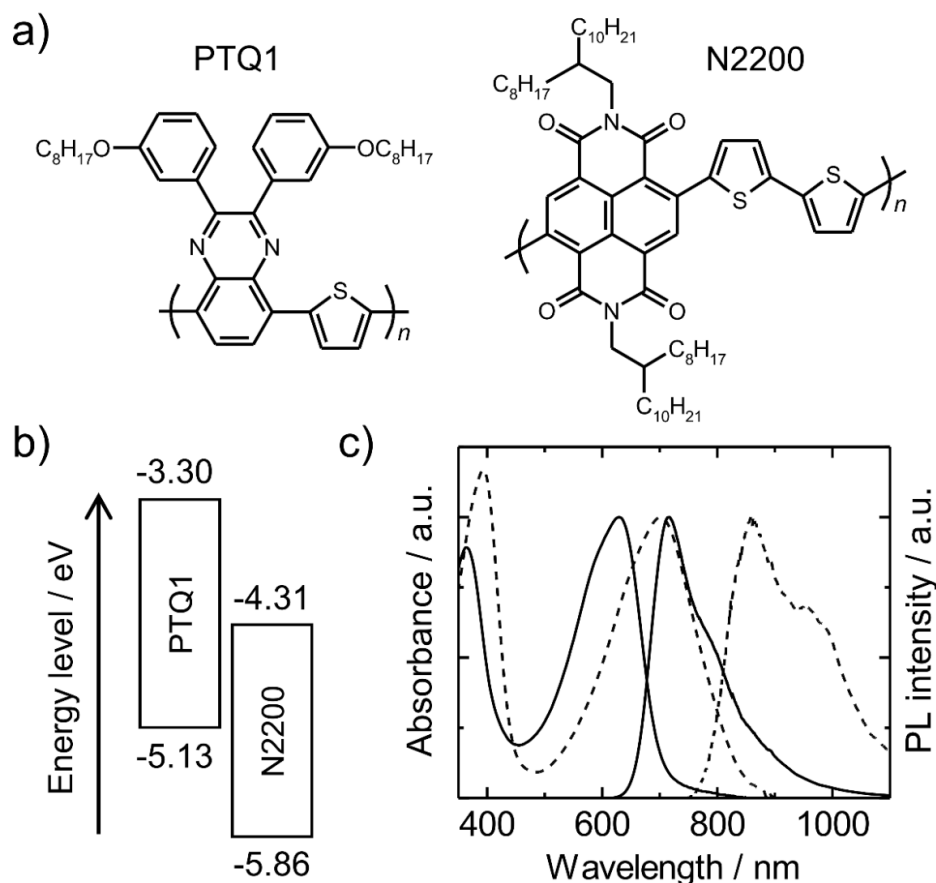


**Figure 5-1.** (a) Chemical structures of PTQ1 and N2200. (b) The energy level diagram of PTQ1 and N2200 neat films. The HOMO levels were determined by photoelectron yield spectroscopy and the LUMO levels were estimated by adding the optical energy gap calculated from the 0–0 transition to the HOMO energy.<sup>37</sup> (c) Normalized absorption (left) and photoluminescence (right) spectra of PTQ1 (solid lines) and N2200 (dashed lines) neat films.

ability at near-infrared wavelengths (Figures 5-1a and c). The absorption spectra of PTQ1 and N2200 blend covers the solar spectrum from visible light to 900 nm, and the LUMO–LUMO (1.0 eV) and HOMO–HOMO (0.7 eV) energy offsets are sufficient to cause charge generation (exciton dissociation) and subsequent free carrier generation at the heterojunction<sup>21</sup> (Figure 5-1b). In addition, the bulky phenyl side chains on PTQ1 could

facilitate free carrier generation because of the steric hindrance at the PTQ1/N2200 interface.<sup>22</sup>

## 5.2. Results and Discussion

A chloroform (CF) solution of the PTQ1/N2200 blend was prepared and spin-coated onto poly(3,4-ethylenedioxythiophene):poly(4-styrenesulfonate)-coated (PEDOT:PSS-coated) ITO substrates. The photoactive layers obtained were annealed at 120 °C for 10 min. The BHJ solar cells consisting of a 50:50 blend of PTQ1:N2200 resulted in a PCE as high as 3.4%. Figure 5-2 shows the atomic force microscopy (AFM) topographical and phase images ( $1 \mu\text{m} \times 1 \mu\text{m}$ ) of the PTQ1/N2200 blended film: no distinct phase-separated structures were observed. These featureless surface morphologies are typical of efficient polymer/polymer BHJ solar cells because of mixing of the donor and acceptor polymers on the nanometer scale.<sup>8,9</sup> The blending ratio of PTQ1 to N2200 was changed from 20 to 80

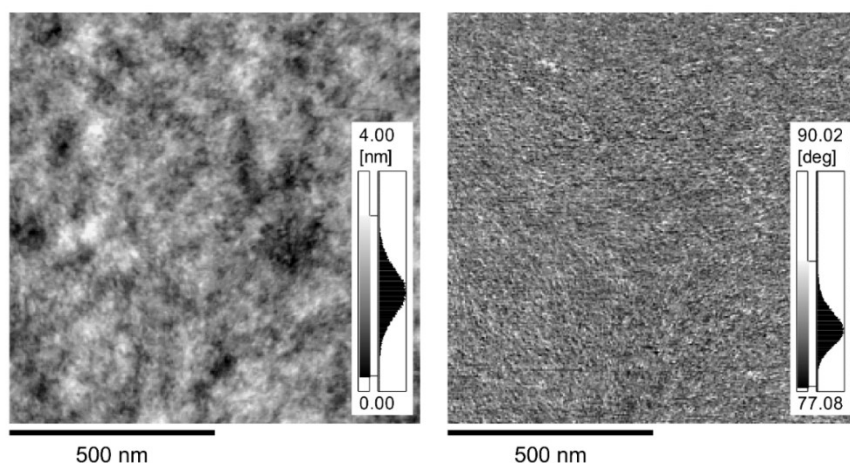


**Figure 5-2.** Tapping-mode AFM topographical (left) and phase (right) images ( $1 \mu\text{m} \times 1 \mu\text{m}$ ) of a PTQ1/N2200 blended film (weight ratio PTQ1:N2200 = 50:50). The scale bar corresponds to a length of  $0.5 \mu\text{m}$ . The film was spin-coated from a CF solution onto a glass substrate and annealed at 120 °C for 10 min.

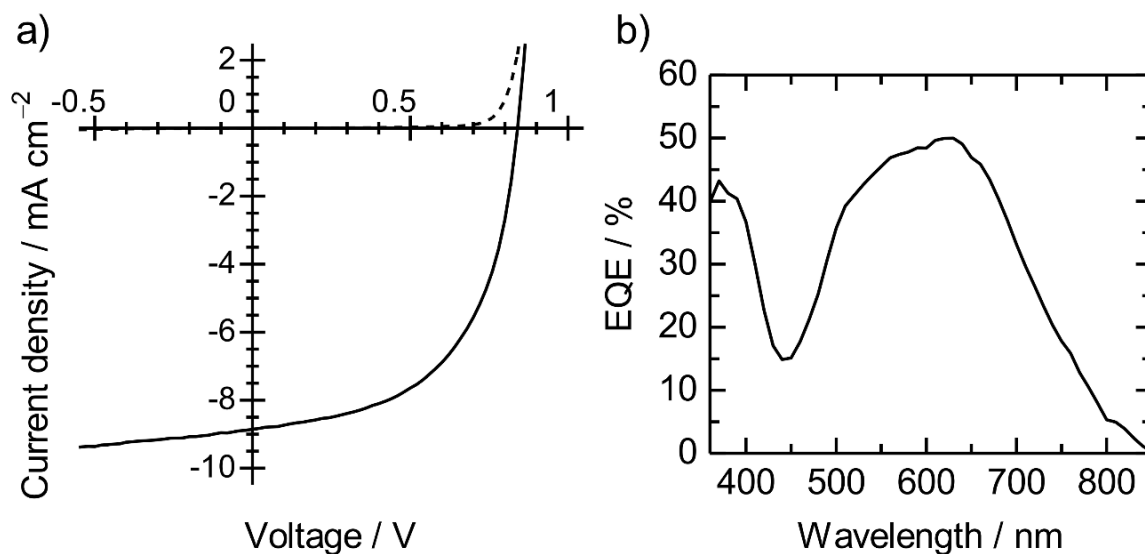


**Figure 5-3.** (a)  $J$ - $V$  characteristics of a PTQ1/N2200 (weight ratio PTQ1:N2200 = 70:30) solar cell with the best PCE of 4.1% under AM 1.5G illumination from a calibrated solar simulator with an intensity of  $100 \text{ mW cm}^{-2}$  (solid line) and under dark conditions (dashed line).  $J_{\text{SC}} = 8.85 \text{ mA cm}^{-2}$ ,  $\text{FF} = 0.55$ , and  $V_{\text{OC}} = 0.84$ . (b) EQE spectrum of the PTQ1/N2200 BHJ solar cell.

**Table 5-1.** Photovoltaic parameters of the devices.

Weight ratio of PTQ1:N2200	$J_{\text{SC}} / \text{mA cm}^{-2}$	FF	$V_{\text{OC}} / \text{V}$	PCE / %
20:80	4.84	0.37	0.79	1.4
30:70	7.07	0.39	0.81	2.2
40:60	7.48	0.48	0.81	2.9
50:50	7.67	0.54	0.82	3.4
60:40	8.48	0.53	0.83	3.7
70:30	8.85	0.55	0.84	4.1
80:20	7.73	0.59	0.84	3.8

wt% to optimize the device performance. The solar cell performances of the devices with various donor:acceptor (D:A) compositions are summarized in Table 5-1. The film thickness of the PTQ1/N2200 layers was adjusted to ~85 nm in all the devices. It is interesting that the photovoltaic parameters strongly depended on the D:A ratio. The value of  $J_{SC}$  increased from 4.84 to 8.85 mA cm<sup>-2</sup> when the PTQ1 content was increased from 20 to 70 wt% and it decreased slightly at 80 wt%. The FF increased from 0.37 to 0.59 with increase PTQ1 content and the highest value was obtained for the device with 80 wt% PTQ1. Moreover,  $V_{OC}$  also increased slightly with increase in the PTQ1 content. Hence, the best PCE of 4.1% was attained for the device with a D:A ratio of PTQ1:N2200 = 70:30. Figure 5-3 shows the  $J-V$  curves and the EQE spectrum of the device with the best PCE. The photovoltaic parameters were  $J_{SC} = 8.85$  mA cm<sup>-2</sup>, FF = 0.55,  $V_{OC} = 0.84$  V, and PCE = 4.1%. In addition, the EQE approached 50% at 630 nm. The marked dependence of the PCE suggests the importance of controlling the D:A blending ratio during the fabrication of the polymer/polymer BHJ solar cells. Moreover, the PCE was optimized at a donor rich blend ratio, which is in contrast with that reported for polymer/fullerene BHJ solar cells.

The author first focuses on the light absorption and the charge generation efficiencies in the PTQ1/N2200 blended films to discuss the dependence of PCE on the PTQ1 content. The number of photons absorbed by the PTQ1/N2200 blended films was evaluated from the integral of the product of the absorption of the PTQ1/N2200 layer and the solar spectrum. The results revealed that the number of photons was almost independent of the PTQ1 content; the decrease in the PTQ1 absorption could be compensated with the increase in the N2200 absorption (see Appendix, Figures 5-A1 and 5-A2). This is one of the advantages of polymer/polymer BHJ solar cells in which both D and A polymers can harvest the solar light. Therefore, the increase in  $J_{SC}$  could not be attributed to the increase in light absorption by the photoactive layers.

Next, the charge generation following the light absorption is discussed on the basis of the photoluminescence (PL) quenching, since the charge generation efficiency can be inferred from the degree of PL quenching. The PL spectra of the blended films were measured by selective excitation of the PTQ1 and the N2200 components (see Appendix, Table 5-A1). As shown in Figure 5-4, the quenching efficiency of N2200 ( $\Phi_q(A)$ ) was 77% for the blended film with a D:A ratio of PTQ1:N2200 = 60:40. However, the efficiency was reduced to as low as 47% when the ratio of PTQ1:N2200 was 20:80. This marked decrease in ( $\Phi_q(A)$ ) indicates that a large number of photogenerated excitons in the photoactive layer deactivate radiatively to the ground state before arriving at the heterojunction interface because the size of the N2200-rich phase grew beyond the exciton diffusion length ( $L_D \leq 10$  nm) with increase in the N2200 content.<sup>9,17</sup> In other words, a large number of photogenerated excitons cannot dissociate into charges for the samples with high N2200 content. On the other hand, the PL from PTQ1 was highly quenched

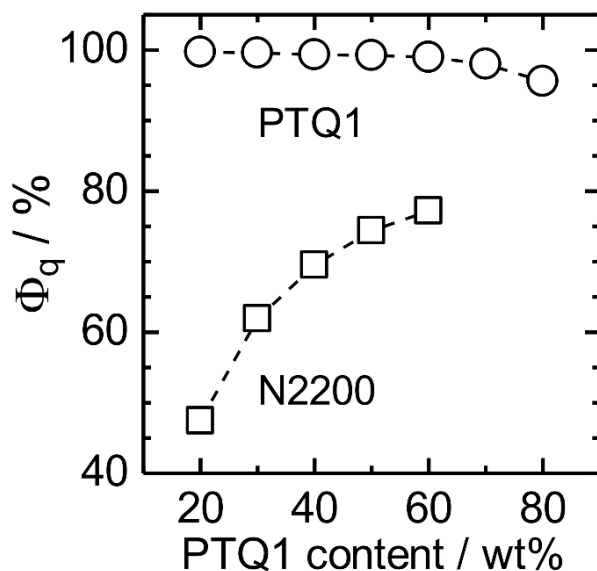


**Figure 5-4.** Photoluminescence quenching efficiencies  $\Phi_q$  of PTQ1 (circles) and N2200 (squares) in the PTQ1/N2200 blended films as a function of PTQ1 weight percentage.

regardless of the blend composition and the PL quenching efficiency of PTQ1 ( $\Phi_q(D)$ ) was higher than 96%. This suggests that the size of the PTQ1-rich phase remained small even for the samples with high PTQ1 content. In addition, as shown in Figure 5-1c, the PL spectrum of PTQ1 overlapped well with the absorption spectrum of N2200. Therefore, the quenching of the PTQ1 excitons would be enhanced by the long-range resonant energy transfer from PTQ1 to N2200, because the energy transfer allows transport of the PTQ1 excitons to the heterojunction interface at distances beyond  $L_D$ .<sup>23,24</sup> The author thus concludes that the increase in  $J_{SC}$  with increasing PTQ1 content was caused by the favorable phase separated structure of PTQ1 and the effective energy transfer to N2200, both resulting in efficient charge generation with minimal loss of absorbed photons.

Following the discussion on charge generation, the author further focuses on the charge transport efficiency in terms of the charge-carrier mobilities in the blended films because mobility is one of the key parameters that dominates the charge transport to the electrodes.<sup>25,26</sup> The hole mobility  $\mu_h$  and the electron mobility  $\mu_e$  in both the neat and the blended films were measured using the space-charge-limited current (SCLC) method with the Mott–Gurney equation (see Appendix, Figures 5-A3 and 5-A4).<sup>27</sup> The dependence of the mobilities on the D:A composition is shown in Figure 5-5. The PTQ1 neat film exhibited a hole mobility of  $\mu_h = 2.5 \times 10^{-5} \text{ cm}^2 \text{ V}^{-1} \text{ s}^{-1}$  and the N2200 neat film showed an electron mobility of  $\mu_e = 4.6 \times 10^{-3} \text{ cm}^2 \text{ V}^{-1} \text{ s}^{-1}$ , which were close to the values reported previously.<sup>28,29</sup> As shown in Figure 5-5,  $\mu_h$  increased from  $2.6 \times 10^{-6}$  to  $1.2 \times 10^{-5} \text{ cm}^2 \text{ V}^{-1} \text{ s}^{-1}$  with increase in the PTQ1 content from 20 to 80 wt%. In contrast,  $\mu_e$  remained much higher than  $\mu_h$  among the blended compositions. As a result, the hole mobility became more balanced with the electron mobility with an increase in the PTQ1 content. Considering the FFs shown in Table 5-1, it can be concluded that the control of the D:A blending ratio is essential to achieve a balance between the hole and electron mobilities,

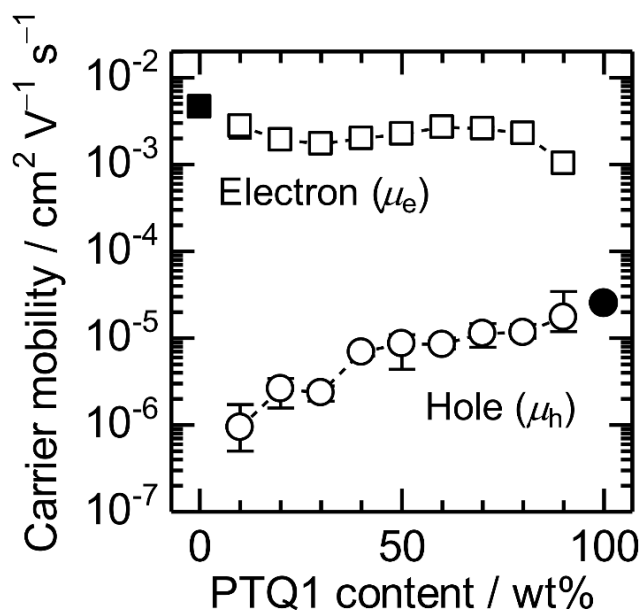


**Figure 5-5.** Hole (open circles) and electron (open squares) mobilities in PTQ1/N2200 blended films as a function of PTQ1 weight percentage. The solid circle and square indicate the hole and electron mobilities in the PTQ1 and N2200 neat films, respectively. The mobilities were calculated from SCLC currents measured for the hole-only devices consisting of ITO|PEDOT:PSS and Au electrodes (hole mobility) and the electron-only devices consisting of Al and Cs<sub>2</sub>CO<sub>3</sub>|Al electrodes (electron mobility).

which is the key to obtaining high FFs. It is worth noting that the D:A blending ratio for achieving an optimal FF differed between the PTQ1/N2200 and the PTQ1/fullerene BHJ solar cells. In the case of the PTQ1/fullerene BHJs, the best FF was obtained with a fullerene content of 70–80 wt%,<sup>19</sup> while just 20–30 wt% of N2200 provided optimal FF in the PTQ1/N2200 BHJs. The neat films of the N2200 and fullerene derivative, [6,6]-phenyl-C<sub>61</sub>-butyric acid methyl ester (PCBM), showed very similar SCLC electron mobilities<sup>30</sup> in the order of  $10^{-3} \text{ cm}^2 \text{V}^{-1} \text{s}^{-1}$ . Therefore, the difference in the optimal blend compositions is probably a result of their different phase-separated morphologies. For polymer/fullerene BHJs, the concentration of the low molecular weight fullerenes should be high enough to ensure the presence of sufficient electron transporting networks throughout

the film;<sup>2</sup> in the blends with amorphous donor polymers such as MDMO-PPV,<sup>31</sup> fluorene copolymers,<sup>32</sup> and PCDTBT,<sup>33</sup> 80 wt% of fullerenes is required to provide optimal FF. The high concentration of the fullerenes, however, decreases the amount of light absorption in the photoactive layer owing to the low absorption coefficients of the fullerenes compared to the donor polymers. In contrast, as an acceptor, N2200 (with a weight-average molecular weight of 178,000 g mol<sup>-1</sup>) could provide sufficient pathways for electron transport through the chain networks even when the concentration was as low as 20 wt%, indicating one of the advantages in utilizing a polymer as an acceptor. The preferable formation of interpenetrating networks by both D and A polymers allows for the adjustment of the D:A blending ratio in a wide range without losing charge transport pathways.

### 5.3. Conclusions

The author has demonstrated that polymer/polymer BHJs consisting of low-bandgap D and A polymers is a potential alternative to conventional polymer/fullerene BHJs. The device performance is optimized at the D:A blending ratio of 70:30 wt%, giving rise to a maximum EQE of 50% at 630 nm,  $J_{SC}$  of 8.85 mA cm<sup>-2</sup>, FF of 0.55,  $V_{OC}$  of 0.84 V, and the best PCE of 4.1%. From the PL quenching measurements, efficient charge generation from both PTQ1 and N2200 excitons is observed with increase in the PTQ1 content to up to 80 wt%. The SCLC mobility measurements show that the hole mobility of PTQ1/N2200 blends increases with increase in the PTQ1 content and is in balance with the electron mobility of N2200. Hence,  $J_{SC}$  and FF are successfully improved for devices containing higher amounts PTQ1 than N2200. In addition to efficient light absorption at longer wavelengths by both D and A polymers, the excitons generated in the D polymer are effectively conveyed to the interface with the A polymer *via* energy transfer. The D:A composition of the polymers can be adjusted in a wide range of blending ratios without

losing charge transport pathways owing to the interpenetrated network of polymer chains. Consequently, the PTQ1/N2200 BHJ device shows EQE of 50% and PCE of 4.1%, which are one of the highest values reported for polymer/polymer BHJ solar cells.

#### 5.4. Experimental

*Materials:* The polymers PTQ1 and N2200 were obtained from Solarmer Energy, Inc. and Polyera Corporation, respectively, and used as received. The weight-average molecular weight  $M_w$ , and polydispersity index (PDI; given by  $M_w/M_n$ , where  $M_n$  is the number-average molecular weight) of PTQ1 were 113,000 g mol<sup>-1</sup> and 2.4, respectively, while those of N2200 were 178,000 g mol<sup>-1</sup> and PDI = 3.7, respectively. The values were measured by size-exclusion chromatography (Shodex, GPC-101) using *o*-dichlorobenzene as the eluent, which was calibrated against monodisperse polystyrene standards (Shodex, STANDARD S-Series). The HOMO levels of the PTQ1 and N2200 neat films were estimated by photoelectron yield spectroscopy (Riken Keiki, AC-3).

*Device Fabrication and Measurements:* Indium–tin–oxide (ITO)-coated glass substrates (10 Ω per square) were washed by ultrasonication with toluene, then acetone, and finally ethanol for 15 min each and then dried under an N<sub>2</sub> flow. The washed substrates were further treated with a UV–O<sub>3</sub> cleaner (Nippon Laser & Electronics Lab., NL-UV253S) for 30 min. A 40-nm-thick topcoat layer of poly(3,4-ethylenedioxythiophene):poly(4-styrenesulfonate) (PEDOT:PSS; H.C. Stark PH-500) was spin-coated onto the ITO substrate at a spinning rate of 3000 rpm (rotations per minute) for 99 s and then dried in air at 140 °C for 10 min. A blended layer of PTQ1/N2200 was spin-coated onto the PEDOT:PSS film at 3000 rpm for 60 s from CF solutions. All PTQ1/N2200 blended films used in this study were spin-coated from CF solutions in which PTQ1 and N2200 were dissolved at weight ratios that varied from 20:80 to 80:20. The total concentration of these blended solutions was maintained at

12 mg mL<sup>-1</sup> to keep the film thickness constant. The thickness of the PTQ1/N2200 blended layers was typically 85 nm. Preparation of the CF solutions and the subsequent spin-coating of the solutions onto the PEDOT:PSS film were carried out in an N<sub>2</sub>-filled glove box. The photoactive layer was thermally annealed at 120 °C for 10 min in an N<sub>2</sub>-filled glove box, after which a calcium interlayer (Ca, 12 nm) and an aluminum electrode (Al, 70 nm) were vacuum-deposited at 2.5 × 10<sup>-4</sup> Pa. The area of the circular Ca/Al electrode was 0.07 cm<sup>2</sup>. The *J-V* characteristics of the devices were measured by using a direct-current voltage and a current source/monitor (Advantest, R6243) under illumination by “air mass 1.5-Global” (AM 1.5G) simulated solar light with 100 mW cm<sup>-2</sup>. The light intensity was corrected with a calibrated silicon photodiode reference cell (Bunko-Keiki, BS-520, active area: 0.0534 cm<sup>2</sup>). The EQE spectra were measured with a digital electrometer (Advantest, R8252) under the illumination of monochromatic light from a 500-W xenon lamp (Thermo Oriel, 66921) with optical cut filters and a monochromator (Thermo Oriel, UV-visible Cornerstone). The spectral-mismatch factor calculated with respect to the AM 1.5G spectrum for the PTQ1/N2200 (weight ratio PTQ1:N2200 = 70:30) test cell and the BS-520 silicon reference cell combination was 1.01<sup>34</sup>. The *J*<sub>SC</sub> value increased almost linearly with illumination from low intensities (as for the EQE measurement) to 100 mW cm<sup>-2</sup>. The active area of the device was 0.07 cm<sup>2</sup>, which was determined from the area of the top Ca/Al electrode. To minimize the *edge effect*, the author used the device layout that consists of unpatterned PEDOT:PSS and PTQ1/N2200 layers sandwiched between unpatterned ITO and Ca/Al top electrodes. In this layout, the photoactive area can be assumed to the area of the Ca/Al top electrode.<sup>35</sup> The devices were illuminated from the ITO side. All these measurements were carried out under an atmosphere of N<sub>2</sub> at room temperature. The device structure is depicted in Appendix, Figure 5-A5. At least 11 devices were fabricated

to ensure the reproducibility of the  $J$ - $V$  characteristics. The photovoltaic parameters that were averaged over 11 devices are summarized in Appendix, Table 5-A2.

*Mobility Measurements:* Hole-only devices were fabricated by the following procedure. A PTQ1 neat layer and a PTQ1/N2200 blended layer were spin-coated on separate ITO substrates covered with 40-nm-thick PEDOT:PSS, which acted as the anode. A gold electrode (Au, 50 nm) was then vacuum-deposited on each layer as the cathode (ITO|PEDOT:PSS|PTQ1|Au and ITO|PEDOT:PSS|PTQ1/N2200|Au). Thickness of the PTQ1 neat layer and the PTQ1/N2200 blended layer were 138 nm and 100 nm, respectively. Electron-only devices were fabricated by the following procedure. A 50-nm-thick Al layer, which acted as the anode, was vacuum-deposited on a glass substrate covered with 20-nm-thick poly(sodium 4-styrenesulfonate) (PSS,  $M_w = 70,000 \text{ g mol}^{-1}$ ). A neat layer of N2200 and a PTQ1/N2200 blended layer were spin-coated onto each Al electrode. A  $\text{Cs}_2\text{CO}_3$  interlayer (4 nm) and an Al (80 nm) layer were then vacuum-deposited as the cathode (Al|N2200| $\text{Cs}_2\text{CO}_3$ |Al and Al|PTQ1/N2200| $\text{Cs}_2\text{CO}_3$ |Al). Thickness of the N2200 neat layer and the PTQ1/N2200 blended layer were 98 nm and 85 nm, respectively. The  $\text{Cs}_2\text{CO}_3$  layer was used to enhance the efficiency of electron injection.<sup>36</sup> The dark current density–voltage ( $J$ - $V$ ) characteristics of the devices were measured in air (hole-only devices) and in  $\text{N}_2$  atmosphere (electron-only devices) by using a direct-current voltage and a current source/monitor (Advantest, R6243). The PTQ1 and N2200 neat layers were spin-coated from chlorobenzene solutions. The PTQ1/N2200 blended layers were spin-coated from CF solutions in which PTQ1 and N2200 were dissolved at weight ratios ranging from 10:90 to 90:10.

*Photoluminescence Quenching Measurements:* Photoluminescence (PL) spectra were measured for the PTQ1 and N2200 neat films and the PTQ1/N2200 blended films, which were spin-coated onto quartz substrates and annealed at 120 °C for 10 min, using a calibrated

fluorescence spectrophotometer (Horiba, NanoLog). The samples were excited at 600 nm to excite primarily the PTQ1 component and at 720 nm to excite the N2200 component. Excitation fractions of PTQ1 and N2200 in the PTQ1/N2200 blended films are listed in Appendix, Table 5-A1. The PL quenching efficiency of PTQ1 was evaluated from the ratio of the PL intensity of PTQ1 for the PTQ1/N2200 blended films to that for a PTQ1 neat film (after each PL intensity was corrected for variations in the PTQ1 absorption at 600 nm). The PL quenching efficiency of N2200 was evaluated from the ratio of the PL intensity of N2200 for the PTQ1/N2200 blended films to that for an N2200 neat film (after each PL intensity was corrected for variations in the N2200 absorption at 720 nm).

*AFM Measurements:* AFM images were collected in tapping mode (Shimadzu, SPM-9600) using silicon probes with a resonant frequency of ~150 kHz and a force constant of ~9 N m<sup>-1</sup> (Olympus, OMCL-AC200TS).

## 5.5. Appendix

### 5.5.1. Calculation of the Number of Photons Absorbed by PTQ1/N2200 Layers

The number of photons absorbed by the PTQ1/N2200 blended films,  $N_{\text{ph}}$ , was calculated using the following equation.

$$N_{\text{ph}} = \int_{350 \text{ nm}}^{900 \text{ nm}} \frac{N_{\text{AM1.5G}}(\lambda) \cdot \%Abs(\lambda) \cdot d\lambda}{100} \quad (\text{A1})$$

In A5.5.1,  $N_{\text{AM1.5G}}$  is the number of photons included in AM 1.5G solar light,  $\%Abs$  is the percentage absorption of the PTQ1/N2200 blended films, and  $\lambda$  is the wavelength. The value of  $\%Abs$  was calculated from the absorbance ( $Abs$ ) of the blended films as  $\%Abs(\lambda) = (1 - 10^{-Abs(\lambda)}) \times 100$ . The absorbance was measured in reflection geometry at an incident angle of 5° normal to the substrate (Hitachi, U-4100) for the blended films covered with an Al top electrode. Figure 5-A1 shows the reflection absorption spectra of the blended films used for the calculation. These blended films were spin-coated from CF solutions onto

glass substrates under the same conditions used for the device fabrication. Figure 5-A2 shows normalized  $N_{ph}$  as a function of PTQ1 weight percentage.

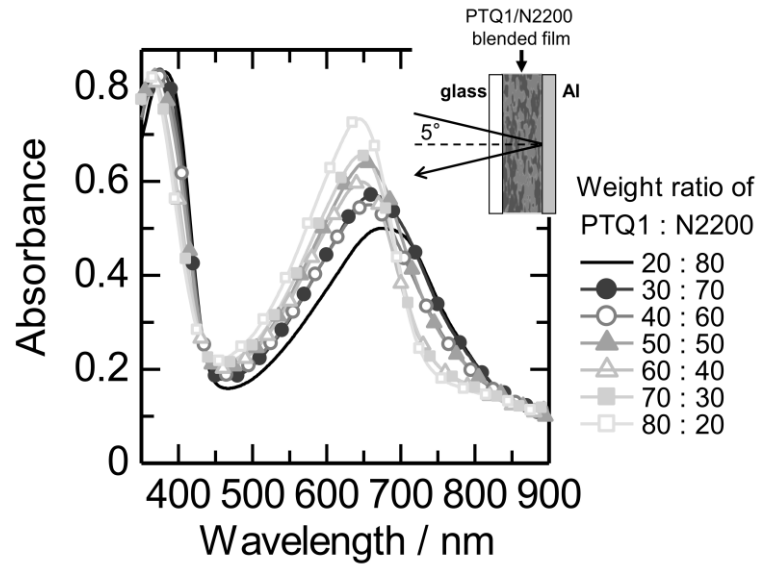


**Figure 5-A1.** Reflection absorption spectra of the PTQ1/N2200 blended films. The inset shows a schematic of the film structure.

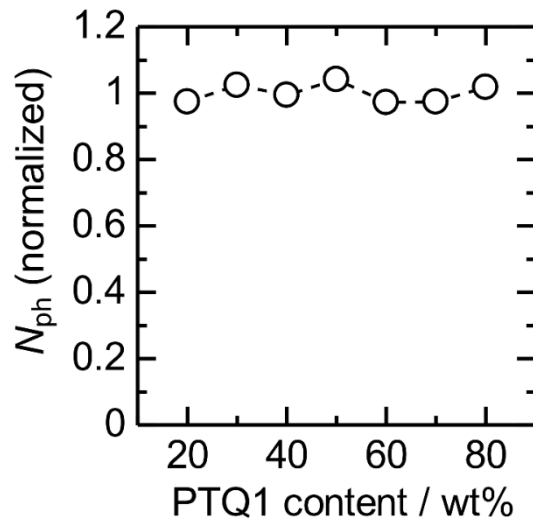


**Figure 5-A2.** Normalized  $N_{ph}$  as a function of PTQ1 weight percentage.

### 5.5.2. Photoluminescence Quenching Measurements

Photoluminescence spectra of the PTQ1/N2200 blended films were measured by selective excitation of the PTQ1 and N2200 components at 600 nm and 720 nm, respectively.

The excitation fractions are summarized in Table 5-A1.

**Table 5-A1.** Excitation fractions of PTQ1 and N2200 in the PTQ1/N2200 blended films.

Weight ratio of PTQ1:N2200	Excitation fraction / %	
	PTQ1 (at 600 nm)	N2200 (at 720 nm)
20:80	41	94
30:70	52	91
40:60	61	88
50:50	69	83
60:40	76	78
70:30	82	—
80:20	88	—

### 5.5.3. Mobility Measurements

Charge-carrier mobilities ( $\mu$ ) were evaluated from the  $J$ - $V$  characteristics using the space-charge-limited current (SCLC) method with the Mott–Gurney equation for the current density  $J_{\text{SCLC}}$  expressed as  $J_{\text{SCLC}} = \frac{9}{8} \varepsilon_0 \varepsilon_r \mu \frac{V^2}{L^3}$ , where  $\varepsilon_0$  is the vacuum permittivity,  $\varepsilon_r$  is the dielectric constant of the film ( $\varepsilon_r = 3$  was assumed), and  $L$  is the thickness of the active layer.<sup>27,A1</sup> The  $J$ - $V$  characteristics of the hole-only devices and those of the electron-only devices are shown in Figures 5-A3 and A4, respectively.

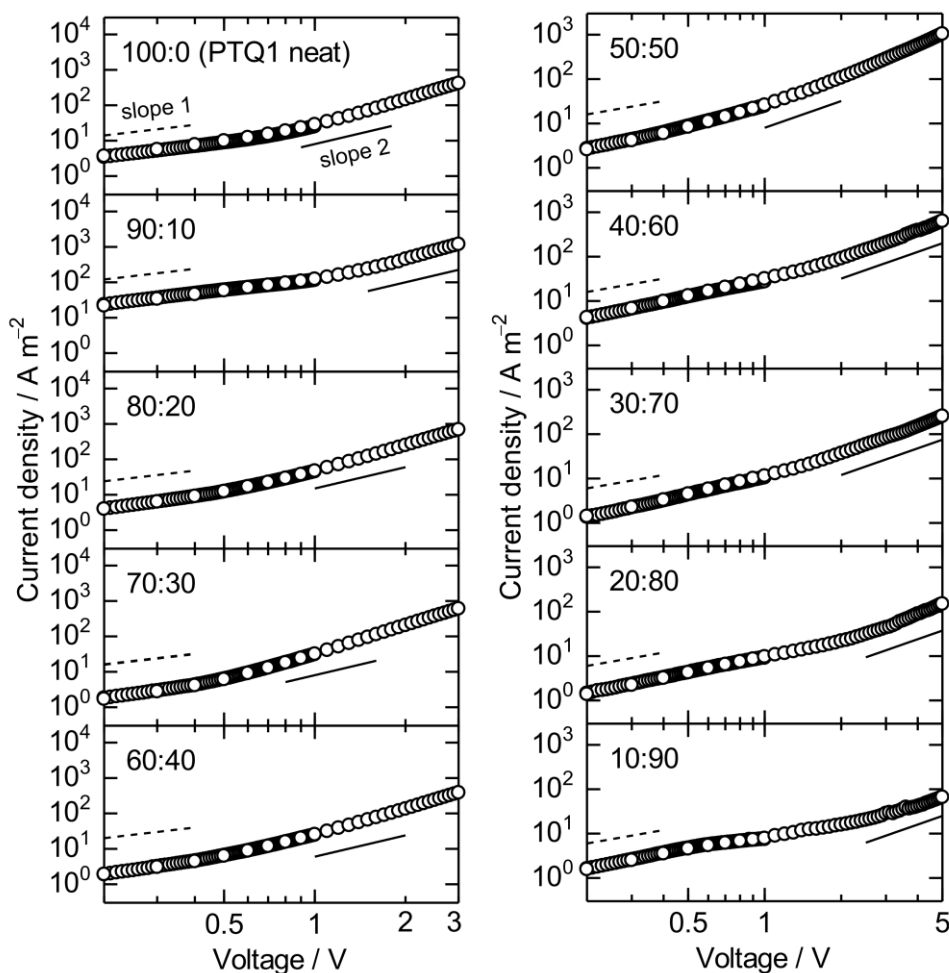


**Figure 5-A3.**  $J$ - $V$  characteristics of ITO|PEDOT:PSS|PTQ1(138 nm)|Au and ITO|PEDOT:PSS|PTQ1/N2200(100 nm)|Au hole-only devices with different PTQ1:N2200 weight ratios.

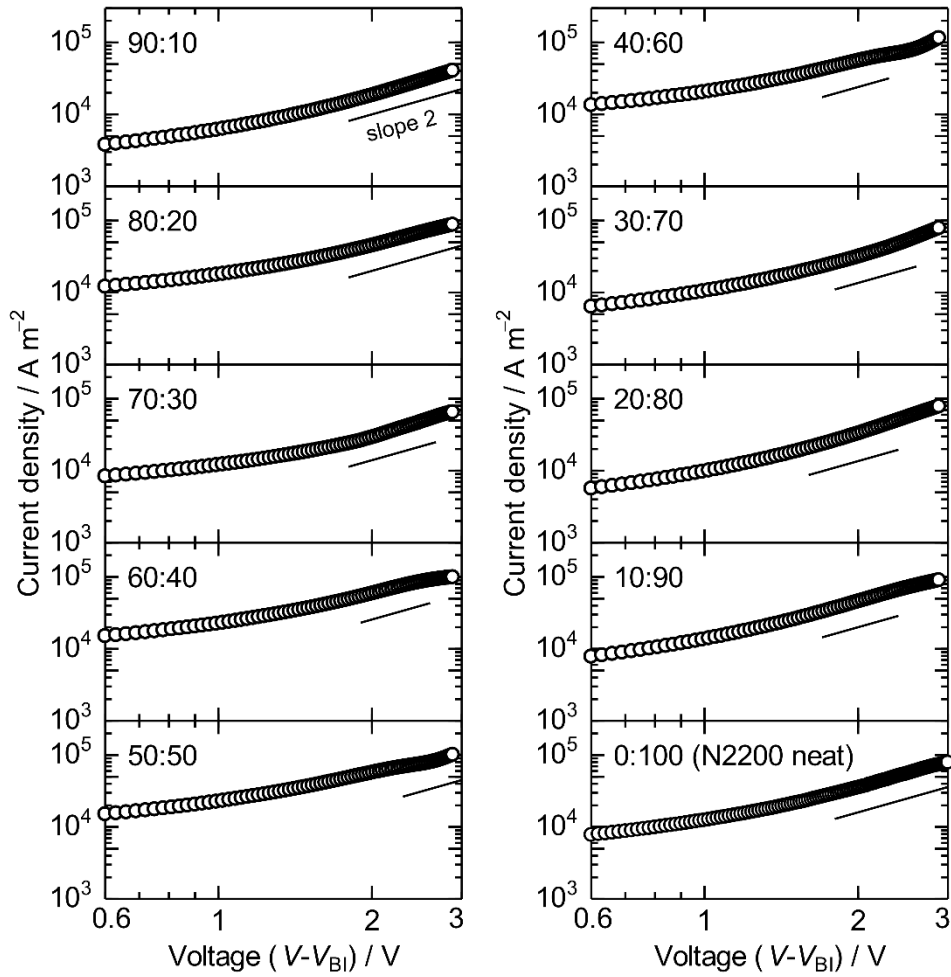


**Figure 5-A4.**  $J$ - $V$  characteristics of Al|N2200(98 nm)|Cs<sub>2</sub>CO<sub>3</sub>/Al and Al|PTQ1/N2200(85 nm)|Cs<sub>2</sub>CO<sub>3</sub>/Al electron-only devices with different PTQ1:N2200 weight ratios. The applied voltage  $V$  was corrected for the built-in voltage  $V_{BI}$  of 2.1 V.<sup>A2,A3</sup>

#### 5.5.4. Averaged Values of the Photovoltaic Parameters

**Table 5-A2.** Photovoltaic parameters of the devices.

Weight ratio of PTQ1:N2200	$J_{sc} / \text{mA cm}^{-2}$ (Average) <sup>a</sup>	FF (Average) <sup>a</sup>	$V_{oc} / \text{V}$ (Average) <sup>a</sup>	PCE / % (Average) <sup>a</sup>
20:80	4.4	0.38	0.78	1.3
30:70	6.6	0.39	0.81	2.1
40:60	7.4	0.46	0.82	2.8
50:50	7.7	0.52	0.83	3.3
60:40	8.0	0.55	0.84	3.7
70:30	8.4	0.56	0.84	4.0
80:20	7.5	0.59	0.85	3.8

<sup>a</sup> The photovoltaic parameters are averaged values over 11 devices.

#### 5.5.5. Device Structure

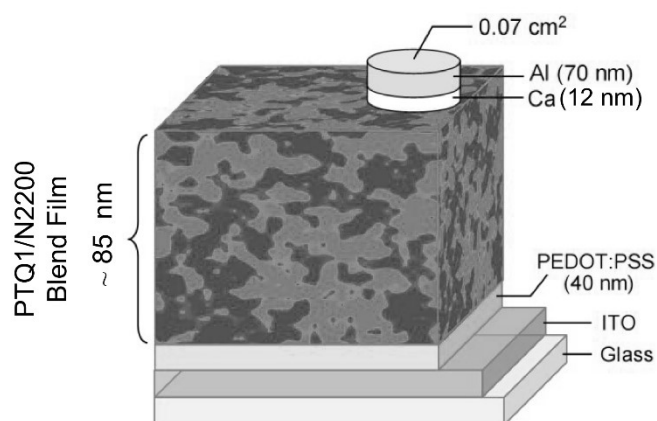


**Figure 5-A5.** Schematic illustration of the device structure.

## 5.6. References and Note

- [1] R. Søndergaard, M. Hösel, D. Angmo, T. T. Larsen-Olsen, F. C. Krebs, *Mater. Today* **2012**, *15*, 36–49.
- [2] M. T. Dang, L. Hirsch, G. Wantz, J. D. Wuest, *Chem. Rev.* **2013**, *113*, 3734–3765.
- [3] G. Li, R. Zhu, Y. Yang, *Nat. Photon.* **2012**, *6*, 153–161.
- [4] C. J. Brabec, S. Gowrisanker, J. J. M. Halls, D. Laird, S. Jia, S. P. Williams, *Adv. Mater.* **2010**, *22*, 3839–3856.
- [5] H. Ohkita, S. Ito, *Polymer* **2011**, *52*, 4397–4417.
- [6] C. R. McNeill, *Energy Environ. Sci.* **2012**, *5*, 5653–5667.
- [7] C. R. McNeill, N. C. Greenham, *Adv. Mater.* **2009**, *21*, 3840–3850.
- [8] See Chapter 4.
- [9] See Chapter 2.
- [10] E. Zhou, J. Cong, Q. Wei, K. Tajima, C. Yang, K. Hashimoto, *Angew. Chem. Int. Ed.* **2011**, *50*, 2799–2803.
- [11] Z. He, C. Zhong, S. Su, M. Xu, H. Wu, Y. Cao, *Nat. Photon.* **2012**, *6*, 591–595.
- [12] C. R. McNeill, A. Abrusci, I. Hwang, M. A. Ruderer, P. Müller-Buschbaum, N. C. Greenham, *Adv. Funct. Mater.* **2009**, *19*, 3103–3111.
- [13] X. Liu, S. Huettner, Z. Rong, M. Sommer, R. H. Friend, *Adv. Mater.* **2012**, *24*, 669–674.
- [14] M. Schubert, D. Dolfen, J. Frisch, S. Roland, R. Steyrlleuthner, B. Stiller, Z. Chen, U. Scherf, N. Koch, A. Facchetti, D. Neher, *Adv. Energy Mater.* **2012**, *2*, 369–380.
- [15] H. Yan, B. A. Collins, E. Gann, C. Wang, H. Ade, C. R. McNeill, *ACS Nano* **2012**, *6*, 677–688.
- [16] S. Swaraj, C. Wang, H. Yan, B. Watts, J. Lüning, C. R. McNeill, H. Ade, *Nano Lett.* **2010**, *10*, 2863–2869.

- [17] C. R. McNeill, S. Westenhoff, C. Groves, R. H. Friend, N. C. Greenham, *J. Phys. Chem. C* **2007**, *111*, 19153–19160.
- [18] R. C. Mulherin, S. Jung, S. Huettner, K. Johnson, P. Kohn, M. Sommer, S. Allard, U. Scherf, N. C. Greenham, *Nano Lett.* **2011**, *11*, 4846–4851.
- [19] E. Wang, L. Hou, Z. Wang, S. Hellström, F. Zhang, O. Inganäs, M. R. Andersson, *Adv. Mater.* **2010**, *22*, 5240–5244.
- [20] H. Yan, Z. Chen, Y. Zheng, C. Newman, J. R. Quinn, F. Dötz, M. Kastler, A. Facchetti, *Nature* **2009**, *457*, 679–686.
- [21] G. Dennler, M. C. Scharber, C. J. Brabec, *Adv. Mater.* **2009**, *21*, 1323–1338.
- [22] T. W. Holcombe, J. E. Norton, J. Rivnay, C. H. Woo, L. Goris, C. Piliego, G. Griffini, A. Sellinger, J. L. Brédas, A. Salleo, J. M. J. Fréchet, *J. Am. Chem. Soc.* **2011**, *133*, 12106–12114.
- [23] K. Feron, W. J. Belcher, C. J. Fell, P. C. Dastoor, *Int. J. Mol. Sci.* **2012**, *13*, 17019–17047.
- [24] S. R. Scully, P. B. Armstrong, C. Edder, J. M. J. Fréchet, M. D. McGehee, *Adv. Mater.* **2007**, *19*, 2961–2966.
- [25] J. Nakamura, K. Murata, K. Takahashi, *Appl. Phys. Lett.* **2005**, *87*, 132105.
- [26] L. J. A. Koster, V. D. Mihailetschi, M. Lenes, P. W. M. Blom, in *Organic Photovoltaics: Materials, Device Physics, and Manufacturing Technologies*, (Eds.: C. Brabec, V. Dyakonov, U. Scherf), Wiley-VCH, Weinheim, Germany **2008**, pp. 283–297.
- [27] Y. Shen, A. R. Hosseini, M. H. Wong, G. G. Malliaras, *ChemPhysChem.* **2004**, *5*, 16–25.
- [28] L. M. Andersson, *Org. Electron.* **2011**, *12*, 300–305.
- [29] R. Steyrleuthner, M. Schubert, F. Jaiser, J. C. Blakesley, Z. Chen, A. Facchetti, D.

- Neher, *Adv. Mater.* **2010**, *22*, 2799–2803.
- [30] V. D. Mihailetschi, J. K. J. van Duren, P. W. M. Blom, J. C. Hummelen, R. A. J. Janssen, J. M. Kroon, M. T. Rispens, W. J. H. Verhees, M. M. Wienk, *Adv. Funct. Mater.* **2003**, *13*, 43–46.
- [31] J. K. J. van Duren, X. Yang, J. Loos, C. W. T. Bulle-Lieuwma, A. B. Sieval, J. C. Hummelen, R. A. J. Janssen, *Adv. Funct. Mater.* **2004**, *14*, 425–434.
- [32] L. M. Andersson, F. Zhang, O. Inganäs, *Appl. Phys. Lett.* **2007**, *91*, 071108.
- [33] S. Wakim, S. Beaupré, N. Blouin, B. Aich, S. Rodman, R. Gaudiana, Y. Tao, M. Leclerc, *J. Mater. Chem.* **2009**, *19*, 5351–5358.
- [34] V. Shrotriya, G. Li, Y. Yao, T. Moriarty, K. Emery, Y. Yang, *Adv. Funct. Mater.* **2006**, *16*, 2016–2023.
- [35] A. Cravino, P. Schilinsky, C. J. Brabec, *Adv. Funct. Mater.* **2007**, *17*, 3906–3910.
- [36] G. J. A. H. Wetzelaer, M. Kuik, Y. Olivier, V. Lemaire, J. Cornil, S. Fabiano, M. A. Loi, P. W. M. Blom, *Phys. Rev. B* **2012**, *86*, 165203.
- [37] The LUMO energy determined from cyclic voltammetry measurements performed on the polymer thin film was  $-3.91$  eV: Z. Chen, Y. Zheng, H. Yan, A. Facchetti, *J. Am. Chem. Soc.* **2009**, *131*, 8–9.
- [A1] M. A. Lampert, P. Mark, *Current Injection in Solids*, Academic Press, New York, **1970**.
- [A2] The  $V_{BI}$  was determined from the difference of the work functions between Al anode (4.3V) and  $Cs_2CO_3/Al$  cathode (2.2 eV).<sup>A3</sup>
- [A3] J. Huang, Z. Xu, Y. Yang, *Adv. Funct. Mater.* **2007**, *17*, 1966–1973.

## Chapter 6

# Efficient Charge-Carrier Generation and Collection in Low-Bandgap Donor/Acceptor Polymer Blend Solar Cells with High Charge-Carrier Mobilities

### 6.1. Introduction

Currently, the most widely studied polymer-based solar cells consist of a bulk-heterojunction (BHJ) structure in which a conjugated polymer is mixed with a low-molecular-weight fullerene derivative. In these systems, the conjugated polymer acts as an electron donor and the fullerene derivative acts as an acceptor. The power conversion efficiencies (PCEs) of polymer/fullerene BHJ solar cells have increased over the past two decades, and approaching 10% in single-junction cells.<sup>1,2</sup> This improvement is mainly because various low-bandgap donor polymers have been developed with rational molecular designs.<sup>3-7</sup> On the other hand, polymer/polymer BHJ solar cells, which consist of a polymer donor and polymer acceptor, have a number of potential advantages over conventional polymer/fullerene BHJ solar cells. Of particular importance is the flexible molecular design of not only the donor but also the acceptor polymers, which allows for fine tuning of the optical, electronic, and morphological properties of the materials. Consequently, recent studies have been devoted to developments of polymer acceptors.<sup>8</sup>

Owing to considerable efforts in synthesizing various polymer acceptors and optimizing the blend morphology, the PCE of polymer/polymer BHJ solar cells has been steadily improving up to 2 – 4% in the last few years.<sup>8-19</sup> However, these PCEs are still much lower than the efficiencies of polymer/fullerene BHJ solar cells. Even in the most efficient polymer/polymer BHJ solar cells, the maximum external quantum efficiency (EQE)

is as low as 40 – 50%<sup>15,16,18,19</sup>, which is far below that of polymer/fullerene solar cells (70 – 80%).<sup>1,3–5</sup> Such low EQEs of polymer/polymer BHJ solar cells are generally considered to be due to poor charge-carrier generation and/or collection efficiencies<sup>8,17,20–22</sup>, implying that polymer/polymer BHJ solar cells might be inherently inferior to polymer/fullerene BHJ solar cells.

In this chapter, the author demonstrates highly efficient donor/acceptor polymer blend solar cells with a maximum EQE of ~60% and a PCE of 5.73%, which are the highest efficiencies reported for polymer/polymer BHJ solar cells. Based on the applied reverse (negative) voltage dependence of the photocurrent under various intensities of the incident light, the author finds that both the charge-carrier generation and collection efficiencies are as high as 80% in this polymer blend. This finding demonstrates that polymer/polymer solar cells have the potential to improve the device performance, making it as efficient as polymer/fullerene solar cells.

Poly{[*N,N'*-bis(2-octyldodecyl)-naphthalene-1,4,5,8-bis(dicarboximide)-2,6-diyl]-*alt*-5,5'-(2,2'-bithiophene)} [P(NDI2OD-T2); Polyera ActivInk™ N2200]<sup>23</sup> is one of the attractive polymer acceptor alternatives to fullerenes owing to its high electron mobility, high electron affinity, and light absorption ability at near-infrared wavelengths. Among the low-bandgap polymer donors reported, of particular interest are a series of copolymers composed of alternating benzo[1,2-*b*:4,5-*b'*]dithiophene (BDT) and thieno[3,4-*b*]thiophene (TT) units (denoted PBDTTTs) since they offer very high PCEs for polymer/fullerene BHJ solar cells. This is because of their strong absorption in the long-wavelength region and good hole mobility on the order of  $10^{-4} \text{ cm}^2 \text{ V}^{-1} \text{ s}^{-1}$ .<sup>24–26</sup> In particular, PBDTTTs based on the thienyl-substituted BDT unit have been reported to exhibit higher hole mobilities than those based on alkoxy-substituted BDTs.<sup>27</sup> The author therefore utilized poly[[4,8-bis[5-(2-ethylhexyl)thiophene-2-yl]benzo[1,2-*b*:4,5-*b'*]dithiophene-2,6-diyl][3-fluoro-2-[(2-

ethylhexyl) carbonyl]thieno[3,4-*b*]thiophenediyl]] (PBDTTT-EF-T)<sup>28</sup> as a polymer donor and N2200 as a polymer acceptor (Figure 6-1a). As shown in Figure 6-1b, both PBDTTT-EF-T and N2200 exhibited efficient absorption at around 700 nm, where the photon flux of

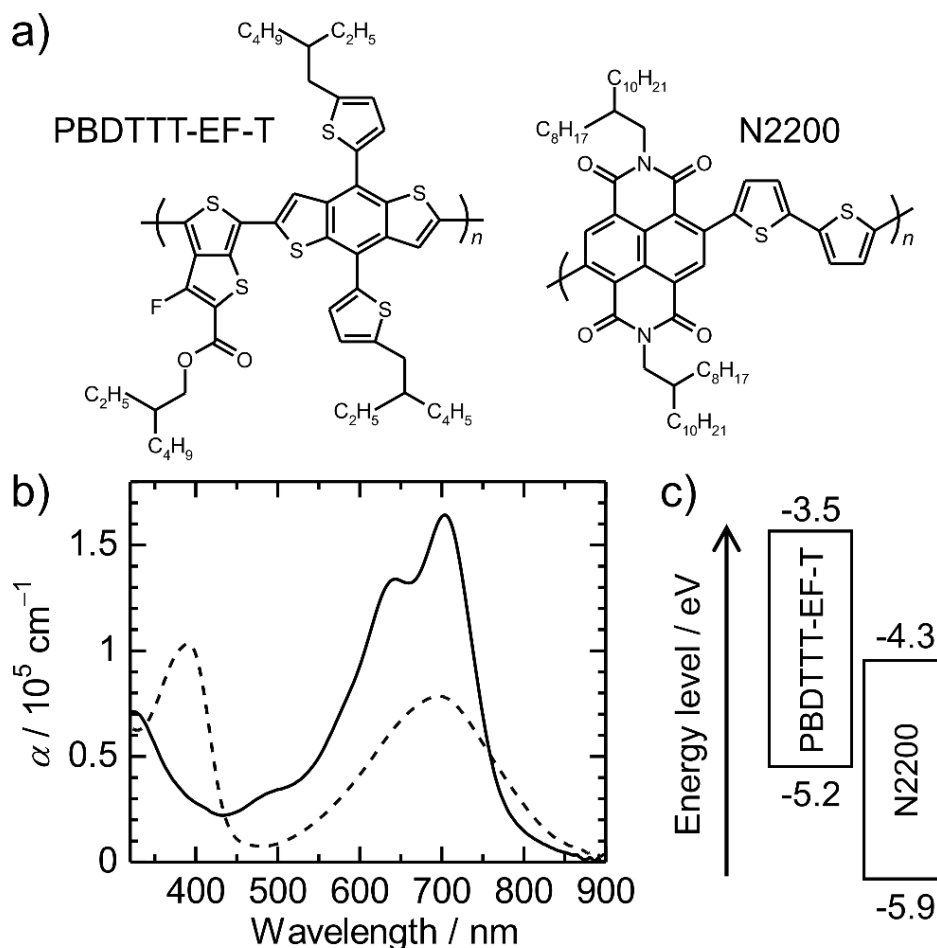


**Figure 6-1.** (a) Chemical structures of PBDTTT-EF-T and N2200. (b) Absorption coefficients ( $\alpha$ ) of PBDTTT-EF-T (solid line) and N2200 (broken line) neat films spin-coated from chlorobenzene. (c) Energy level diagram of PBDTTT-EF-T and N2200 neat films. The HOMO levels were evaluated by photoelectron yield spectroscopy, and the LUMO levels were estimated by adding the optical bandgap energy, calculated from the 0–0 transition, to the HOMO energy (see Appendix, Figure A6-6).

the solar spectrum is the highest, which is important for obtaining a large short-circuit current density ( $J_{SC}$ ). Moreover, the energy offsets both in the lowest unoccupied molecular orbitals (LUMOs, 0.8 eV) and highest occupied molecular orbitals (HOMOs, 0.7 eV) are sufficient to promote efficient electron transfer from the photoexcited state of PBDTTT-EF-T and hole transfer from the photoexcited state of N2200, respectively (Figure 6-1c).<sup>29</sup>

## 6.2. Results and Discussion

The PBDTTT-EF-T/N2200 blend was spin-coated from a chlorobenzene (CB) solution onto poly(3,4-ethylenedioxythiophene):poly(4-styrenesulfonate)-coated (PEDOT:PSS-coated) indium–tin-oxide (ITO) substrates. The weight fraction of PBDTTT-EF-T in the blend was 50%, and the film thickness of the PBDTTT-EF-T/N2200 active layer was adjusted to  $100 \pm 10$  nm. Figure 6-2 shows the  $J$ - $V$  curves and EQE

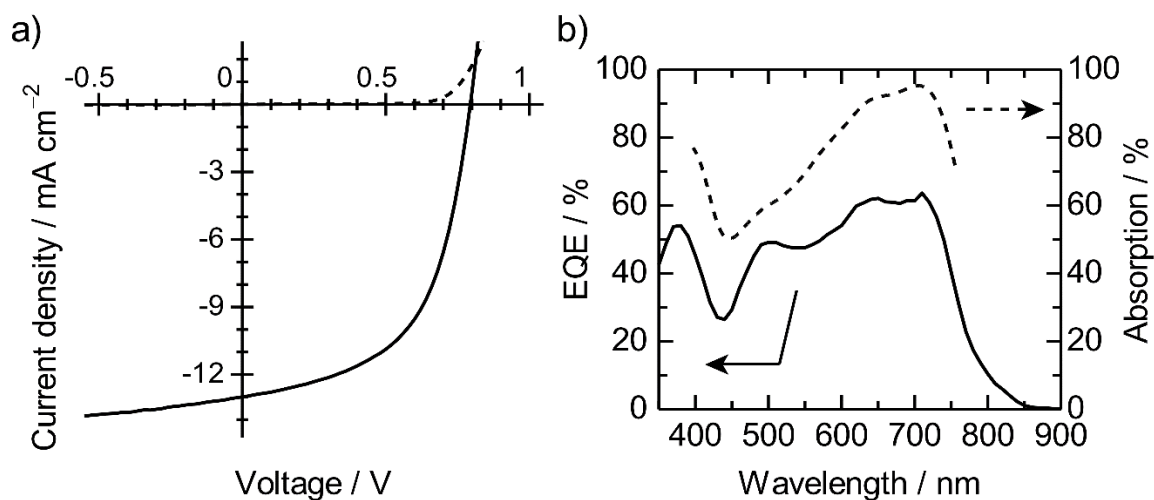


**Figure 6-2.** (a)  $J$ - $V$  characteristics of a PBDTTT-EF-T/N2200 BHJ solar cell with the best PCE of 5.73% under AM 1.5G illumination from a calibrated solar simulator with an intensity of  $100 \text{ mW cm}^{-2}$  (solid line) and in the dark (broken line):  $J_{SC} = 13.0 \text{ mA cm}^{-2}$ ,  $V_{OC} = 0.794$ , and  $FF = 0.556$ . (b) EQE (solid line) and reflection absorption (broken line) spectra of the PBDTTT-EF-T/N2200 BHJ solar cell.

spectrum of the PBDTTT-EF-T/N2200 BHJ solar cell with the best PCE. The photovoltaic parameters including the  $J_{SC}$ , open-circuit voltage ( $V_{OC}$ ), fill factor (FF), and PCE are summarized in Table 6-1. The PBDTTT-EF-T/N2200 BHJ solar cells exhibited a  $J_{SC}$  as high as  $13.0 \text{ mA cm}^{-2}$ , resulting in a PCE of 5.73% under AM 1.5G illumination with an intensity of  $100 \text{ mW cm}^{-2}$ . The author notes that the value of  $J_{SC}$  was close to the photocurrent density calculated by integrating the EQE spectrum with an AM 1.5G reference spectrum (the error was  $\sim 3\%$ ). An EQE value over 50% at 380 nm indicates that N2200 successfully contributes to the photocurrent generation because light absorption at wavelengths around 380 nm is mainly accomplished by N2200, as shown in Figure 6-1b. More importantly, the EQE exceeded 60% in the range of 620 – 720 nm and was still as high as 50% even at 740 nm. The broken line in Figure 6-2b is the reflection absorption spectrum of a PBDTTT-EF-T/N2200 blended film with a thickness of  $\sim 100 \text{ nm}$ , revealing that more than 90% of the incident photons are absorbed around 700 nm because of the efficient light absorption by both PBDTTT-EF-T and N2200. The efficient light absorption at the near-infrared wavelength ranges is responsible for the large  $J_{SC}$  measured for the PBDTTT-EF-T/N2200 BHJ solar cell. As a result, the values for  $J_{SC}$ , maximum EQE, and PCE are the highest reported thus far for polymer/polymer BHJ solar cells.

**Table 6-1.** Photovoltaic Parameters of the PBDTTT-EF-T/N2200 BHJ Solar Cells.

	$J_{SC} / \text{mA cm}^{-2}$	$V_{OC} / \text{V}$	FF	PCE / %
Best	13.0	0.794	0.556	5.73
Average <sup>a</sup>	$13.0 \pm 0.22$	$0.795 \pm 0.00$	$0.534 \pm 0.01$	$5.50 \pm 0.08$

<sup>a</sup> Averaged values over 25 devices. Photovoltaic parameters of the 25 devices are shown in Appendix, Figure S6-1.

To address the origin of the efficient conversion of absorbed photons into photocurrent in the PBDTTT-EF-T/N2200 BHJ solar cell, the author first focuses on the charge-carrier generation and then discuss the charge transport. Figure 6-3 shows the net photocurrent density ( $J_{ph}$ ) as a function of the applied reverse (negative) voltage under illumination at  $100 \text{ mW cm}^{-2}$ . Here,  $J_{ph}$  is given by  $J_{ph} = J_L - J_D$ , where  $J_L$  and  $J_D$  are the current densities under illumination and in the dark, respectively. As shown in Figure 6-3,  $J_{ph}$  was saturated at reverse voltages higher than  $-6 \text{ V}$ , suggesting that at a reverse voltage of  $-6 \text{ V}$ , the electric field within the device would be large enough to sweep out all charge

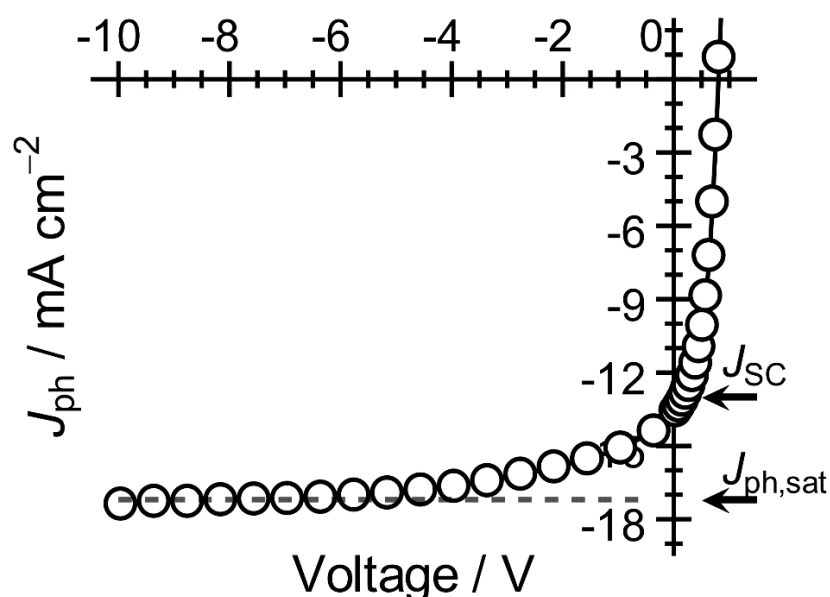


**Figure 6-3.** Photocurrent density ( $J_{ph}$ ) of the PBDTTT-EF-T/N2200 BHJ solar cell as a function of the applied reverse (negative) voltage under AM 1.5G illumination ( $100 \text{ mW cm}^{-2}$ ). The  $J_{ph}$  values were obtained by subtracting the current density in the dark ( $J_D$ ) from that under illumination ( $J_L$ ) as  $J_{ph} = J_L - J_D$ .  $J_{ph,sat}$  and  $J_{sc}$  represent the reverse saturation photocurrent density and short-circuit current density, respectively.

carriers to the electrodes prior to recombination.<sup>30,31</sup> In other words, all of the photogenerated charge carriers in the device are collected at reverse voltages higher than  $-6$  V. The reverse saturation photocurrent density  $J_{\text{ph,sat}}$  was  $17 \text{ mA cm}^{-2}$ . On the other hand, the maximum obtainable photocurrent density ( $J_{\text{max}}$ ) was calculated to be  $\sim 22 \text{ mA cm}^{-2}$  from the integral of the product of the reflection absorption of the PBDTTT-EF-T/N2200 active layer and the incident photon flux density of AM 1.5G solar light (Appendix, Figure 6-A2). Therefore, the charge-carrier generation efficiency in the device can be estimated from the ratio of  $J_{\text{ph,sat}}$  to  $J_{\text{max}}$ . The  $J_{\text{ph,sat}}/J_{\text{max}}$  ratio was as high as 77%, suggesting efficient charge-carrier generation in the PBDTTT-EF-T/N2200 BHJ solar cell. The exciton quenching efficiency following light absorption is also estimated based on the photoluminescence (PL) quenching.<sup>18</sup> The PL spectra of the blended films were measured by excitation of the PBDTTT-EF-T component at 500 nm (excitation fraction is 78%) and N2200 component at 400 nm (excitation fraction is 72%). The PL quenching efficiencies of PBDTTT-EF-T and N2200 were  $> 99\%$  and  $86\%$ , respectively, for the blended film of PBDTTT-EF-T/N2200. The efficient PL quenching of both donor and acceptor polymers is consistent with the efficient charge-carrier generation as mentioned above, suggesting that charge-carriers are generated with minimal loss of absorbed photons in the PBDTTT-EF-T/N2200 BHJ solar cell. Figure 6-4 shows the atomic force microscopy (AFM) topographical and phase images ( $1 \mu\text{m} \times 1 \mu\text{m}$ ) of the PBDTTT-EF-T/N2200 blended film: no distinct phase-separated domain structures were observed. The fine surface morphology is consistent with the efficient PL quenching of both PBDTTT-EF-T and N2200, which implies that the donor and acceptor polymers are mixed on the nanometer scale. The author therefore concludes that efficient charge-carrier generation following light absorption is one of the key contributors to the large EQE observed for the PBDTTT-EF-T/N2200 BHJ solar cell.

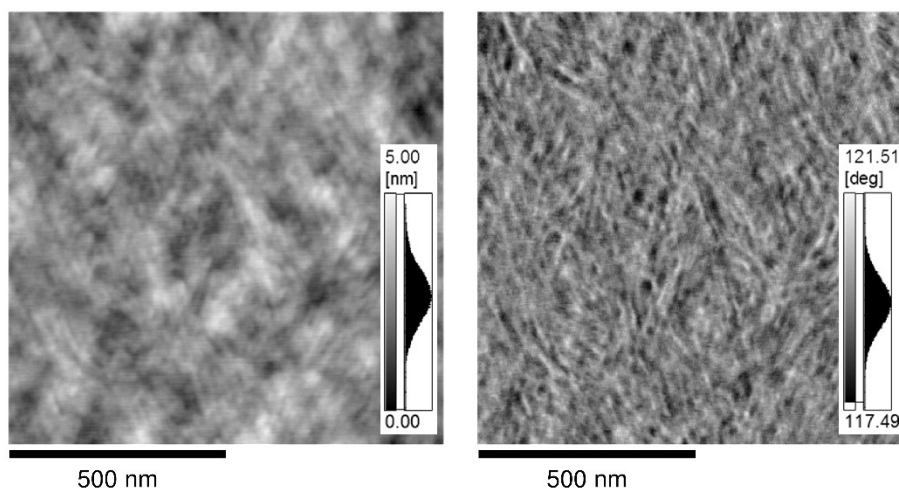


**Figure 6-4.** Tapping-mode AFM topographical (left) and phase (right) images ( $1 \mu\text{m} \times 1 \mu\text{m}$ ) of a PBDTTT-EF-T/N2200 blended film. The scale bar corresponds to a length of  $0.5 \mu\text{m}$ . The film was spin-coated from a chlorobenzene solution onto a glass substrate.

Next, the author discusses charge transport under short-circuit condition. From the ratio of  $J_{\text{SC}}$  to  $J_{\text{ph,sat}}$ , the charge collection efficiency was estimated to be as high as 79% under the short-circuit condition. Moreover, as shown in Figure 6-5a, the charge collection efficiency ( $J_{\text{SC}}/J_{\text{ph,sat}}$ ) was almost nondependent on the illumination intensities ranging from  $0.32$  to  $100 \text{ mW cm}^{-2}$ . If charge transport under the short-circuit condition suffers from bimolecular recombination, the increased charge-carrier density with light intensity should increase the magnitude of bimolecular recombination rates and thus decrease the  $J_{\text{SC}}/J_{\text{ph,sat}}$  ratio. Therefore, the nondependence of  $J_{\text{SC}}/J_{\text{ph,sat}}$  on illumination intensity suggests that bimolecular recombination is not dominant under the short-circuit condition. The 21% loss in  $J_{\text{ph}}$  might be due to geminate recombination of charge carriers. To further confirm this, the author measured the illumination intensity dependence of  $J_{\text{SC}}$ . As shown in Figure 6-5b,  $J_{\text{SC}}$  followed a power-law dependence  $J_{\text{SC}} \propto P_{\text{light}}^S$  with a slope  $S$  of 0.96 for the entire range of illumination intensities ( $P_{\text{light}}$ ). The value of the slope being close to unity is also

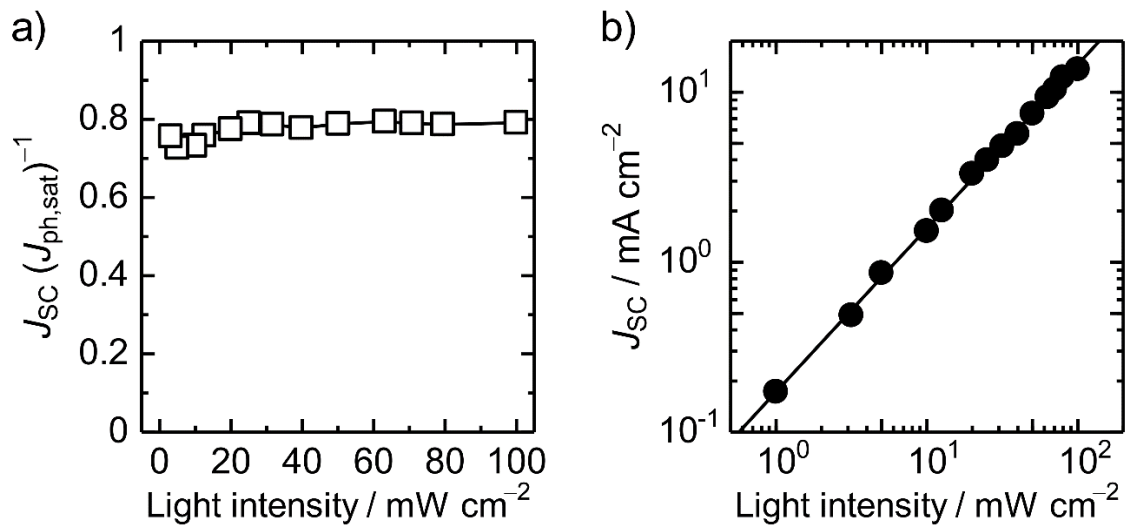


**Figure 6-5.** (a) Charge transport efficiencies under short-circuit condition ( $J_{SC}/J_{ph,sat}$ ) obtained by varying incident light intensities ranging from 100 to 0.32  $\text{mW cm}^{-2}$ ;  $J_{ph,sat}$  is the reverse saturation photocurrent density. (b) Incident light intensity ( $P_{light}$ ) dependence of  $J_{SC}$ . The data were fitted by a solid line according to  $J_{SC} \propto P_{light}^S$  with a slope  $S$  of 0.96;  $S$  was given by a least-squares fit over the entire range of light intensities.

indicative of negligible bimolecular recombination.<sup>32–36</sup> These results demonstrate that photogenerated charge carriers in the device are efficiently transported to the electrodes prior to bimolecular recombination under short-circuit condition. Thus, the author concludes that efficient charge collection is another key contributor to the large EQE observed for the PBDTTT-EF-T/N2200 BHJ solar cell. Here, the author notes that the loss in  $J_{ph}$  was 42% at the maximum power point, indicating that bimolecular recombination is not negligible at the low electric fields.

Finally, the author focuses on the charge-carrier mobility in the active layer, because the charge collection efficiency is determined by the competition between carrier sweep-out, which is limited by the charge-carrier mobility, and bimolecular recombination loss. The author measured the hole mobility  $\mu_h$  and the electron mobility  $\mu_e$  in both the neat and

blended films using the space-charge-limited current (SCLC) method with the Mott–Gurney equation (see Appendix, Figure 6-A3-1 and 6-A3-2).<sup>37,38</sup> The PBDTTT-EF-T neat film exhibited a hole mobility of  $\mu_h = 9.6 \times 10^{-4} \text{ cm}^2 \text{ V}^{-1} \text{ s}^{-1}$ . The N2200 neat film exhibited an electron mobility of  $\mu_e = 4.1 \times 10^{-3} \text{ cm}^2 \text{ V}^{-1} \text{ s}^{-1}$ . In the PBDTTT-EF-T/N2200 blended film,  $\mu_h$  and  $\mu_e$  were evaluated to be  $3.4 \times 10^{-4}$  and  $3.6 \times 10^{-4} \text{ cm}^2 \text{ V}^{-1} \text{ s}^{-1}$ , respectively. The high charge-carrier mobility on the order of  $10^{-4} \text{ cm}^2 \text{ V}^{-1} \text{ s}^{-1}$  in the blended film can reduce the carrier sweep-out time and hence improve the charge collection under the short-circuit condition. In addition, the SCLC measurements show that the hole mobility of the PBDTTT-EF-T/N2200 blended film is similar to the electron mobility. In other words, a balanced charge transport between hole and electron can be achieved in the PBDTTT-EF-T/N2200 device. A balanced charge-carrier transport is important for the improvement in FF because it would reduce the build-up of space-charges.<sup>39,40</sup> It is known that the space-charge-limited photocurrent shows a square root power dependence on voltage, and thus, limits the maximum FF to only 0.42.<sup>39,40</sup> In Figure 6-6, the  $J_{\text{ph}}$  of the PBDTTT-EF-T/N2200 BHJ solar cell was plotted against the effective applied voltage ( $V_0 - V$ ), where  $V_0$  is the compensation voltage at which  $J_{\text{ph}}$  is zero. Apparently, the  $J_{\text{ph}}$  was free from space-charge effects discriminated by  $J_{\text{ph}} \propto (V_0 - V)^{1/2}$ , as depicted by the broken line in Figure 6-6.<sup>39,40</sup> The author therefore concludes that the high and balanced charge-carrier mobility on the order of  $10^{-4} \text{ cm}^2 \text{ V}^{-1} \text{ s}^{-1}$  not only reduces the carrier sweep-out time under short circuit condition, but also suppresses the build-up of space-charges in the device, leading to improvements in EQE and FF, and consequently PCE. A fill factor of 0.47 was obtained even for the 150-nm-thick active layer (see Appendix, Figure 6-A5). This value is still higher than 0.42, indicating that charge carriers are collected at the electrodes without the space-charge limit even in the thick active layer.

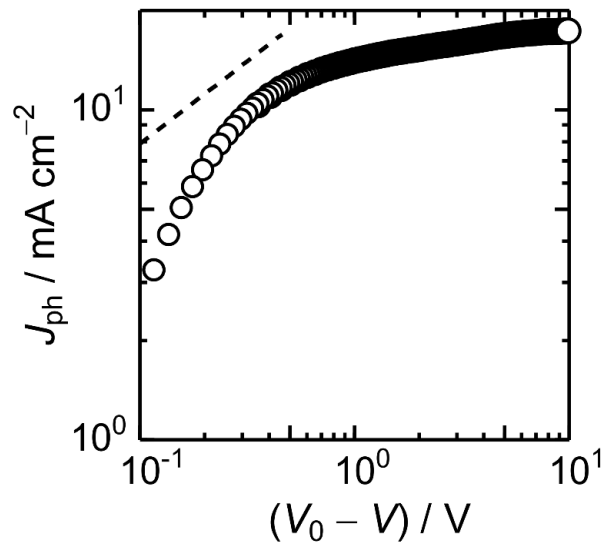


**Figure 6-6.** Photocurrent density  $J_{\text{ph}}$  of the PBDTTT-EF-T/N2200 BHJ solar cell plotted against the effective applied voltage  $(V_0 - V)$  under AM 1.5G illumination at  $100 \text{ mW cm}^{-2}$ ;  $V_0$  is the voltage at which  $J_{\text{ph}}$  is zero and  $V$  is the applied voltage. The broken line represents the square-root dependence of the  $J_{\text{ph}}$  on voltage.

### 6.3. Conclusions

The author has demonstrated that a PCE of 5.73% can be achieved even for polymer/polymer BHJ solar cells. This is mainly because the charge-carrier generation and collection efficiencies are both as high as  $\sim 80\%$ , which is comparable to those of efficient polymer/fullerene BHJ solar cells.<sup>1,3-5, 29</sup> This finding represents that polymer/polymer solar cells are not inherently inferior to polymer/fullerene solar cells, but rather that they have great potential as an alternative to polymer/fullerene solar cells. Recently, Polyera Corporation has announced achieving a PCE of 6.47%,<sup>8</sup> demonstrating that the potential for highly efficient polymer/polymer solar cells is not confined to this donor/acceptor polymer systems but rather versatile and achievable for other combinations of donor and acceptor polymers too. As shown in Figure 6-1b, both donor and acceptor polymers used in this study have a large absorption band from 550 to 800 nm and an “absorption window” from

400 to 550 nm at the same time. In other words, the device efficiency in this study is mainly limited by the weak absorptivity in the visible range rather than by charge-carrier generation and collection. Such absorption loss can be overcome by using donor and acceptor polymers with complementary absorption bands. If the complementary absorption spectrum ranges from 350 to 800 nm, we can achieve a  $J_{SC}$  value of  $16 \text{ mA cm}^{-2}$  even with an EQE of 60%. Moreover, using a wider HOMO–LUMO bandgap acceptor polymer with a LUMO energy level larger than that of N2200 by more than 0.2 eV (or a donor polymer with a HOMO energy level smaller (deeper) than that of PBDTTT-EF-T by more than 0.2 eV) will allow the  $V_{OC}$  to rise above 1 V. Consequently, a PCE of 8% should be achievable. In addition, the author notes that the device shown in this study is fabricated by simply spin-coating an active layer onto a normal ITO/PEDOT:PSS electrode. Processing approaches such as using solvent additives<sup>5,41,42</sup> and novel interfacial layers combined with an inverted device structure,<sup>1,43</sup> will further increase the PCE. The author, therefore, believes that the PCEs of polymer/polymer blend solar cells can be further improved up to 9%, as in the case of state-of-the-art polymer/fullerene solar cells.

#### 6.4. Experimental

*Materials:* The polymers PBDTTT-EF-T and N2200 were obtained from 1-Material Inc. and Polyera Corporation, respectively, and used as received. The weight-average molecular weight  $M_w$ , and polydispersity index (PDI; given by  $M_w/M_n$ , where  $M_n$  is the number-average molecular weight) of PBDTTT-EF-T as provided on the Certificate of Analysis were  $115,000 \text{ g mol}^{-1}$  and 2.5, respectively. Those of N2200 were  $178,000 \text{ g mol}^{-1}$  and 3.7, respectively. The  $M_w$  and PDI of N2200 were measured by size-exclusion chromatography (Shodex, GPC-101) using *o*-dichlorobenzene as the eluent, which was calibrated against monodisperse polystyrene standards (Shodex, STANDARD S-Series). The HOMO levels

of the PBDTTT-EF-T and N2200 neat films were evaluated by photoelectron yield spectroscopy (Riken Keiki, AC-3). To evaluate their accurate HOMO levels, the bottom sides of their neat films were measured. Their LUMO levels were determined by adding the optical bandgap energy ( $E_g$ ) calculated from the 0-0 transition to the HOMO energy:  $E_g$  was calculated as 1.68 eV (PBDTTT-EF-T) and 1.55 eV (N2200) by using  $E_g = hc/\lambda_{0-0}$ , where  $h$  is the Planck's constant,  $c$  is the velocity of light, and  $\lambda_{0-0}$  is the wavelength of the crossing point between the absorption and PL bands of the neat films (see Appendix, Figure 6-A6).

*Device Fabrication and Measurements:* ITO-coated glass substrates (10  $\Omega$  per square) were washed by ultrasonication with toluene, then acetone, and finally ethanol for 15 min each and then dried under an  $N_2$  flow. The washed substrates were further treated with a UV- $O_3$  cleaner (Nippon Laser & Electronics Lab, NL-UV253S) for 30 min. A 40-nm-thick layer of PEDOT:PSS (H. C. Stark, PH-500) was spin-coated onto the ITO substrate at a spinning rate of 3000 rpm for 99 s and then dried in air at 140  $^{\circ}C$  for 10 min. A blended layer of PBDTTT-EF-T/N2200 was spin-coated onto the PEDOT:PSS film at 2500 rpm for 60 s from CB solution. The blended solution was prepared by mixing PBDTTT-EF-T and N2200 in a 1:1 weight ratio in CB: PBDTTT-EF-T (9 mg) and N2200 (9 mg) were dissolved in 1 mL of CB. The thickness of the PBDTTT-EF-T/N2200 blended layers was  $100 \pm 10$  nm. Preparation of the CB solutions and subsequent spin coating of the solutions onto the PEDOT:PSS film was carried out in an  $N_2$ -filled glove box. After the spin coating, the PBDTTT-EF-T/N2200 blended films were stored in an  $N_2$ -filled glove box for one week at room temperature. Finally, a calcium interlayer (Ca, 2 nm) and an aluminum electrode (Al, 70 nm) were vacuum-deposited through a shadow mask at  $2.5 \times 10^{-4}$  Pa. The  $J$ - $V$  characteristics of the devices were measured using a direct-current voltage and current source/monitor (Advantest, R6243) under illumination by an "air mass 1.5-Global" (AM

1.5G) simulated solar light at  $100 \text{ mW cm}^{-2}$ . The light intensity was corrected with a calibrated silicon photodiode reference cell (Bunko-Keiki, BS-520; active area:  $0.0534 \text{ cm}^2$ ). The spectral-mismatch factor calculated with respect to the AM 1.5G spectrum for the PBDTTT-EF-T/N2200 test-cell and BS-520 silicon reference-cell combination was 1.02.<sup>44</sup> The illumination intensity dependence of the  $J$ - $V$  characteristics was performed by using reflective neutral density (ND) filters with optical densities (OD) from 0.1 to 1.5. The EQE spectrum was measured with a digital electrometer (Advantest, R8252) under illumination of monochromatic light from a 500-W Xe lamp (Thermo Oriel, 66921) with optical cut filters and a monochromator (Thermo Oriel, UV-visible Cornerstone). The active area of the device was  $0.07 \text{ cm}^2$ , which was determined from the area of the top Ca/Al electrode. To minimize the *edge effect*, the author used a device layout consisting of unpatterned PEDOT:PSS and PBDTTT-EF-T/N2200 layers sandwiched between unpatterned ITO and Ca/Al top electrodes. In this layout, the photoactive area can be assumed to be the area of the Ca/Al top electrode.<sup>45</sup> Simulated solar light was illuminated on the ITO side of the device. All measurements were carried out under an atmosphere of  $\text{N}_2$  at room temperature. The device structure is depicted in Appendix, Figure 6-A7. More than 25 devices were fabricated to ensure the reproducibility of the  $J$ - $V$  characteristics.

*Mobility Measurements:* Hole-only devices were fabricated by the following procedure. A PBDTTT-EF-T neat layer and PBDTTT-EF-T/N2200 blended layer were spin-coated onto separate ITO substrates covered with 40-nm-thick PEDOT:PSS, which acted as the anode. A gold electrode (Au, 50 nm) was then vacuum-deposited on each layer as the cathode (ITO|PEDOT:PSS|PBDTTT-EF-T|Au and ITO|PEDOT:PSS|PBDTTT-EF-T/N2200|Au). Thicknesses of the PBDTTT-EF-T neat layer and PBDTTT-EF-T/N2200 blended layer were 123 nm and 82 nm, respectively. Electron-only devices were fabricated by the following procedure. A 50-nm-thick Al layer, which acted as the anode, was vacuum-deposited on a

glass substrate covered with 20-nm-thick poly(sodium 4-styrenesulfonate) ( $M_w = 70,000 \text{ g mol}^{-1}$ ). A neat layer of N2200 and PBDTTT-EF-T/N2200 blended layer were spin-coated onto each Al electrode. A  $\text{Cs}_2\text{CO}_3$  interlayer (4 nm) and Al layer (80 nm) were then vacuum-deposited as the cathode ( $\text{Al}|\text{N2200}|\text{Cs}_2\text{CO}_3|\text{Al}$  and  $\text{Al}|\text{PBDTTT-EF-T/N2200}|\text{Cs}_2\text{CO}_3|\text{Al}$ ). Thicknesses of the N2200 neat layer and PBDTTT-EF-T/N2200 blended layer were 145 nm and 95 nm, respectively. The  $\text{Cs}_2\text{CO}_3$  layer was used to enhance the efficiency of electron injection.<sup>46</sup> The dark  $J$ - $V$  characteristics of the devices were measured in air (hole-only devices) and under an  $\text{N}_2$  atmosphere (electron-only devices) by using a direct-current voltage and current source/monitor (Advantest, R6243). The PBDTTT-EF-T and N2200 neat layers were spin-coated from CB solutions. The PBDTTT-EF-T/N2200 blended layer was spin-coated under the same conditions used for device fabrication.

*Photoluminescence Quenching Measurements:* PL spectra were measured for the PBDTTT-EF-T and N2200 neat films and PBDTTT-EF-T/N2200 blended film, which were spin-coated onto quartz substrates, using a calibrated fluorescence spectrophotometer (Horiba, NanoLog). The sample films were excited at 500 nm to primarily excite the PBDTTT-EF-T component and at 400 nm to mainly excite the N2200 component. The excitation fraction of each component was 78% (PBDTTT-EF-T) and 72% (N2200). The PL quenching efficiency of PBDTTT-EF-T was evaluated from the ratio of PBDTTT-EF-T PL intensity for the PBDTTT-EF-T/N2200 blended films to that for a PBDTTT-EF-T neat film (after each PL intensity was corrected for variations in PBDTTT-EF-T absorption at 500 nm). The PL quenching efficiency of N2200 was evaluated from the ratio of N2200 PL intensity for the PBDTTT-EF-T/N2200 blended films to that for an N2200 neat film (after each PL intensity was corrected for variations in N2200 absorption at 400 nm).

*Reflection Absorption Measurements:* Absorbance was measured in reflection geometry at an incident angle of  $5^\circ$  normal to the substrate (Hitachi, U-4100) for the PBDTTT-EF-T/N2200 blended films covered with an Al top electrode. A schematic of the film structure used in reflection absorbance measurements is depicted in the inset of Figure 6-A2 in Appendix. The blended film was spin-coated from CB solution onto a glass substrate under the same conditions used for device fabrication. The reflection absorption of the PBDTTT-EF-T/N2200 blended films was calculated from the reflection absorbance ( $Abs(\lambda)$ ) as  $(1-10^{-Abs(\lambda)}) \times 100$ .

*AFM Measurements:* Surface morphology of the PBDTTT-EF-T/N2200 blended film was observed by Atomic Force Microscopy (AFM, Simadzu, SPM-9600). Silicon probes were used with a resonant frequency of  $\sim 267$  kHz and a force constant of  $\sim 42$  N m $^{-1}$  (NANO WORLD, NCHR-10).

## 6.5. Appendix

### 6.5.1. Device Parameters

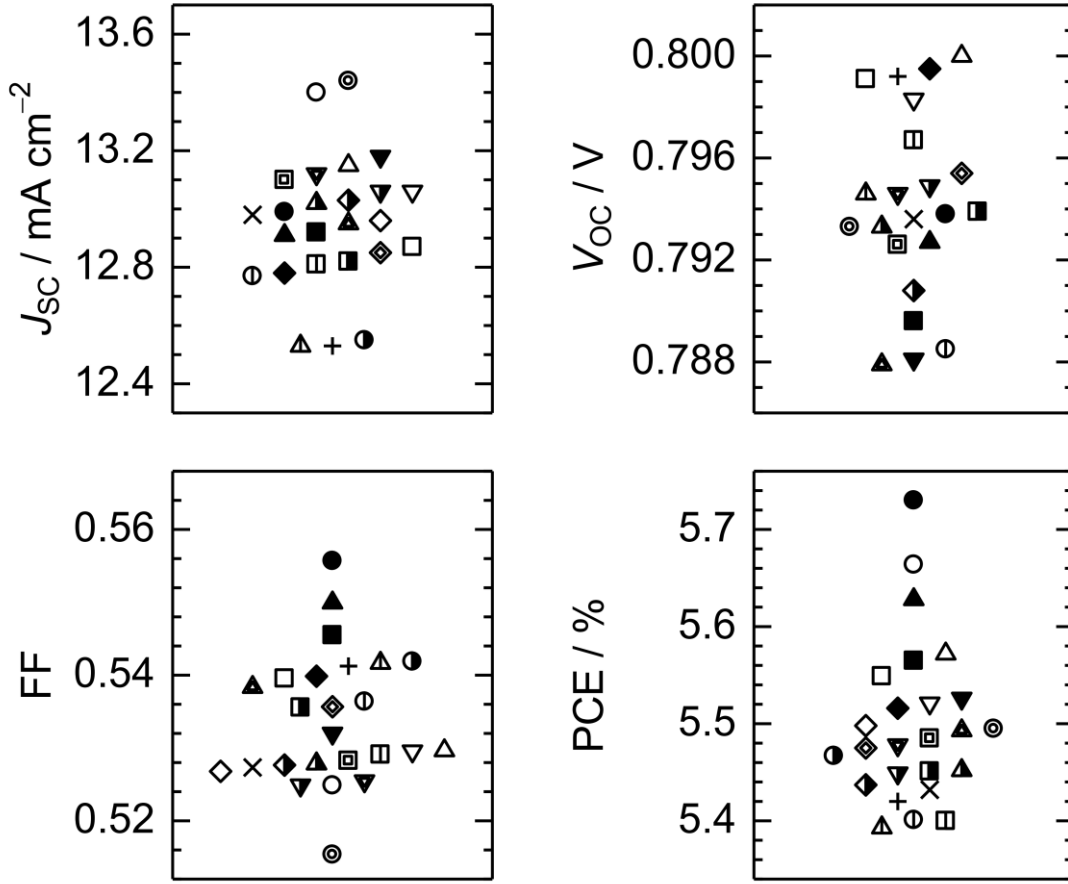


**Figure 6-A1.** Distributions of  $J_{SC}$ , FF, PCE, and  $V_{OC}$  of PBDTTT-EF-T/N2200 BHJ solar cells. Circles of the same symbols in each figure represent the parameters obtained from the same device.

### 6.5.2. The Number of Photons Absorbed by the PBDTTT-EF-T/N2200 Layer

The number of photons absorbed by the PBDTTT-EF-T/N2200 blended film ( $N_{ph}$ ) was calculated using the following equation:

$$N_{ph} = \int_{350 \text{ nm}}^{900 \text{ nm}} \frac{N_{AM1.5G}(\lambda) \cdot \%Abs(\lambda) \cdot d\lambda}{100} \quad (\text{A1})$$

In Equation A1,  $N_{AM1.5G}$  is the number of photons from AM 1.5G solar light,  $\%Abs$  is the percentage absorption of the PBDTTT-EF-T/N2200 blended film, and  $\lambda$  is the wavelength.

The value of  $\%Abs$  was calculated from the absorbance (Abs) of the blended film as  $\%Abs(\lambda)$

$= (1 - 10^{-Abs(\lambda)}) \times 100$ . The absorbance was measured in reflection geometry at an incident angle of  $5^\circ$  normal to the substrate (Hitachi, U-4100) for the blended film covered with an Al top electrode. Figure 6-A2 shows the reflection absorbance of the blended film used for the calculation of %Abs. The blended film was spin-coated from CB solution onto a glass substrate under the same conditions used for device fabrication.

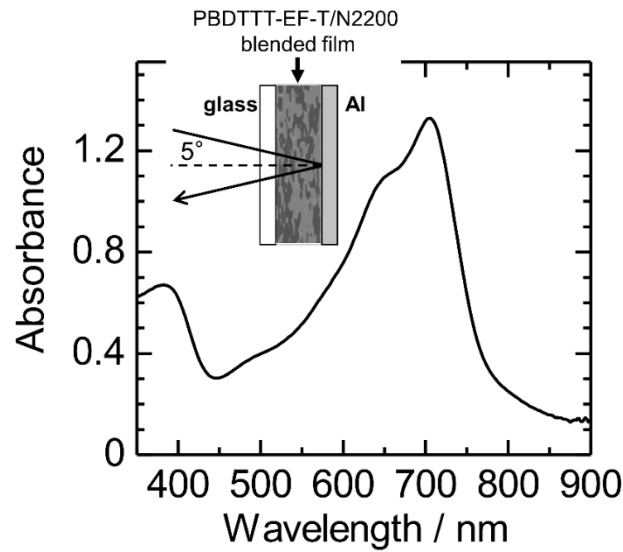


**Figure 6-A2.** Reflection absorbance spectrum of the PBDTTT-EF-T/N2200 blended film. The inset shows a schematic of the film structure used in the reflection absorbance measurement.

### 6.5.3. Mobility Measurements

Charge-carrier mobilities ( $\mu$ ) were calculated from the dark  $J$ - $V$  characteristics using the space-charge-limited current (SCLC) method using the Mott–Gurney equation for current density  $J_{SCLC}$ , expressed as  $J_{SCLC} = \frac{9}{8} \epsilon_0 \epsilon_r \mu \frac{V^2}{L^3}$ , where  $\epsilon_0$  is the vacuum permittivity,  $\epsilon_r$  is the dielectric constant of the film ( $\epsilon_r = 3$  was assumed), and  $L$  is the thickness of the active layer.<sup>37,38</sup> The  $J$ - $V$  characteristics of the hole-only devices and those of the electron-only devices are shown in Figures 6-A3-1 and 6-A3-2, respectively.

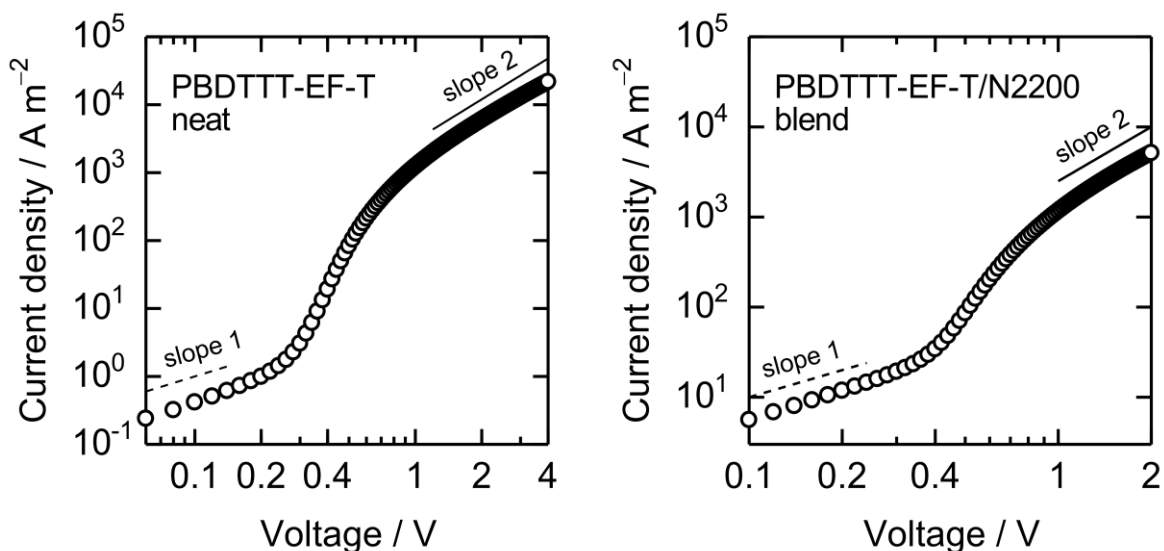


**Figure 6-A3-1.** The dark  $J$ - $V$  characteristics of ITO|PEDOT:PSS|PBDTTT-EF-T(123 nm)|Au and ITO|PEDOT:PSS|PBDTTT-EF-T/N2200(82 nm)|Au hole-only devices.

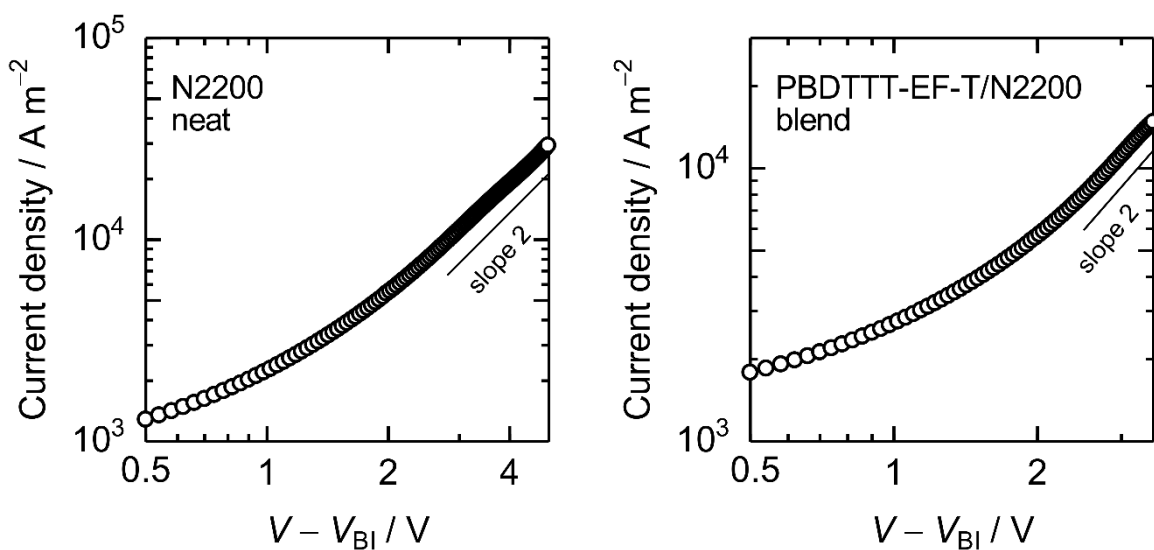


**Figure 6-A3-2.** The dark  $J$ - $V$  characteristics of Al|N2200(145 nm)|Cs<sub>2</sub>CO<sub>3</sub>/Al and Al|PBDTTT-EF-T/N2200(95 nm)|Cs<sub>2</sub>CO<sub>3</sub>/Al electron-only devices. The applied voltage  $V$  was corrected for the built-in voltage  $V_{BI}$  of 2.1 V.<sup>A1,A2</sup>

#### 6.5.4. Dependence of Charge-Carrier Mobilities on Film Thickness

Charge-carrier mobilities in the PBDTTT-EF-T/N2200 blended film calculated by considering the voltage drop due to contact resistance (the resistance of these single-carrier devices was assumed to be  $10 \Omega^{A3,26}$ ) are  $\mu_h = 4.1 \times 10^{-4} \text{ cm}^2 \text{ V}^{-1} \text{ s}^{-1}$  and  $\mu_e = 4.8 \times 10^{-4} \text{ cm}^2 \text{ V}^{-1} \text{ s}^{-1}$ , respectively

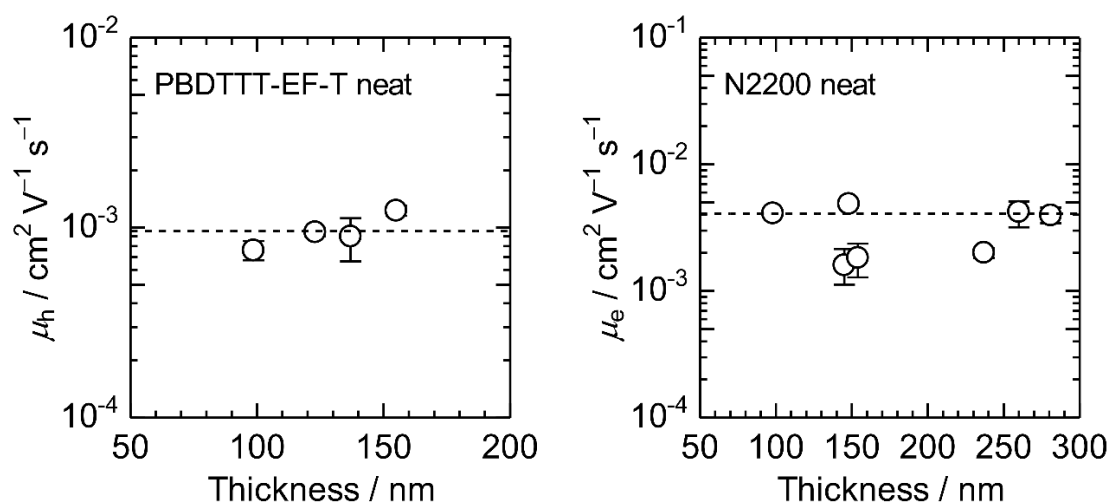


**Figure 6-A4.** Hole ( $\mu_h$ ) and electron ( $\mu_e$ ) mobilities of PBDTTT-EF-T and N2200 neat films evaluated for different film thickness.

#### 6.5.5. Dependence of FF on Active Layer Thickness

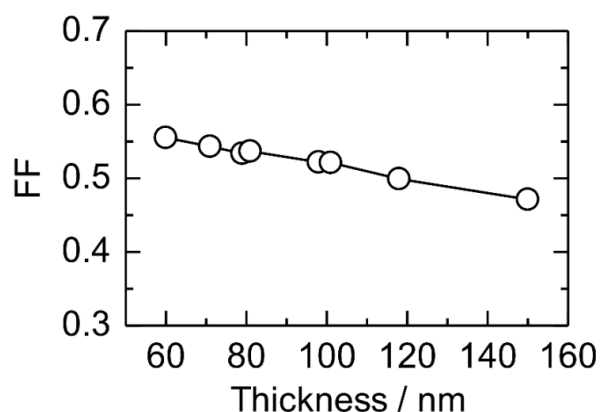


**Figure 6-A5.** Fill factor of PBDTTT-EF-T/N2200 BHJ solar cells with varying thicknesses ranging from 60 nm to 150 nm under AM 1.5G illumination ( $100 \text{ mW cm}^{-2}$ ).

### 6.5.6. Calculation of Optical Bandgap Energy ( $E_g$ )

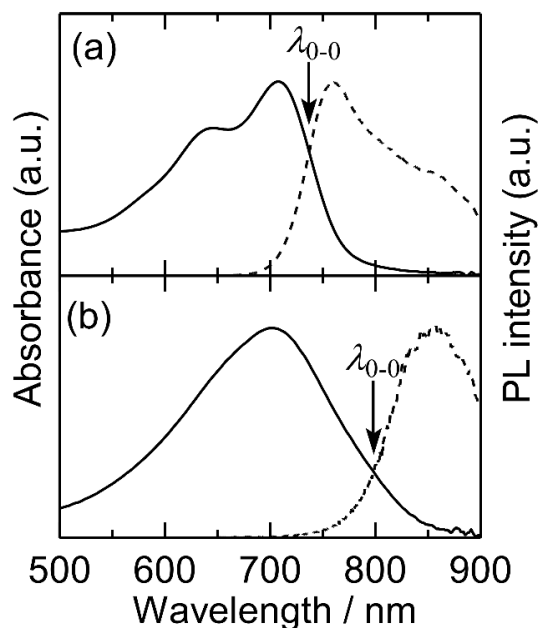


**Figure 6-A6.** Absorbance (solid line) and PL (dashed line) spectra of (a) PBDTTT-EF-T and (b) N2200 neat films spin-coated from chlorobenzene solution. The optical bandgap energy ( $E_g$ ) was calculated from the 0-0 transition using  $E_g = hc/\lambda_{0-0}$ , where  $h$  is the Planck's constant,  $c$  is the velocity of light, and  $\lambda_{0-0}$  is the wavelength of the crossing point between the absorption and PL bands.

### 6.5.7. Device Structure

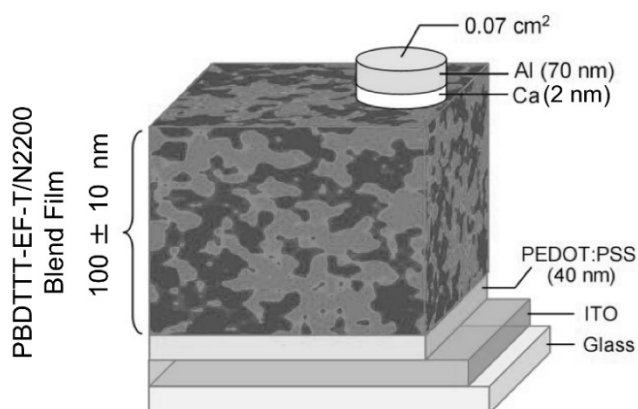


**Figure 6-A7.** Schematic illustration of the device structure.

## 6.6. References and Note

- [1] Z. He, C. Zhong, S. Su, M. Xu, H. Wu, Y. Cao, *Nat. Photon.* **2012**, *6*, 591–595.
- [2] M. A. Green, K. Emery, Y. Hishikawa, W. Warta, E. D. Dunlop, *Prog. Photovolt: Res. Appl.* **2014**, *22*, 1–9.
- [3] L. Bian, E. Zhu, J. Tang, W. Tang, F. Zhang, *Prog. Polym. Sci.* **2012**, *37*, 1292–1331.
- [4] C. J. Brabec, S. Gowrisanker, J. J. M. Halls, D. Laird, S. Jia, S. P. Williams, *Adv. Mater.* **2010**, *22*, 3839–3856.
- [5] Y. W. Su, S. C. Lan, K. H. Wei, *Mater. Today* **2012**, *15*, 554–562.
- [6] Y. Li, *Acc. Chem. Res.* **2012**, *45*, 723–733.
- [7] Z. Ma, W. Sun, S. Himmelberger, K. Vandewal, Z. Tang, J. Bergqvist, A. Salleo, J. W. Andreasen, O. Inganäs, M. R. Andersson, C. Müller, F. Zhang, E. Wang, *Energy Environ. Sci.* **2014**, *7*, 361–369.
- [8] A. Facchetti, *Mater. Today* **2013**, *16*, 123–132.
- [9] E. Zhou, J. Cong, Q. Wei, K. Tajima, C. Yang, K. Hashimoto, *Angew. Chem. Int. Ed.* **2011**, *50*, 2799–2803.
- [10] See Chapter 2.
- [11] See Chapter 4.
- [12] S. Ito, T. Hirata, D. Mori, H. Benten, L. T. Lee, H. Ohkita *J. Photopolym. Sci. Technol.* **2013**, *26*, 175–180.
- [13] T. Earmme, Y. J. Hwang, N. M. Murari, S. Subramaniyan, S. A. Jenekhe, *J. Am. Chem. Soc.* **2013**, *135*, 14960–14963.
- [14] Y. Zhou, Q. Yan, Y. Q. Zheng, J. Y. Wang, D. Zhao, J. Pei, *J. Mater. Chem. A* **2013**, *1*, 6609–6613.
- [15] P. Cheng, L. Ye, X. Zhao, J. Hou, Y. Li, X. Zhan, *Energy Environ. Sci.* **2014**, *7*, 1351–1356.

- [16] E. Zhou, J. Cong, K. Hashimoto, K. Tajima, *Adv. Mater.* **2013**, *25*, 6991–6996.
- [17] N. Zhou, H. Lin, S. J. Lou, X. Yu, P. Guo, E. F. Manley, S. Loser, P. Hartnett, H. Huang, M. R. Wasielewski, L. X. Chen, R. P. H. Chang, A. Facchetti, T. J. Marks, *Adv. Energy Mater.* **2014**, *4*, 1300785.
- [18] See Chapter 5.
- [19] Y. Zhou, T. Kurosawa, W. Ma, Y. Guo, L. Fang, K. Vandewal, Y. Diao, C. Wang, Q. Yan, J. Reinspach, J. Mei, A. L. Appleton, G. I. Koleilat, Y. Gao, S. C. B. Mannsfeld, A. Salleo, H. Ade, D. Zhao, Z. Bao, *Adv. Mater.* **2014**, *26*, 3767–3772.
- [20] M. M. Mandoc, W. Veurman, L. J. A. Koster, B. Boer, P. W. M. Blom, *Adv. Funct. Mater.* **2007**, *17*, 2167–2173.
- [21] Y. Kim, S. Cook, S. A. Choulis, J. Nelson, J. R. Durrant, D. D. C. Bradley, *Chem. Mater.* **2004**, *16*, 4812–4818.
- [22] M. M. Mandoc, W. Veurman, L. J. A. Koster, M. M. Koetse, J. Sweelssen, B. Boer, P. W. M. Blom, *J. Appl. Phys.* **2007**, *101*, 104512.
- [23] H. Yan, Z. Chen, Y. Zheng, C. Newman, J. R. Quinn, F. Dötz, M. Kastler, A. Facchetti, *Nature* **2009**, *457*, 679–687.
- [24] Y. Liang, D. Feng, Y. Wu, S. T. Tsai, G. Li, C. Ray, L. Yu, *J. Am. Chem. Soc.* **2009**, *131*, 7792–7799.
- [25] H. Y. Chen, J. Hou, S. Zhang, Y. Liang, G. Yang, Y. Yang, L. Yu, Y. Wu, G. Li, *Nat. Photon.* **2009**, *3*, 649–653.
- [26] Y. Liang, Z. Xu, J. Xia, S. T. Tsai, Y. Wu, G. Li, C. Ray, L. Yu, *Adv. Mater.* **2010**, *22*, E135–E138.
- [27] L. Huo, S. Zhang, X. Guo, F. Xu, Y. Li, J. Hou, *Angew. Chem. Int. Ed.* **2011**, *50*, 9697–9702.
- [28] S. H. Liao, H. J. Jhuo, Y. S. Cheng, S. A. Chen, *Adv. Mater.* **2013**, *25*, 4766–4771.

- [29] G. Dennler, M. C. Scharber, C. J. Brabec, *Adv. Mater.* **2009**, *21*, 1323–1338.
- [30] V. D. Mihailetschi, L. J. A. Koster, P. W. M. Blom, C. Melzer, B. Boer, J. K. J. Duren, R. A. J. Janssen, *Adv. Funct. Mater.* **2005**, *15*, 795–801.
- [31] V. D. Mihailetschi, H. Xie, B. Boer, L. J. A. Koster, P. W. M. Blom, *Adv. Funct. Mater.* **2006**, *16*, 699–708.
- [32] P. Schilinsky, C. Waldauf, C. J. Brabec, *Appl. Phys. Lett.* **2002**, *81*, 3885.
- [33] J. Nelson, *Phys. Rev. B* **2003**, *67*, 155209.
- [34] D. Gebeyehu, M. Pfeiffer, B. Maennig, J. Drechsel, A. Werner, L. Leo, *Thin Solid Films*, **2004**, *451–452*, 29–32.
- [35] I. Riedel, J. Parisi, V. Dyakonov, L. Lutsen, D. Vanderzande, J. C. Hummelen, *Adv. Funct. Mater.* **2004**, *14*, 38–44.
- [36] A. K. K. Kyaw, D. H. Wang, V. Gupta, W. L. Leong, L. Ke, G. C. Bazan, A. J. Heeger, *ACS Nano* **2013**, *7*, 4569–4577.
- [37] G. G. Malliaras, J. R. Salem, P. J. Brock, C. Scott, *Phys. Rev. B* **1998**, *58*, R13411–R13414.
- [38] Y. Shen, A. R. Hosseini, M. H. Wong, G. G. Malliaras, *ChemPhysChem* **2004**, *5*, 16–25.
- [39] V. D. Mihailetschi, J. Wildeman and P. W. M. Blom, *Phys. Rev. Lett.* **2005**, *94*, 126602.
- [40] L. J. A. Koster, V. D. Mihailetschi, M. Lenes, P. W. M. Blom, in *Organic Photovoltaics: Materials, Device Physics, and Manufacturing Technologies*, (Eds.: Brabec, C.; Dyakonov, V.; Scherf, U.) Wiley-VCH, Weinheim, Germany **2008**, pp. 283–297.
- [41] H. C. Liao, C. C. Ho, C. Y. Chang, M. H. Jao, S. B. Darling, W. F. Su, *Mater. Today* **2013**, *16*, 326–336.
- [42] Y. Kim, H. R. Yeom, J. Y. Kim and C. Yang, *Energy Environ. Sci.*, **2013**, *6*, 1909–

- 1916.
- [43] Z. He, C. Zhong, X. Huang, W. Y. Wong, H. Wu, L. Chen, S. Su and Y. Cao, *Adv. Mater.* **2011**, *23*, 4636–4643.
- [44] V. Shrotriya, G. Li, Y. Yao, T. Moriarty, K. Emery, Y. Yang, *Adv. Funct. Mater.* **2006**, *16*, 2016–2023.
- [45] A. Cravino, P. Schilinsky, C. J. Brabec, *Adv. Funct. Mater.* **2007**, *17*, 3906–3910.
- [46] G. J. A. H. Wetzelaer, M. Kuik, Y. Olivier, V. Lemaire, J. Cornil, S. Fabiano, M. A. Loi, P. W. M. Blom, *Phys. Rev. B* **2012**, *86*, 165203.
- [A1] The  $V_{BI}$  was estimated from the difference in the work functions between Al anode (4.3 eV) and  $Cs_2CO_3/Al$  cathode (2.2 eV).<sup>A2</sup>
- [A2] J. Huang, Z. Xu, Y. Yang, *Adv. Funct. Mater.* **2007**, *17*, 1966–1973.
- [A3] S. M. Tuladhar, D. Poplavskyy, S. A. Choulis, J. R. Durrant, D. D. C. Bradley, J. Nelson, *Adv. Funct. Mater.* 2005, **15**, 1171–1182.



## Summary

In this thesis, the author describes the development of efficient polymer blend solar cells composed of conjugated donor and acceptor polymers, through both optimization of the nanoscale phase-separated structure of polymer/polymer blend films and an appropriate selection of donor and acceptor polymer materials. The origin of the improved device performances is also addressed. The first part of this thesis is concerned with the optimization of blend nanomorphology and the correlation between morphology and photovoltaic performances. The latter part of the thesis focuses on the application of low-bandgap polymers to polymer/polymer blend solar cells in order to enhance their photovoltaic performances. A summary of each chapter is presented below.

In Chapter 2, the preparation of polymer/polymer blend solar cells consisting of poly(3-hexylthiophene) (P3HT) as the donor and poly[2,7-(9,9-didodecylfluorene)-*alt*-5,5-(4',7'-bis(2-thienyl)-2',1',3'-benzothiadiazole)] (PF12TBT) as the acceptor is reported. The author found that the photovoltaic performances of P3HT/PF12TBT solar cells varied drastically with changes in the processing solvents and annealing temperatures. The device prepared by spin coating using high-boiling point solvents, chlorobenzene and *o*-dichlorobenzene, exhibited a short-circuit current density ( $J_{SC}$ ) as low as  $1 \text{ mA cm}^{-2}$  due to the formation of phase-separated structures on the micro- and sub-micrometer scale during the slow evaporation of solvents. On the other hand, the device prepared from chloroform (a low-boiling point solvent) resulted in a higher  $J_{SC}$  as high as  $4 \text{ mA cm}^{-2}$  due to the presence of a finely mixed blend morphology comprising nanoscale phase-separated domains. In addition, thermal annealing was found to improve domain purity and subsequently promoted domain growth on a nanometer scale. As a result,  $J_{SC}$  increased due to low-temperature annealing but decreased due to high-temperature annealing. Thus, the author concludes

that efficient photovoltaic performances are achieved owing to thermal purification of nanoscale phase-separated domains, obtained from a low-boiling point solvent such as chloroform.

In Chapter 3, charge carrier generation and recombination dynamics in thermally-annealed P3HT/PF12TBT blend films are investigated using transient absorption spectroscopy. Charge carrier dynamics were found to vary depending on the annealing temperature. In the case of the unannealed blend film, the majority of charges were generated promptly within an excitation laser pulse (100 fs) without diffusion of singlet excitons. This indicates that donor and acceptor polymers are mixed on the scale of a few nanometers, which is shorter than the diffusion length of singlet excitons. In this case, most of the generated charges were constrained within the isolated polymer domains, and were found to recombine monomolecularly to the ground state with a lifetime of 2500 ps. Thermal annealing was observed to suppress the monomolecular recombination loss and to increase the efficiency of free carrier generation owing to both purification of the PF12TBT domains and crystallization of the P3HT chains. The author therefore concludes that photovoltaic performances are dominated by the generation efficiency of free charge carriers, which is significantly affected by the nanomorphology of blend films.

From the discussion in Chapters 2 and 3, the author found that an improvement in device performance is obtained with a blend morphology that can offer efficient free-carrier generation and transport by the thermal purification of nanoscale phase-separated domains without domain growth. In Chapter 4, based on these findings, a further improvement in performances is demonstrated using high-molecular-weight of the acceptor polymer, PF12TBT. The power conversion efficiency (PCE) increased from 1.9% to 2.7% as the weight average molecular weight of PF12TBT increased from 8,500 to 78,000. In the device with high-molecular-weight PF12TBT, efficient charge generation was maintained

even at high annealing temperatures. This is likely because high-molecular-weight PF12TBT has a relatively high  $T_g$ , and its chains exhibit reduced diffusional mobility, thus resulting in the suppression of domain growth during the thermal annealing of P3HT/PF12TBT blend films. Efficient charge transport was also achieved by the formation of interconnected networks of PF12TBT domains, and by the ordering of P3HT chains in P3HT domains by thermal annealing. Therefore, in the device with high-molecular-weight PF12TBT, optimum blend morphology that realizes efficient charge generation as well as charge transport by thermal annealing results in the improvement in device performance.

In Chapter 5, the use of low-bandgap polymers as both donor and acceptor materials to enhance the light-harvesting efficiencies in the near infrared region is examined. Low-bandgap polymer/polymer blend solar cells were prepared using poly[2,3-bis-(3-octyloxyphenyl)quinoxaline-5,8-diyl-*alt*-thiophene-2,5-diyl] (PTQ1) as the donor and poly{[*N,N'*-bis(2-octyldodecyl)-naphthalene-1,4,5,8-bis(dicarboximide)-2,6-diyl]-*alt*-5,5'-(2,2'-bithiophene)} (N2200) as the acceptor. Due to efficient light absorption by both PTQ1 and N2200, the solar cells consisting of a 50:50 blend of PTQ1:N2200 gave a PCE as high as 3.4%. Moreover, the device performance was further enhanced by the optimization of the PTQ1:N2200 blend ratio, with a maximum external quantum efficiency (EQE) of 50% and an excellent PCE of 4.1% being achieved for the device containing 70% PTQ1. To explain the origin of the superior device performance in the presence of a higher PTQ1 to N2200 ratio, charge generation and transport efficiencies were investigated for the blend films with different PTQ1 contents. Photoluminescence quenching measurements indicated that charge generation from PTQ1 excitons occurred more efficiently than that from N2200 excitons as the excitons in PTQ1 were effectively conveyed to the interface with N2200 *via* energy transfer. Furthermore, mobility measurements showed that hole mobilities in the

blend film improved and became more balanced with electron mobilities as the PTQ1 content increased. Consequently, the device performances were optimized at high PTQ1 contents.

In Chapter 6, the preparation of highly efficient polymer/polymer blend solar cells using poly[[4,8-bis[5-(2-ethylhexyl)thiophene-2-yl]benzo[1,2-b:4,5-b']dithiophene-2,6-diyl][3-fluoro-2-[(2-ethylhexyl)carbonyl]thieno[3,4-b]thiophenediyl]] (PBDTTT-EF-T) as the donor and N2200 as the acceptor is demonstrated. In this case, both the donor and acceptor are low-bandgap polymers with high charge carrier mobilities, resulting in an EQE approaching 60% and a PCE of 5.7%. The author found both charge-carrier generation and collection efficiencies to be as high as 80%, which is comparable to those of efficient polymer/fullerene blend solar cells. This is due to the finely mixed morphology on nanometer scale and high charge-carrier mobilities in blend films. This finding therefore demonstrates that the potential of polymer/polymer blend solar cells is comparable to that of polymer/fullerene solar cells.

## List of Publications

### Chapter 2.

***“Polymer/Polymer Blend Solar Cells with 2.0% Efficiency Developed by Thermal Purification of Nanoscale-Phase-Separated Morphology”***

Daisuke Mori, Hiroaki Benten, Junya Kosaka, Hideo Ohkita, Shinzaburo Ito, and Kunihiro Miyake

*ACS Applied Materials and Interfaces* **2011**, 3 (8), 2924–2927.

### Chapter 3.

***“Charge Generation and Recombination Dynamics in Efficient Polymer/Polymer Blend Solar Cells with Nanoscale-Phase-Separated Morphology”***

Daisuke Mori, Hiroaki Benten, Hideo Ohkita, and Shinzaburo Ito

Submitted to *Advanced Energy Materials*.

### Chapter 4.

***“Polymer/Polymer Blend Solar Cells Improved by High-Molecular-Weight Fluorene-Based Copolymer as Electron Acceptor”***

Daisuke Mori, Hiroaki Benten, Hideo Ohkita, Shinzaburo Ito, and Kunihiro Miyake

*ACS Applied Materials and Interfaces* **2012**, 4 (7), 3325–3329.

Chapter 5.

***“Low-Bandgap Donor/Acceptor Polymer Blend Solar Cells with Efficiency Exceeding 4%”***

Daisuke Mori, Hiroaki Benten, Izumi Okada, Hideo Ohkita, and Shinzaburo Ito  
*Advanced Energy Materials* **2014**, 4, 1301006.

Chapter 6.

***“Highly Efficient Charge-Carrier Generation and Collection in Polymer/Polymer Blend Solar Cells with a Power Conversion Efficiency of 5.7%”***

Daisuke Mori, Hiroaki Benten, Izumi Okada, Hideo Ohkita, and Shinzaburo Ito  
*Energy & Environmental Science* **2014**, 7, 2939–2943.

Others

***“Current Mode Atomic Force Microscopy (C-AFM) Study for Local Electrical Characterization of Conjugated Polymer Blends”***

Li-Ting Lee, Shinzaburo Ito, Hiroaki Benten, Hideo Ohkita, and Daisuke Mori

*AMBIO* **2012**, *41* (Supplement 2): 135–137.

***“Development of Polymer Blend Solar Cells Composed of Conjugated Donor and Acceptor Polymers”***

Shinzaburo Ito, Toshiaki Hirata, Daisuke Mori, Hiroaki Benten, Li-Ting Lee, and

Hideo Ohkita

*Journal of Photopolymer Science and Technology* **2013**, *26* (2), 175–180.

***“Near-Infrared Dye Sensitization of Polymer/Polymer Thin-Film Solar Cells”***

Shinzaburo Ito, Toshiaki Hirata, Daisuke Mori, Hiroaki Benten, and Hideo Ohkita

*Molecular Crystals and Liquid Crystals* **2013**, *578* (1), 19–25.



## *Acknowledgment*

The studies presented in this thesis have been carried out at Department of Polymer Chemistry, Graduate School of Engineering, Kyoto University, Japan, from April 2010 to March 2015, under the guidance of Professor Shinzaburo Ito. The author expresses his sincere gratitude to Professor Shinzaburo Ito for his kind guidance from a point of wide view, significant discussion, heartfelt advices throughout this work, and for giving the opportunity to study at his laboratory. The author is deeply grateful to Associate Professor Hideo Ohkita for his kind supports and valuable suggestions. The author would like to express his gratitude to Associate Professor Hiroyuki Aoki for his valuable advices from a different point of view. The author is also indebted to Assistant Professor Hiroaki Benten for his great deal of supports and valuable discussion throughout this work. Without his guidance this thesis would not have been possible.

Professor Kazuo Akagi, Department of Polymer Chemistry, Graduate School of Engineering, Kyoto University, and Professor Yoshinobu Tsujii, Institute for Chemical Research, Kyoto University, are especially acknowledged for their critical review of this thesis.

The author would like to thank Dr. Li-Ting Lee, Dr. Koji Masuda, Dr. Michihiro Ogawa, Dr. Satoshi Honda, Dr. Shunsuke Yamamoto, Ms. Akiko Orimo, Mr. Junya Kosaka, Mr. Shunji Ohara, and Mr. Shoudai Ishida for their kind assistance, valuable advices, and helpful discussion. The author would like to express the deepest appreciation to Ms. Izumi Okada for her great supports on device fabrication.

The author would like to express his gratitude for Sumitomo Chemical Co., Ltd. for providing various kinds of conjugated polymer samples including PF12TBT and great supports. The author is in acknowledgment of the JSPS Fellowship for Young Scientist,

and the Global COE program (International Center for Integrated Research and Advanced Education in Material Science) from the Ministry of Education, Culture, Sports, Science, and Technology, Japan.

The author would like to offer his special thanks to all members of Ito Laboratory for their kind guidance and fruitful discussion. The author is much obliged to Ms. Aki Yamasaki and Ms. Kayo Kawamura for their kind assistance during the author's school life.

Finally, the author would like to express his deepest gratitude to his parents, Mr. Kenji Mori and Ms. Yaeko Mori, his grandparents, Ms. Tsuyono Mori, Mr. Masamitsu Hirai, and Ms. Akira Hirai, his uncle, Mr. Shuji Hirai for their financial supports, hearty assistance and encouragement.

March 2012

*Daisuke MORI*